Digital Comprehensive Summaries of Uppsala Dissertations
from the Faculty of Science and Technology 2503

Quantum Dots for Tandem Solar Cells Applications

ANETA ANDRUSZKIEWICZ

ACTA UNIVERSITATIS
UPSALIENSIS
2025

ISSN 1651-6214
ISBN 978-91-513-2383-1
urn:nbn:se:uu:diva-550366

UPPSALA
UNIVERSITET

Dissertation presented at Uppsala University to be publicly examined in Polhemsalen, Room 10134, Ångströmslaboratoriet, Lägerhyddsvägen 1, Uppsala, Thursday, 3 April 2025 at 09:15 for the degree of Doctor of Philosophy. The examination will be conducted in English. Faculty examiner: Professor Alberto Vomiero (Luleå tekniska universitet).

Abstract

Andruszkiewicz, A. 2025. Quantum Dots for Tandem Solar Cells Applications. *Digital Comprehensive Summaries of Uppsala Dissertations from the Faculty of Science and Technology* 2503. 142 pp. Uppsala: Acta Universitatis Upsaliensis. ISBN 978-91-513-2383-1.

The recent acceleration of climate change has emphasized the urgent need for renewable energy solutions to mitigate the environmental impact of fossil fuel-based energy generation. Solar power stands out for this purpose because of its availability and capacity to meet global energy demands. Colloidal quantum dot (CQD) solar cells, have garnered attention for their unique optoelectronic properties, like tunable bandgaps, solution-processability and the ability to harvest infrared light. This PhD thesis presents a comprehensive investigation of CQD solar cells, and specifically the combination of CQD solar cells with other photovoltaic technologies. The research findings highlight both the potential of CQD-based tandem solar cells and the challenges for the CQD solar cells that must be addressed to enhance the solar to electricity conversion efficiency.

One focus of the research is the aspects of integrating CQD solar cells with other photovoltaic technologies, such as dye-sensitized and perovskite solar cells. These studies highlight the potential of CQDs to enhance infrared light absorption and energy conversion but reveal critical challenges related to charge recombination and interfacial losses in the CQD solar cell. To address these limitations, the CQD solar cell was investigated in more detail, especially with a focus on surface passivation and the investigation of charge carrier dynamics. Using advanced spectroscopic methods and photoelectrical methods, we could pin-point the most important limitations for the CQD solar cells. The findings demonstrated that effective surface passivation and the optimization of interfacial properties between the CQDs ant the charge extraction layers, are crucial for enhancing charge extraction and minimizing recombination losses in CQD-based solar cells. The results also highlighted the importance of further improve charge transport properties and reduce recombination rates, particularly for larger CQDs.

These insights show the need for continued research, combining advanced methods, surface ligand development and device engineering, to unlock the full potential of CQD solar cells in tandem applications.

Keywords: quantum dots, tandem solar cells, charge recombination, charge transport, surface passivation, interfacial engineering

Aneta Andruszkiewicz, Department of Chemistry - Ångström, Physical Chemistry, Box 523, Uppsala University, SE-75120 Uppsala, Sweden.

ISSN 1651-6214
ISBN 978-91-513-2383-1
URN urn:nbn:se:uu:diva-550366 (http://urn.kb.se/resolve?urn=urn:nbn:se:uu:diva-550366)

To my family and friends

List of Papers

This thesis is based on the following papers, which are referred to in the text by their Roman numerals.

I. Yuan, L., Michaels, H., Roy, R., Johansson, M., Öberg, V., Andruszkiewicz, A., Zhang, X., Freitag, M., Johansson, E. (2020) Four-Terminal Tandem Solar Cell with Dye-Sensitized and PbS Colloidal Quantum-Dot-Based Subcells. *ACS Applied Energy Materials*, 3(4), 3157-3161

II. Andruszkiewicz, A., Zhang, X., Johansson, M. B., Yuan, L., Johansson, E. (2021) Perovskite and Quantum Dot Tandem Solar Cells with Interlayer Modification for Improved Optical Semi-transparency and Stability. *Nanoscale*, 13(12), 6234-6240

III. Johansson, E., Andruszkiewicz, A. (2022) Combining Quantum Dot and Perovskite Photovoltaic Cells for Efficient Photon to Electricity Conversion in Energy Storage Devices. *Energy Technology*, 10(10)

IV. Jingxuan, C., Siyu, Z., Donglin, J., Wanlu, L., Andruszkiewicz, A., Chaochao, Q., Mei, Y., Jianhua, L., Johansson, E., Zhang X. (2021) Regulating Thiol Ligands of p-Type Colloidal Quantum Dots for Efficient Infrared Solar Cells. *ACS Energy Letters*, 6(5):1970-1979

V. Berggren, E., Weng, Y. C., Andruszkiewicz, A., Johansson, F.O.L., Sharma, R., Giangrisostomi, E., Ovsyannikov, R., Cappel, U., Lindblad, A. Interfacial charge transfer dynamics between 2H-MoS_2 and PbS quantum dots, the role of quantum confinement. Manuscript.

VI. Sloboda, T., Svanström, S., Johansson, F., Andruszkiewicz, A., Zhang, X., Giangrisostomi, E., Ovsyannikov, R., Föhlisch, A., Svensson, S., Mårtensson, N., Johansson, E., Lindblad, A., Rensmo, H., Cappel, U. (2020) A method for studying pico to microsecond time-resolved core-level spectroscopy used to investigate electron dynamics in quantum dots. *Scientific Reports*, 10(1)

VII. Andruszkiewicz, A., Eliasson, N., Hammarström, L., Johansson, E. Comparing charge generation, transport and recombination in PbS quantum dot solar cells prepared from two sizes of quantum dots. Manuscript.

Reprints were made with permission from the respective publishers.

Contribution report

My contributions to each of the papers are discussed below:

I I helped with consulting and carrying out some of the experimental work, focusing on the synthesis of colloidal quantum dots (CQDs), fabrication of CQD solar cells, as well as transmission, reflectance and absorption measurements of the samples. I also assisted with manuscript editing.

II I planned and carried out all experimental work, analyzed the data and wrote the manuscript.

III I planned and carried out all the experimental work and analyzed the data. I also contributed to the discussion of all the results as well as the manuscript writing.

IV I assisted in planning and conducting various aspects of the experimental work, including the synthesis of CQDs, ligand exchange reactions to prepare n-type and p-type QDs, fabrication of colloidal quantum dot solar cells using three different thiol ligands, and current-voltage characteristic measurements. I also contributed to manuscript editing.

V I helped with planning and carrying out major parts of the experimental work, including the synthesis of CQDs and ligand exchange reactions for the preparation of n-type and p-type quantum dots, as well as deposition of these n-type and p-type quantum dots. I also prepared the investigated samples by deposition of these QDs on the silicon substrates with the monolayer of molybdenum sulfide (2H-MoS_2). Furthermore, I also conducted a quality assessment of synthesized quantum dots through absorption and photoluminescence measurements, analyzed that data, and contributed to the results discussion and manuscript preparation.

VI I provided a comprehensive training and consultation in the experimental work related to the CQDs. This included synthesis of the CQDs, guidance on ligand exchange reactions for the preparation of n-type and

p-type QDs and the fabrication of QD solar cells. Additionally, I assisted in the quality assessment of the quantum dots through absorption and photoluminescence measurements, and characterization of the complete QD solar cells via current-voltage measurements. I also contributed to the manuscript editing process.

VII I planned, designed and conducted majority of the experimental work, including synthesis of all QDs, ligand exchange reactions for the preparation of all n-type and p-type QDs, fabrication of QD solar cells and fabrication of all samples for femtosecond transient absorption (f-TA) spectroscopy measurements. I also carried out following measurements together with their data analysis: UV-Vis-NIR absorption spectroscopy, photoluminescence spectroscopy, current-voltage characteristic, transient photovoltage and transient photocurrent measurements at varying light intensities and different temperatures. Furthermore, I initiated the result discussion and wrote majority of the manuscript, except of f-TA results and discussion part.

Contents

Abbreviations

α - empirical parameter/ power factor
ε - molar extinction coefficient
ε – electric field
ε_0 - vacuum permittivity
ε_r - relative permittivity
η – efficiency of power conversion
λ - light wavelength
φ - photon flux
2H-MoS_2 – hexagonal crystal structure of molybdenum disulfide
2T - two-terminal
4T - four-terminal
AAc – ammonium acetate
ABT - 4-aminobenzenethiol
$Al(NO_3)_3 \cdot 9H_2O$ - aluminium nitrate nanohydrate
AM1.5G - Air Mass 1.5 Global
AMF - atomic force microscopy
Au – gold
AZO/AlZnO – aluminium doped zinc oxide
A_λ – absorptance
Br – bromide
Br^- - bromide anion
BTA – butylamine
$BuNH_3$ – butylamine
C - constant
c - speed of light
c – concentration
CaF_2 – calcium fluoride
$CaTiO_3$ - calcium titanate
CB – conduction band
Cd – cadmium
CdS – cadmium sulfide

CdSe – cadmium selenide
CdTe – cadmium telluride
CH_3NH_3I/MAI - methylammonium iodide
CIGS - copper indium gallium selenide
Cl^- - chloride anion
CO_2 – carbon dioxide
CQD – colloidal quantum dot
CQDSSC – colloidal quantum dot solar cell
Cs^+ - cesium cation
cSi – crystalline silicon
CVD - Chemical Vapor Deposition
DFT - density functional theory
DMF - N,N-dimethylformamide
DMSO - Dimethyl sulfoxide
DOS – density of states
DSSC - dye-sensitized solar cell
e - elementary charge
E – energy level
e^- - electron
E_{conf} - confinement energy
E_g^{bulk} - band gap of the bulk
E_g – bandgap
E^{QD} - band gap of the quantum dot
$E_{c/v}$ - conduction or valence band edge
EDT – 1,2-ethanedithiol
EQE – external quantum efficiency
ETL - electron transport layer
E_x - built-in electric field
FA^+ - formamidinium
FF – fill factor
fs-TA – Femtosecond Transient Absorption
FTIR - Fourier Transform Infrared Spectroscopy
FTO - fluorine-doped tin oxide
h - Planck constant
$\hbar$ - Planck's constant
HCl – hydrochloric acid
HTL - hole transport material

I - current
I - transmitted light intensity
I – iodide
I^- - iodide anion
I_0 - incident light intensity
I_0 - reverse saturation current/ 'dark current'
I_F - forward diode current/ forwards-bias current
I_m - maximum power point current
I_{ph} - illumination current
InAs – Indium arsenide
IPCE – incident photon-to-current efficiency
IR – infrared
I_{sc} - short-circuit current
ITO - Indium doped tin oxide
J-V – current density-voltage characteristic
J_0 - dark saturation current
J_{sc} - short circuit current density
k - Boltzmann's constant
l - path length
LED - light-emitting diode
LSLE - liquid-state ligand exchange
m_e^* - effective mass of the excited electron
m_h^* - effective mass of the excited hole
MA^+ - methylammonium cation
$MAPbI_3$/MAPI - Methylammonium lead iodide
MEG - multiple exciton generation
MgZnO – magnesium zinc oxide
MHP - methylammonium halide perovskite
MoO_3 – molybdenum(VI) oxide
MPA - mercaptopropionic acid
MPP – maximum power point
n - ideality factor
n^* - critical monomer concentration
N_2 – nitrogen
NIR - near-infrared
nm – nanometers
n_{max} - peak monomer concentration

n_s - saturated monomer concentration
ODE - 1-octadecene
OEA – oleic acid
OPV - organic photovoltaic materials
P – output power
Pb – lead
$Pb(OEA)_2$ - lead oleate
Pb^{2+} - lead cation
$PbBr_2$ - lead bromide
PbI_2 – lead iodide
PbS – lead sulfide
PbS CQDs - lead sulfide colloidal quantum dots
PbS-EDT – lead sulfide quantum dots capped with 1,2-ethanedithiol ligands
$PbS\text{-}X_2$ – lead sulfide quantum dots capped with halide ligands
PbX – lead chalcogenides
PCE – power conversion efficiency
PEDOT - poly(3,4-ethylenedioxythiophene)
PES - steady-state photoelectron spectroscopy
P_{IN} - input power
P_m - maximum power
P_{in} – incident illumination power
PL – photoluminescence
P_{light} - illumination intensity
PLQE - photoluminescence quantum efficiency
P_{max} – maximum power
PSC - perovskite solar cell
PT - 2-propanethiol
PV – photovoltaic
QCE - quantum confinement effect
QD – quantum dot
QDSC - quantum dot solar cell
R - radius of a QD
R – resistance
R_s – Series resistance
R_{sh} - shunt resistance
Rb^+ - rubidium cation
RMS – root-mean-square
R_λ – reflectance

S – sulfur
SCLC - space charge-limited current
Se – selenide
Si – silicon
Sn^{2+} - tin cation
SnO_2 – tin oxide
Spiro-OMeTAD - 2,2',7,7'-tetrakis(N,N-di-p-methoxyphenylamino)-9,9'-spi. robifluorene
SQ - Shockley-Queisser
SRH - Shockley-Read-Hall
$SrTiO_3$ - strontium titanate
SSLE - solid-state ligand exchange
T - temperature in Kelvin
TBAI - tetrabutylammonium iodide
TCO - transparent conductive oxide
Te – tellurium
TiO_2 – Titanium dioxide
TMDC - Transition Metal Dichalcogenide
$(TMS)_2S$ - bis(trimethylsilyl)sulfide
TPC – transient photocurrent
TPV - thermophotovoltaic
TPV – transient photovoltage
TRPES - time-resolved photoelectron spectroscopy
TSC - Tandem solar cell
T_λ - transmittance
UPS - ultraviolet photoemission spectroscopy
UV – ultraviolet
UV-Vis-NIR - Ultraviolet-Visible-Near-infrared
V – voltage/applied bias
V_a – forward bias
V_R – reverse bias
VB – valence band
V_m - maximum power point voltage
V_{oc} – open-circuit voltage
V_{TFL} - trap-filled limit voltage
X – halogens (eg. I, Br, Cl, F)
XPS - X-ray photoelectron spectroscopy
XRD - X-ray diffraction

YAG - yttrium aluminum garnet
$Zn(Ac)_2 \cdot 2H_2O$ - zinc acetate dihydrate
ZnO – zinc oxide
ZnS – zinc sulfide

Introduction

The recent acceleration of climate change, evident through rising temperatures, severe weather events, and melting polar ice caps, has been well-documented over the past century. Anthropogenic carbon dioxide (CO_2) emissions, mostly from burning fossil fuels for energy generation, are its primary source (see **Figure 1a**).[1] By signing the Paris Agreement in 2015, almost all countries acknowledged this crisis and pledged to keep global warming below 2°C (ideally closer to 1.5°C), in order to limit the worst effects of climate change.[2,3] However, despite these efforts, global energy consumption continues to rise emphasizing the importance of shifting to renewable energy to achieve sustainable development goals.[3,4]

Historically, fossil fuels have powered economic growth, but this reliance has come at a high environmental cost. Transitioning from the "coal age" to the "oil age" brought economic growth but at the cost of rising greenhouse gas.[5–9] Today, renewable energy sources such as solar, wind, hydro, and geothermal power offer essential pathways to reducing CO_2 emissions.[10,11] Among these, solar energy particularly stands out due to its abundance, accessibility, and potential to meet global energy demands. In fact, solar energy is the largest source of energy available, providing approximately 23,000 terawatt-years of power to Earth's surface each year—over 1000 times more than the current global annual energy consumption of approximately 18.5 terawatt-years (see **Figure 1b**).[12,13]

Solar energy can be harnessed through photovoltaic (PV) cells, made with semiconducting materials that use the photovoltaic effect to convert sunlight directly into electricity. For a long time, crystalline silicon (cSi) has dominated the PV sector, accounting for 90% of the worldwide market, owing to its relatively high efficiency and long-term reliability.[14] cSi solar cells, with efficiency surpassing 19% for commercial modules and 26% for research cells[15], have seen considerable cost reductions, with prices lowering by 90% in the last decade.[14,16,17] Despite these developments cSi solar cells have some limitations. For example, silicon-based cells are unable to effectively capture the entire spectrum of sunlight. Particularly, they are not efficient at absorbing the light in the infrared (IR) region. As a result, much of the IR light is lost (see **Figure 1c**).[18] Furthermore, the energy-intensive processes necessary for silicon purification increase the environmental and economic costs of producing these solar cells.[19–21]

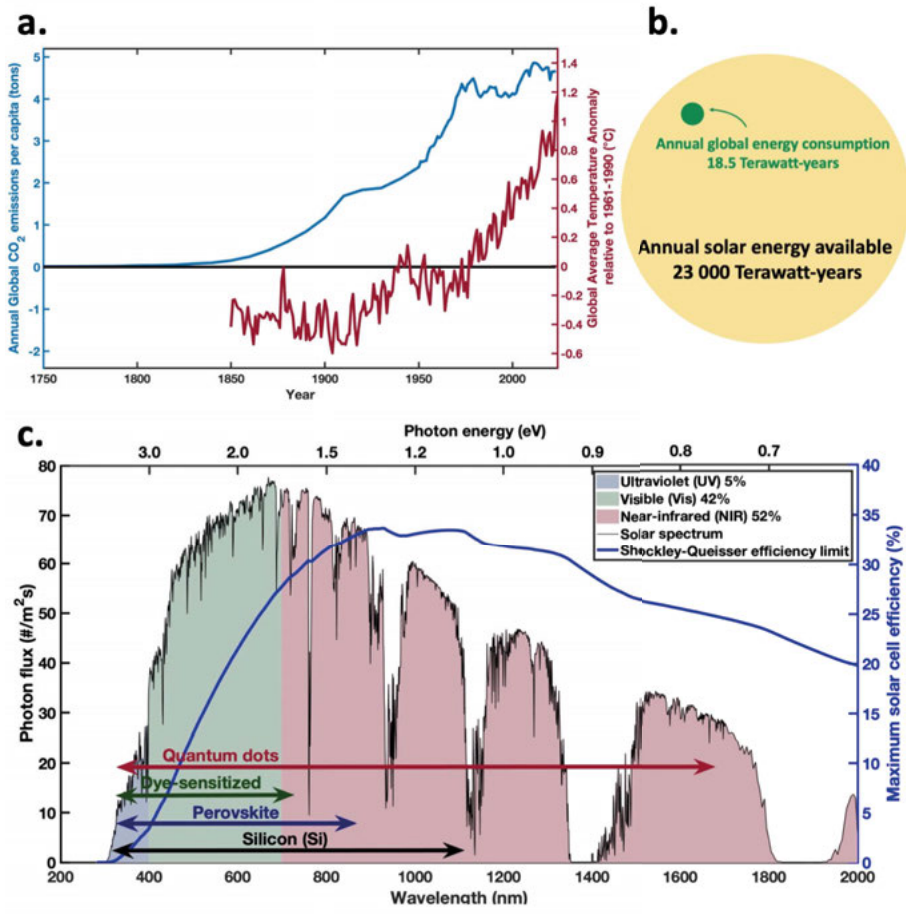

Figure 1. (a) Global temperature anomaly and CO_2 emission (data taken from Global Carbon Budget (2024); Population based on various sources (2024) – with major processing by Our World in Data and Met Office Hadley Centre (2025) – processed by Our World in Data). **(b)** Comparison between annually available solar energy and annual global energy consumption. **(c)** Solar spectrum at AM1.5G with highlighted ultraviolet, visible and near-infrared regions and the Shockley-Queisser efficiency limit of solar cells by bandgap energy. Black, Blue, green and red arrows refer to the approximate spectral response range for the commonly studied solar materials: silicon (Si), perovskite, dye-sensitized and quantum dot, respectively.

To overcome these limitations, new photovoltaic technologies were researched, such as hybrid organic-inorganic or thin-film solar cells (see **Figure 1c**). These devices are lighter, more flexible, and less costly to manufacture than traditional silicon solar cells. Among them, colloidal quantum dots (CQDs) are particularly interesting. Being made of the semiconductor nanocrystals, they exhibit unique optoelectronic properties due to quantum confinement effects. These materials offer tunable bandgaps, making them highly

versatile for harvesting light across a broader range of the solar spectrum, including the IR region.[22–25] And that makes QDs especially promising for tandem solar cells applications, where materials with complementary absorption spectra are stacked to capture a broader range of sunlight, enhancing overall power conversion efficiency by reducing spectral and thermalization losses. QD-based tandem cells, such as those combining lead sulfide (PbS) QDs with other photovoltaic materials (e.g. perovskites or silicon), can potentially surpass the Shockley-Queisser (SQ) limit by capturing lower-energy photons that would otherwise be wasted.[26,27]

However, despite their advantages, QD-based tandem solar cells face several challenges, including material compatibility, charge transport issues, surface passivation, photostability, and synthesis complexity, which limit their commercial viability. The integration of quantum dots with other materials often leads to interface issues and poor charge extraction, while surface trap states can cause non-radiative recombination, further reducing efficiency. Additionally, achieving optimal bandgap engineering and ensuring long-term stability under environmental stress remain as significant problems. Addressing these challenges is crucial to advance this photovoltaic technology as sustainable energy solutions.

Photovoltaics basics

Photovoltaic devices utilize semiconductors to capture sunlight and convert it into electricity. This section provides an overview of the semiconductor physics essential for this process, starting by modeling the operation of solar cell using the p-n junction and followed by deriving the measure of the system's performance. Additionally, the chapter discusses the limitations of single-junction and tandem solar cells.

p-n Junction

The fundamental principle of a solar cell is the conversion of light into electrical energy, a process known as the photovoltaic effect. This phenomenon was first observed by Edmond Becquerel in 1839.[27] A solar cell typically comprises a photoabsorber that absorbs light to excite electrons (e^-) and two selective contacts that spatially separate the photogenerated charges. The separation of charges can be facilitated by an electric field within the material of the solar cell, causing electrons to move in one direction and holes in the other. This charge separation generates a current flow and electric power when connected to an external circuit.

This process is crucial for the conversion of light into electrical energy and is commonly observed in solar cells with p-n junctions without an external voltage applied across the junction **(Figure 2)**. Upon the junction of p-type and n-type semiconductors, the equilibrium of Fermi levels occurs, leading to the migration of electrons from donors to acceptors. This creates a narrow charged region on each side of the junction, known as the space-charge or depletion region, where free electrons and holes are depleted. The resulting electric field in this region acts as a barrier, impeding the movement of charge carriers in one direction while allowing it in the other.

When a positive voltage is applied (forward bias – V_a), the barrier for electrons and holes to move to the opposite side is reduced or disappears (**Figure 3b**). This allows electrons to flow from the n-type to the p-type region and holes to flow in the opposite direction, resulting in a net current across the junction.

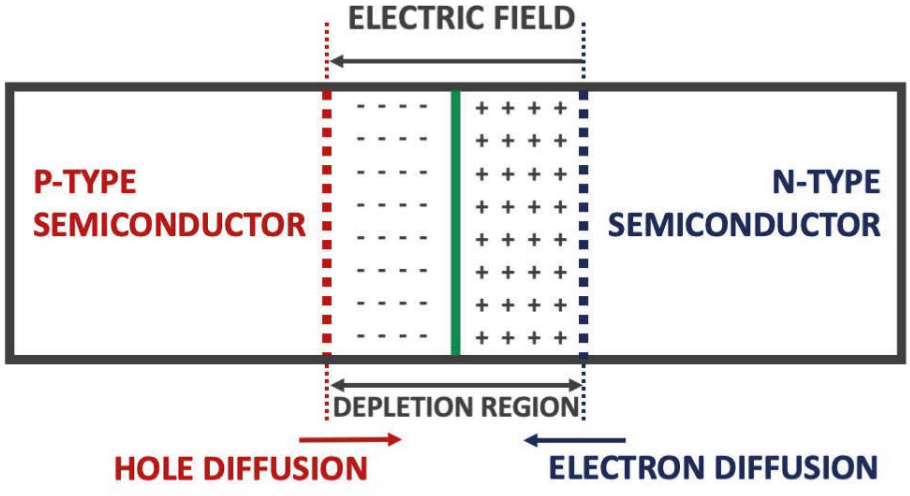

Figure 2. Scheme of p-n junction under equilibrium state (dark and zero bias applied). Negatively charged acceptors are symbolized by '-' signs, while positively charged donors are symbolized by '+' signs. The green line represents the boundary between the p-type and n-type semiconductors in the metallurgical junction.

In contrast, when a negative voltage is applied (reverse bias – V_R), the barrier for electrons and holes to move to the opposite side increases (**Figure 3c**). The device is no longer in equilibrium, and the Fermi level is no longer flat. Quasi-Fermi levels, E_{Fn} for electrons and E_{Fp} for holes, represent the distribution of carriers between the CB and VB in the presence of excess carriers generated by the applied bias.

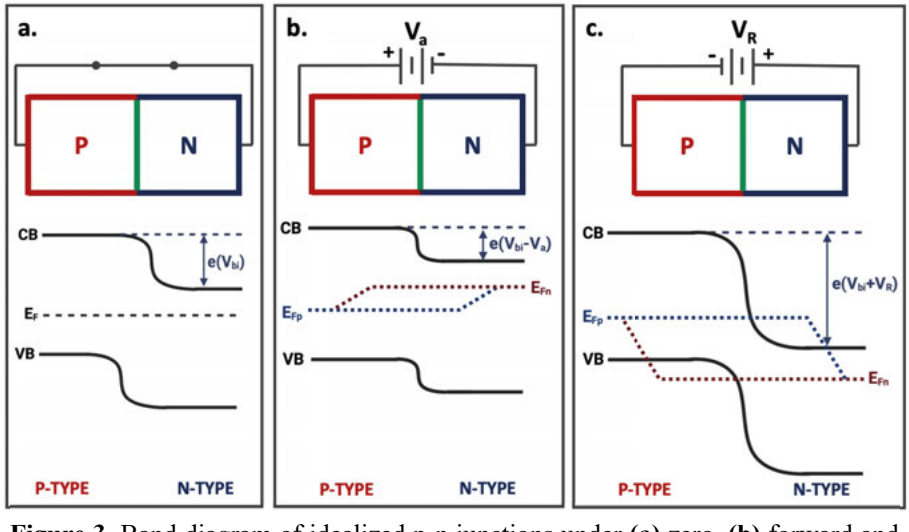

Figure 3. Band diagram of idealized p-n junctions under **(a)** zero, **(b)** forward and **(c)** reverse bias.

This stronger barrier suppresses the flow of charge carriers, leaving only a small current due to thermally generated minority carriers. The magnitude of this current is referred to as the reverse saturation current (I_0) or as 'dark current'.

The effect of applied bias can be described using the ideal-diode equation:

$$I = I_0 \left(exp \left(\frac{eV}{kT} \right) - 1 \right) \tag{5}$$

where I is the current, I_0 is the reverse-saturation current, e is the elementary charge, V is the applied bias, k is the Boltzmann's constant, and T is temperature in Kelvin. A negative voltage represents reverse bias, while a positive one represents forward bias. The equation is plotted in **Figure 5.**

Solar Cell Power Generation and Equations

Figure 4 provides a detailed explanation of the generation of electric power by a solar cell. By illuminating the p-n junction a photon interacts with the semiconductor material and generates an electron-hole pair (exciton). Due to the built-in electric field (E_x) facing toward the p-type region, electrons are

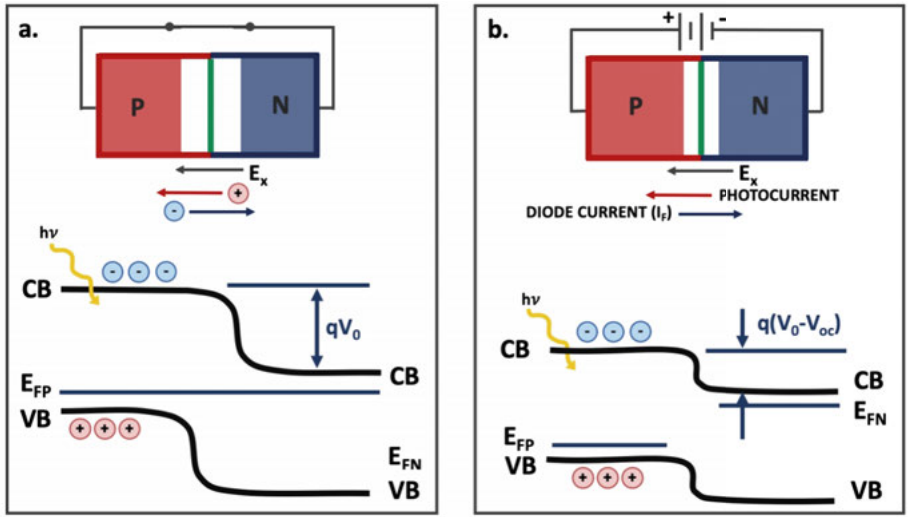

Figure 4. (a) Illumination of the p-n junction generates electron-hole pairs (excitons). Electrons and holes are depicted as '⊖' and '⊕', respectively. The built-in electric field (E_x) directs electrons toward the n-type region. When the terminals are connected, this movement creates the short-circuit current (I_{sc}), driven by the electron-hole pair generation rate. **(b)** Without terminal connection, electrons accumulate in the n-type region, building a voltage across the junction capacitance. This forward voltage generates a current that balances the drift current of the photon-generated electrons. At equilibrium, the open-circuit voltage (V_{oc}) is established.

migrating towards the n-type region. Connecting the two terminals allows the majority of electrons to flow to the n-type region, creating an electrical current, known as the short-circuit current (I_{sc}), driven by the rate of electron-hole pair generation from incident radiation. In scenario where the terminals are not connected externally, accumulated electrons in the n-type region lead to a voltage buildup across the junction capacitance. This results in a forward voltage for the diode and reduces the thickness of the transition region, leading to the creation of a forward diode current (I_F). Equilibrium is attained when this forward diode current matches the drift current of the photon-generated electrons, establishing the open-circuit voltage (V_{oc}) across the two terminals of the solar cell under illumination.

The equation for the net current produced by a solar cell is represented by the difference between the illumination current $\left(I_{ph}\right)$ and the forwards-bias current (I_F):

$$I = I_{ph} - I_F = I_{ph} - I_0 \left(exp\left(\frac{eV}{kT}\right) - 1\right) \tag{6}$$

The term I_F is defined by the ideal diode equation and I_0 is the reverse saturation (dark) current and V is voltage.

In context of solar cell operation, two condition are of particular importance, open-circuit condition and short-circuit condition. The solar cell is effectively open-circuited, meaning that no external load is connected ($R = \infty$), when the current flowing through the circuit is zero and there is no closed path for the current to follow. Therefore, the voltage across the terminals is at its maximum value, known as the open-circuit voltage and is defined by the following condition:

$$I_{ph} = I_0 \left(exp\left(\frac{eV}{kT}\right) - 1\right) \tag{7}$$

This condition leads to the expression

$$V_{oc} = \frac{kT}{e} ln\left(\frac{I_{ph}}{I_0} + 1\right) \tag{8}$$

On the other hand, the solar cell is effectively short-circuited, meaning that the terminals are connected with zero resistance ($R = 0$), when the current flows freely without any external load resistance resulting in the maximum possible current output. Therefore,

$$I = I_{ph} = I_{sc} \tag{9}$$

where I_{sc} represents the short-circuit current.

The output power (P) of a solar cell is the product of voltage and current,

$$P = IV \tag{10}$$

After substituting it with equation (6) it produces following expression

$$P = IV = \left[I_{ph} - I_0\left(exp\left(\frac{eV}{kT}\right) - 1\right)\right]V \tag{11}$$

The maximum output power can be calculated by taking the derivative of $\frac{dP}{dV}$ and setting it to zero. This is referred to as the maximum power point with maximum power point voltage ($V = V_m$) and maximum power point current ($I = I_m$). This point describes a rectangle whose area, given by $P_m = V_m I_m$. This will result with following expression

$$\frac{dP}{dV} = \frac{d(IV)}{dV} = \left[I + V\frac{dI}{dV}\right] = 0 = I_{ph} - I_0\left(exp\left(\frac{eV}{kT} - 1\right)\right) - V_m\left(\frac{I_0 e}{kT}\right)exp\left(\frac{eV_m}{kT}\right) \tag{12}$$

which after reorganizing will yield

$$V_m\left(\frac{I_0 e}{kT}\right)exp\left(\frac{eV_m}{kT}\right) = \frac{I_{ph}}{I_0} + 1\ . \tag{13}$$

At the maximum power point, the voltage across the terminals (V_m) and the current flowing through the cell (I_m) are both less than the corresponding values at open circuit (V_{oc}) and short circuit (I_{sc}), respectively. This is a fundamental characteristic of solar cells and is a consequence of the trade-off between voltage and current that occurs during the operation of the cell.

Considering that V_{oc} and I_{sc} represent the maximum voltage and current, respectively, the ratio given in the subsequent equation is termed as the fill factor (FF) of a device:

$$FF = \frac{I_m V_m}{I_{sc} V_{oc}} \tag{14}$$

The efficiency of power conversion, denoted as (η) , is defined as the ratio of the maximum power (P_m) to the input power (P_{IN}), which after substitution, and normalization by the area of illumination will be expressed as:

$$\eta = \frac{P_m}{P_{in}} \times 100\% = \frac{V_{oc} J_{sc} FF}{P_{in}} \times 100\% \tag{15}$$

where J_{sc} is short circuit current density.

The current-voltage characteristic of a solar cell under dark and illuminated condition is shown in **Figure 5**.

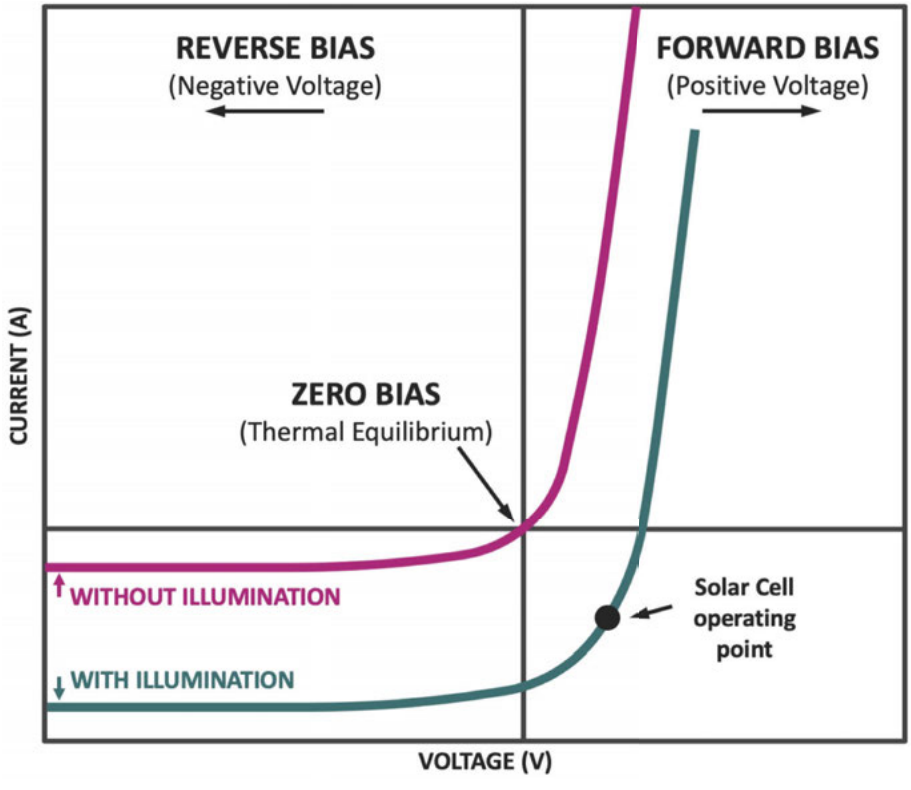

Figure 5. The current-voltage (I-V) characteristic of solar cell without and with illumination.

Limiting Efficiencies and Non-ideal Effects

Solar cells represent a promising avenue for sustainable energy generation, with their efficiency being a critical factor in determining their practical viability. At its heart lies the concept of the Shockley-Queisser (SQ) limit, which sets the theoretical ceiling for single-junction solar cell efficiency.[18] The SQ limit is predicated on a delicate balance between photogeneration, where incident photons are converted into electron-hole pairs within the semiconductor material, and recombination, where these charge carriers recombine, resulting in efficiency losses.

Bandgap engineering plays a pivotal role in achieving optimal efficiency. The semiconductor's bandgap (E_g) must be carefully selected to strike a balance between maximizing photon absorption and minimizing thermalization losses. This entails ensuring that photons with energies above the bandgap are efficiently absorbed, while those below the bandgap do not lead to excessive thermalization. However, the ideal bandgap is not solely determined by absorption considerations; it also necessitates a delicate equilibrium between short-circuit current density and open-circuit voltage. In pursuit of higher

efficiency, solar cell design must navigate the trade-offs associated with bandgap selection. A narrow bandgap facilitates broader absorption spectra, thereby increasing J_{sc}, but may come at the cost of reduced V_{oc} due to diminished quasi Fermi level splitting. Conversely, a wider bandgap maximizes V_{oc} but may limit J_{sc} due to suboptimal absorption efficiency. Striking the optimal balance between these competing factors is principal in realizing the highest achievable power conversion efficiency.[29]

Despite theoretical predictions, real-world solar cells are also a subject to several non-ideal effects that curtail their performance. One is Shockley-Read-Hall (SRH) recombination, which arises from impurities or defects within the semiconductor material.[30,31] These imperfections act as electron or hole traps, diverting charge carriers away from the electrical contacts and reducing the overall efficiency of the solar cell.

Parasitic resistances further influence the challenge of achieving high efficiency in solar cells. Series resistance (R_s) and shunt resistance (R_{sh}) reduce the photocurrent within the solar cell, diminishing both fill factor and ideality factor. Series resistance, stemming from internal resistance within the cell and its contacts, impedes current flow, while shunt resistance provides alternate paths for current, bypassing the active region of the cell.[32,33]

Optical losses present another significant obstacle.[34] Reflection at the interfaces of the cell leads to the loss of incident photons, while parasitic absorbance by front contacts further diminishes the overall absorption efficiency. Lowering defects through improved surface passivation and optical engineering offers avenues for enhancing solar cell performance.

Addressing these non-ideal effects remains a central focus of solar cell research and development. Innovations in materials, device architectures, and fabrication techniques offer promise in overcoming these challenges and approaching the theoretical limits of solar cell efficiency. Integration with advanced technologies such as tandem and multi-junction solar cells, as well as emerging materials like perovskites and quantum dots, holds further potential for enhancing the performance of solar energy conversion devices.

Tandem Solar Cells

As mentioned in the previous chapters, semiconductor materials are the fundamental building blocks of solar cells, serving as the key components that enable the conversion of light into electrical energy through the photovoltaic effect. However, their ability to absorb light is limited by its specific bandgap energy. A semiconductor can only absorb photons with energies greater than or equal to its bandgap energy, meaning that a large portion of the solar spectrum will not be effectively utilized. The excess energy of the photons with energy higher than the bandgap energy will be lost through a process called thermalization, where the excited electrons relax back down to the conduction band edge, dissipating the excess energy as heat. This trade-off between having a low bandgap semiconductor, which can absorb a larger portion of the solar spectrum, or a wide bandgap semiconductor which minimize thermalization losses, fundamentally limits the efficiency of single-junction solar cells.

The Shockley-Queisser limit, which is based on thermodynamic principles, defines the maximum theoretical power conversion efficiency (PCE or η) that can be achieved by a solar cell. For a single-junction solar cell under unconcentrated sunlight this limit is around 31%.[18,29] To overcome SQ efficiency limit, multi-junction solar cell architectures were introduced. These advanced solar cell designs make use of two or more absorber layers, each with a different bandgap, stacked on top of one another. By utilizing this approach, the higher-energy photons are captured by the material with the larger bandgap, while the lower-energy photons are allowed to pass through and reach the smaller-bandgap semiconductors below. This enables a more efficient use of the solar spectrum, as the energy from different regions of the spectrum can be harnessed by the appropriate absorber. **(Figure 6)** Theoretically, a tandem (two-junction) solar cell under unconcentrated sunlight (AM1.5G spectrum) could reach 47% efficiency, a three-junction a 52%, while an infinite-junction even up to 68%, far surpassing the Shockley-Queisser limit for single-junction devices.[35] While an infinite-layered device is not practically feasible, the multi-junction structures does achieve record-braking performances. For example, the highest reported efficiency for the tandem (two-junction) device is held by perovskite-silicon junction and is above 32%.[36,15] While with the overall highest efficiency for multi-junction device was so far produced by six stacked junctions and reach around 39% under unconcentrated sunlight and 47% under concentrated sunlight.[37]

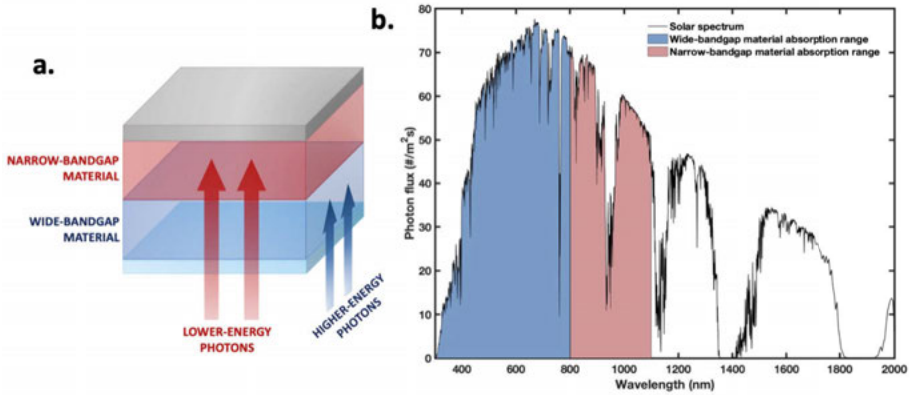

Figure 6. (a) In multi-junction solar cells, high-energy photons are absorbed by the larger bandgap material, while lower-energy photons pass through to smaller-bandgap semiconductors below. **(b)** Solar spectrum utilization by multi-junction solar cells - each absorber capture energy from different spectral regions.

Tandem solar cells (TSCs) have two main configurations illustrated in **Figure 7**: the two-terminal (2T) and four-terminal (4T).[38] In the 2T design, the sub-cells are monolithically fabricated and connected by a tunnel junction or recombination layer, requiring only two external electrical contacts. The 4T design, on the other hand, involves fabricating the sub-cells on separate substrates and stacking them, with each sub-cell connected to an independent external circuit, necessitating four contacts. The 2T design offers a slight total efficiency advantage due to the reduced number of semi-transparent contacts, which can lead to lower optical losses. However, the fabrication process for 2T tandem cells is more challenging, particularly for solution-processed devices, where the solvents used to deposit the second cell can potentially damage the underlying layers.

Regardless of the architectural design, the operation of tandem solar cells is similar to that of a single-junction device. Each sub-cell can generate a short-circuit current and an open-circuit voltage under illumination. During operation, the cell is held at a voltage between V_{oc} and zero, generating a current and with the goal of operating at the maximum power point, where the generated power (current × voltage) is maximized. In a 2T tandem cell configuration, the sub-cell voltages are added, whilst according to Kirchhoff's law the photocurrents must be matched, limiting the overall photocurrent to that of the lower-performing sub-cell. Since the sub-cells harvest vastly different regions of the solar spectrum, careful optimization of their bandgaps and efficiencies is required to achieve the necessary photocurrent matching. On the contrary, the 4T configuration allows the sub-cells to be effectively operated separately, avoiding the current-matching limitations and requiring less rigorous bandgap optimizations.

Overall, the development of tandem and multi-junction solar cell architectures has been a significant advancement in the field of photovoltaics, enabling higher conversion efficiencies and a more efficient utilization of the solar spectrum compared to traditional single-junction solar cells. As research in this area continues to progress, further improvements in the design, fabrication, and optimization of these advanced solar cell structures are expected to drive the continued advancement of solar energy technology.

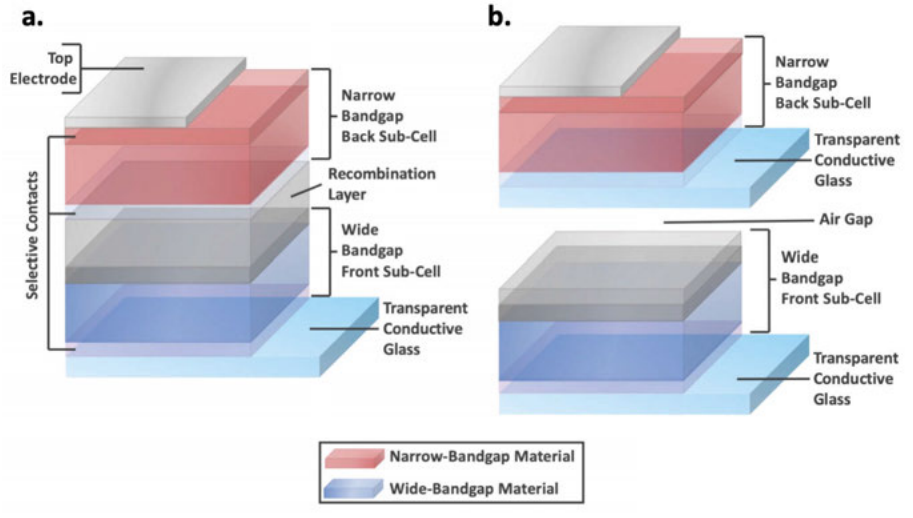

Figure 7. Architectures for **(a)** 2-terminal (2T) and **(b)** 4-terminal (4T) tandem solar cells.

Colloidal Quantum Dot Photovoltaics

Colloidal quantum dots (CQDs) are solution processed semiconductor nanoparticles with the radius smaller than the exciton Bohr radius of their bulk material. This results in size-dependent optoelectronic properties, such as a tunable bandgap (E_g), leading to adjustable absorbance and photoluminescence.[39,40] The synthesis of quantum dots was first documented four decades ago, and since then the continuous research has led to their utilization in a wide array of applications from medicine and optoelectronics to solar harvesting.[41–43] In this chapter I will review the CQDs physics, CQDs materials, CQDs based solar cell working principle and charge generation, transport and recombination in CQDs based solar devices.

Colloidal Quantum Dots

Almost exactly forty years ago, Louis E. Brus[44,45] and Alexei I. Ekimov[46], independently examined nanocrystals dispersed in colloidal solutions and glass, respectively. These parallel studies, later supplemented by future advances in synthesis by chemists such as Moungi G. Bawendi[47], contributed to the development of the field of colloidal quantum dots (CQDs). Despite variations in the forms of matter containing the nanocrystals, their findings suggested that the size of the nanocrystal could, under certain conditions, be determined by a diffusion-controlled microscopic precipitation process. Additionally, they observed that QDs just a few nanometers in size displayed unique optoelectronic characteristics distinct from those of bulk materials. This collective body of research, which included foundational discoveries and methodological advancements, awarded them the Noble Prize in Chemistry in 2023 for their pivotal contributions to the development of QDs.

Due to their opposite charges, electrons and holes possess the potential to form bound states within a material. These bound electron-hole pairs are identified as a quasi-particle entity - an exciton and are characterized by the separation distance known as the exciton Bohr radius.[48] The significance of the exciton Bohr radius increases notably as the semiconductor particle diminishes in size. Particularly noteworthy are instances where the exciton dimension surpasses that of the particle itself, as observed in quantum dots. Present understanding indicates that the band gap of quantum dots is primarily governed by the diameter of the particles, owing to the quantum confinement

phenomenon.[44–46,49] The dimensionality of a material determines the extent to which its carriers act as free carriers in terms of the number of dimensions involved. In a bulk semiconductor, a continuous density of states gives rise to both conduction and valence bands. However, when the number of atoms in the lattice is limited, the density of states becomes discrete, losing the continuous band-like characteristic. Generally, when a material's electronic density of states is affected by one or more small dimensions, the material is considered confined. This confinement can manifest as quantum wells, quantum wires, or quantum dots. The variation of the semiconductor density of states function with the dimensions of the material is demonstrated in **Figure 8a**. Bulk semiconductor materials exemplify three-dimensional systems where the density of states is proportional to $\left(E - E_{c/v}\right)^{1/2}$. In a quantum well system, which is two-dimensional, electrons are confined in one dimension, resulting in a step-like density of states. In a quantum wire system, a one-dimensional setup, electrons are confined in two dimensions, leading to a density of states proportional to $\left(E - E_{c/v}\right)^{-1/2}$. A quantum dot, being a zero-dimensional system, confines electron motion in all three dimensions. Consequently, QDs exhibit atomic-like density of states represented as a sequence of delta functions $\delta\left(E - E_{c/v}\right)$ at allowed energy levels and the energy levels are discrete. This discrete nature is the essential characteristic contributing to the distinctive properties of QDs. **Figure 8b** further describes the comparison between the electronic energy structures of a bulk semiconductor and a quantum dot. The continuous parabolic energy level in bulk semiconductors contrasts with the discrete energy levels in confined QDs. The confinement energy $\left(\Delta E_{conf}\right)$, which represents the quantum energy associated with localizing electrons and holes, becomes more pronounced as the size of the QD decreases towards the Bohr radius. In regions of weak confinement, where the QD size is approximately equal to the Bohr radius, the wave function exhibits characteristics that are intermediate between hydrogenic and confined forms. However, in regions of strong confinement, where the QD size is smaller than the Bohr radius, the wave function is solely controlled by carrier confinement within the spherical space of the QD. Essentially, this means that the size of the nanocrystal determines the bandgap of the QDs and regulates the emission wavelength region, making them a highly promising candidate for advanced optoelectronic devices.

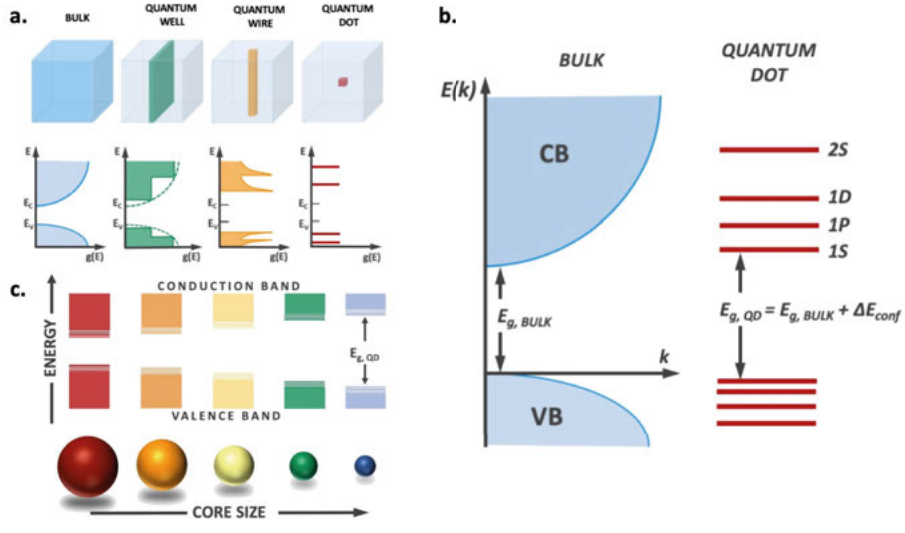

Figure 8. (a) Variation of the semiconductor density of states function with the dimensions of the material. **(b)** Schematic comparison between the electronic energy structures of a bulk semiconductor and a quantum dot. **(c)** Comparison between the electronic band gap of a quantum dot as a function of QD core size.

The threshold at which quantum confinement occurs for semiconductor nanoparticles, defined by the exciton Bohr radius, spans from 2 to 50 nm across different materials[50], with a value of approximately 18 nm for PbS.[51] As already described when the particle size nears these thresholds (as illustrated in **Figure 8c**), the exciton wave functions become confined, thereby restricting the available energy states for electrons. Consequently, the material's band gap widens. This range of sizes where these effects are observed is commonly known as the quantum confinement regime. Within this regime, the energy gap exhibits size dependency, as described by the Brus equation[45]:

$$E^{QD} = E_g^{bulk} + \frac{\hbar^2}{8R^2}\left(\frac{1}{m_e^*} + \frac{1}{m_h^*}\right) - \frac{1.8e^2}{4\pi\varepsilon_r\varepsilon_0 R^2} \tag{16}$$

where E^{QD} and E_g^{bulk} represent the band gaps of the quantum dot and bulk, respectively, R denotes the radius of a QD, and m_e^* and m_h^* represent the effective masses of the excited electron and hole, respectively. $\hbar$ is Planck's constant, and ε_r and ε_0 denote relative and vacuum permittivity, respectively. The middle term of Equation 16 signifies the confinement energy, while the right term represents the exciton Coulombic interaction energy, which may be negligible in materials with high dielectric constants (like PbS). It is evident that the confinement energy is inversely proportional to the R^2 of the quantum dot, allowing for the modulation of its band gap by adjusting its size.

Materials

Nanocrystals of semiconductor materials have attracted significant scientific interest due to their extraordinary potential in optoelectronic applications. These materials exhibit unique physical properties governed by the (QCE), which becomes prominent when their dimensions are smaller than the corresponding exciton Bohr radius (see **Figure 9**).[23,52] Such nanocrystals are referred to as quantum dots (QDs). A remarkable feature of QDs is the phenomenon of multiple exciton generation (MEG), which enables the generation of more than one electron-hole pair per high-energy photon absorbed.[53–55] This property offers the potential to surpass the Shockley–Queisser efficiency limit of single-junction solar cells.[56] QDs also have several other advantageous properties, including a size-tunable bandgap[24,57,58], narrow emission spectra[57,59], and solution-processability[60,61].

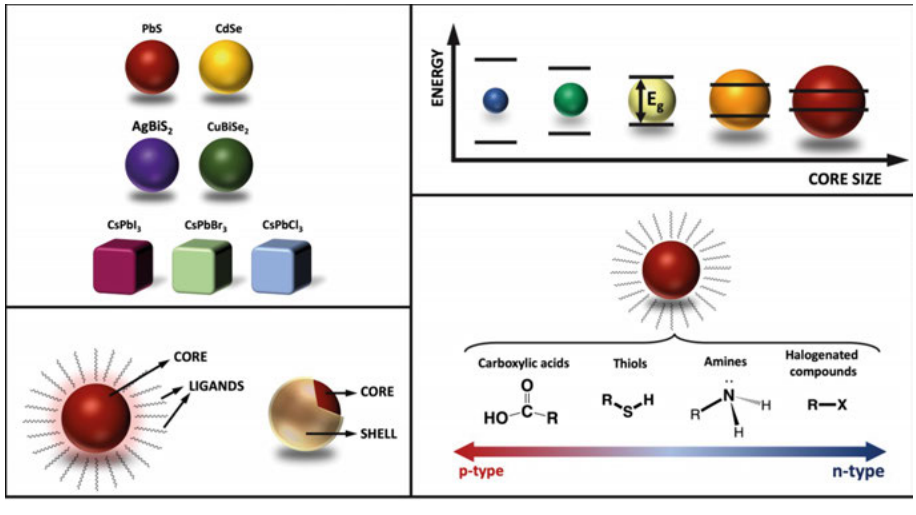

Figure 9. Schematic summary of several types of QD materials found in solar cell applications and QDs optoelectronic characteristics tuned by the core size/composition and the surface ligand passivation.

These versatile properties make QDs highly significant for a wide range of optoelectronic applications, schematically illustrated in **Figure 10**, including photovoltaics, photodetectors, luminescent devices, lasers, and photocatalysis.

In photovoltaics, QDs with strong infrared (IR) absorption capabilities are particularly valuable for developing high-performance single-junction and tandem solar cells.[26,27,61–63] By extending light absorption into the near-infrared (NIR) region, QDs enable broader solar spectrum utilization. QDs can be synthesized from a variety of semiconductor materials, ranging from single-element systems like silicon to binary and ternary compounds, including cadmium (Cd) or lead (Pb) chalcogenides.[64–66] Among the most studied QDs for

photovoltaic applications are lead chalcogenides (PbX, where X = S, Se, Te).[67] Recently, metal halide perovskite QDs have also emerged as promising alternatives due to their tunable optoelectronic properties.[68,69] For luminescent applications, such as light-emitting diodes (LEDs) and fluorescent biomarkers, core-shell QDs are most commonly employed. Examples include cadmium chalcogenides (e.g., cadmium selenide (CdSe)) with protective shells like zinc sulfide (ZnS), which enhance stability and emission efficiency.[60,70] In laser applications, indium arsenide (InAs) QDs are of interest due to their tunable IR emission.[71] Meanwhile, PbS QDs also have demonstrated significant potential in photocatalysis, such as for CO_2 reduction, owing to their strong IR absorption and efficient charge transfer properties.[72]

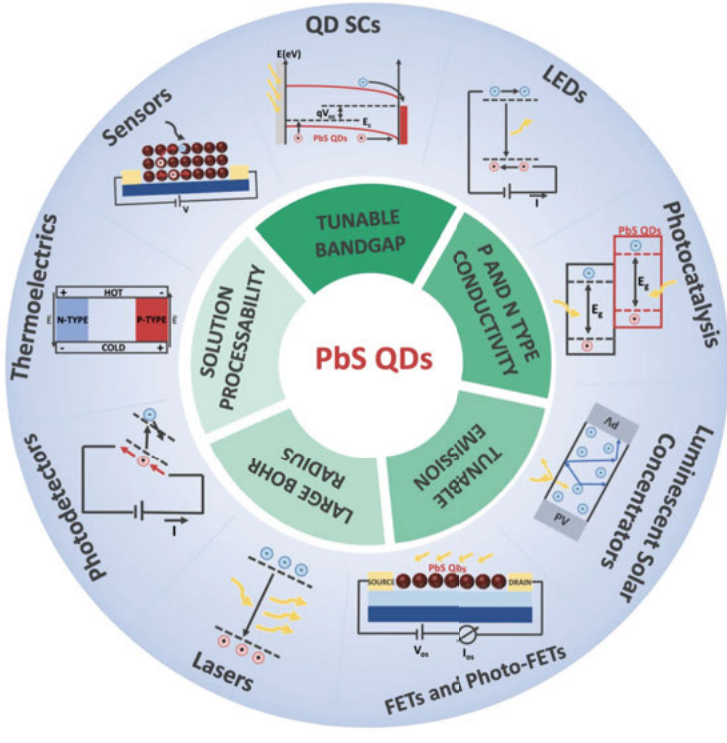

Figure 10. Schematic illustration of the QDs and their wide range of optoelectronic applications.

The unique surface properties of QDs have also spawned their own field of research. Due to their high surface-to-volume ratio, QDs have a large proportion of surface atoms (approximately 25% for 2 nm QDs).[73] These surfaces are typically passivated with ligands, which can be organic or inorganic, single- or multi-dentate, and range from single-atom species to long-chain molecules.[43] The choice of ligands strongly influences QD stability, electronic properties, and compatibility with specific applications (see **Figure 9**).

Metal chalcogenides, a class of semiconductor materials, have been central to optoelectronic research since before World War II. [67] These materials are widely interesting for utilization in third-generation solar cells due to their high absorption coefficients, size-dependent properties, and stability under solar irradiation. Metal chalcogenides can be classified into three categories for QD-based sensitizers:

1. **Heavy metal chalcogenides**: Includes CdX and PbX (X = S, Se, Te) and hybrid structures (e.g., alloyed or core-shell systems). [74–77]
2. **Eco-friendly metal chalcogenides**: Includes Cu-(III-V)-X_2 and Ag-(III-V)-X_2 (where III-V = In, Bi and X = S, Se), offering alternatives with lower toxicity. [78–80]
3. **Other transition metal chalcogenides**: They possess unique properties for specific applications but are less commonly used.[81–84]

The primary focus of this thesis is on lead sulfide colloidal quantum dots (PbS CQDs). PbS QDs have garnered attention for their exceptional optoelectronic properties and high performance in photovoltaic applications. Unlike II-VI nanocrystals, such as CdSe, CdTe, and CdS, which are limited by large bandgaps that restrict absorption to visible wavelengths (up to ~800 nm), PbS QDs exhibit tunable bandgaps (0.7–1.5 eV) and broad-spectrum absorption, spanning the ultraviolet (UV) to IR regions. PbS is a binary IV-VI semiconductor with a large exciton Bohr radius (18 nm), which facilitates strong quantum confinement effects in nanocrystalline forms.[85] PbS is a direct bandgap material (E_g~ 0.41 eV for bulk), and shows high carrier mobility, a high static dielectric constant (17.3), and a low effective electron mass (<0.1m*).[86–88] These properties contribute to its strong photoconductivity, high absorption cross-section, and efficient multiple exciton generation.[89] Additionally, PbS QDs demonstrate excellent stability, low-cost synthesis, and low-temperature processing (<200°C), making them particularly suitable for high-performance infrared solar cells.

Significant advancements in surface passivation and device engineering have propelled PbS QDs to the forefront of QD solar cell research. Infrared PbS-based quantum dot solar cells have achieved power conversion efficiencies (PCEs) exceeding 15% and have demonstrated excellent operational stability under prolonged illumination.[90] This progress highlights their suitability for integration as bottom cells in tandem solar cells, where they can complement other technologies such as perovskite, organic, or dye-sensitized solar cells.[27]

The promising attributes of PbS QDs underscore their promising potential of solution-processed PbS QDSCs for the development of next-generation solar cells.

Device Structure

Quantum dot solar cells (QDSCs) offer diverse advantages, such as tunable light response through quantum dot size adjustments, scalable synthesis, solution-based deposition techniques, and the potential for multiple-exciton generation. These properties make semiconductor quantum dots very interesting for producing cost-effective, large-area, lightweight, flexible, and high-efficiency photovoltaic cells. Over the past decade, the development of QDSCs, particularly those utilizing PbS nanocrystals, has accelerated due to improvements in materials and device architectures. Advances in materials engineering include better quantum dot size control, improved surface passivation, electronic trap state reduction, and enhanced deposition techniques. Additionally, architectural innovations have drawn from inorganic semiconductors and organic optoelectronics, with specific adaptations for CQD films and materials. The efficiency of electron-hole pair separation, rapid charge carrier collection and optimization of energy level alignment for efficient charge extraction directly influences the photovoltaic performance of CQD solar cells. Therefore, exploring advanced charge transport materials and optimizing device architecture are essential for achieving high-performance CQD solar cells. This chapter will review recent developments in efficient carrier transport materials and device structure optimization for CQD solar cells, mainly focusing on the type used in this thesis (p-i-n heterojunction).

Various device structures have been explored to enhance the photovoltaic performance of CQDSCs. In 2007, a Schottky-structured CQDSC with a PCE of 1% was reported.[91,92] Its structure featured a CQD solid film as the photoactive layer placed between a transparent oxide electrode and a metal electrode with a shallow work function (**Figure 11a**).[93] Further performance improvements were hindered by significant charge carrier recombination at the CQD/electrode interfaces.[94,95] To address this, researchers focused on modifying the device architecture to enhance charge carrier extraction. One approach involved incorporating an n-type oxide, such as TiO_2, SnO_2, or ZnO, as an electron transport layer (ETL) between the oxide electrode and the CQD solid film, creating a p-n depleted heterojunction within the CQDSC (**Figure 11b**).[96–100] This configuration improved the interface contact between the ETL and the CQD solid film, facilitating effective electron injection from CQDs

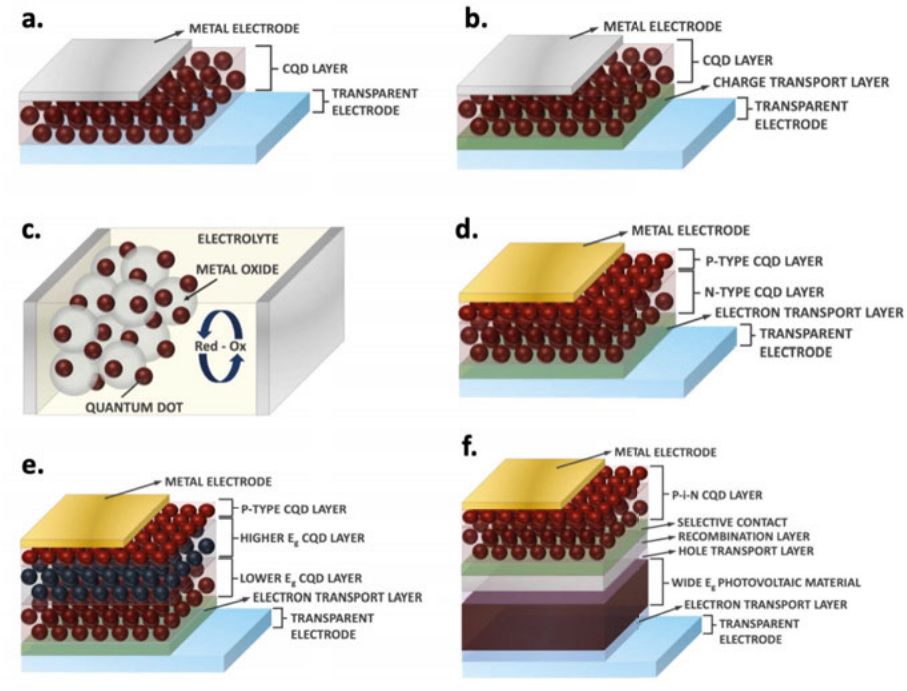

Figure 11. Schematic structures of **(a)** Schottky CQD solar cell, **(b)** depletion heterojunction CQD solar cell, **(c)** CQD-sensitized solar cell, **(d)** p–i–n CQD solar cell, **(e)** graded architecture CQD solar cell and **(f)** 2T-tandem solar cell employing CQD sub-cell.

into the ETL and reducing non-radiative interfacial recombination. The efficiency of hole extraction is critical for the V_{oc} and overall photovoltaic performance of heterojunction-structured CQDSCs. To optimize hole extraction, various hole transport materials (HTLs), such as MoO_3[101–103], p-type CQDs[65,104–106], and polymers[107–111], have been employed. These HTLs aid in efficient hole extraction, thereby enhancing the overall device performance.

Another exploited structure used colloidal quantum dots as sensitizers when applied over transparent mesoporous electron acceptors (e.g. TiO_2 or ZnO), to create CQD-sensitized solar cells (CQDSSCs), as shown in **Figure 11c**.[112–114] This concept is derived from dye-sensitized solar cells (DSSCs).[115] CQDs offer several benefits over traditional organic dyes, including lower cost, a broader absorption spectrum, and greater stability. However, surface defects in CQDs and a high hole-trapping rate can lead to charge carrier recombination issues. Additionally, the CQDSSCs must be well-sealed to prevent electrolyte leakage and their long-term stability can be compromised by the instability of the polysulfide electrolyte.

In recent years, the p-i-n heterojunction structure has become widely adopted in CQD SCs, demonstrating effectiveness in aiding efficient charge carrier extraction.[116,117] This also the QDs based device structure widely used in this thesis. As illustrated in **Figure 11d**, this structure includes a transparent

oxide electrode (Indium doped tin oxide - ITO), an electron transport layer (ZnO), a CQD solid film (CQD-PbX_2, X = I and Br, prepared from CQD inks), a hole transport layer (CQD-EDT, EDT – 1,2-ethanedithiol), and a metal electrode (Au).[118–120] Unlike the p-n depleted heterojunction structure, the p-i-n configuration incorporates a HTL between the CQD solid film and the metal electrode, enhancing hole extraction at the back junction of the device. The efficiency of CQDSCs using a p-i-n heterojunction structure has significantly improved to approximately 14%, with potential for further enhancement through optimization of the device structure or CQD surface chemistry.[121] Additionally, the development of CQD inks has significantly advanced the optimization of CQDSC device architecture, thereby enhancing overall performance. CQD inks have facilitated the realization of graded architectures in CQD SCs. Traditional CQDSCs feature two depletion regions at the ETL/CQD-PbX_2 and CQD-PbX_2/HTL interfaces, with a quasi-neutral region in between. While the built-in electric field in the depletion regions aids charge carrier extraction, carriers in the quasi-neutral region rely on diffusion, which competes with recombination due to sub-bandgap traps from imperfect CQD surface passivation. This recombination limits CQDSC performance. Graded structures, achieved by stacking CQDs of varying sizes, improve band alignment and enhance the built-in electric field at the back junction, reducing recombination in the quasi-neutral region.[63,122–124] However, conventional polar solvents like butylamine (BTA) disrupt underlying CQD layers during deposition. Using non-polar solvents such as toluene, chlorobenzene, and chloroform to dissolve CQDs, as facilitated by forming PbS-BTA complexes, allows for the construction of graded architectures (**Figure 11e**), enabling further device optimization.

The bandgap tunability of the PbS colloidal quantum dots allows their use both in single junction solar cells as well as in tandem solar cells combined with other photovoltaic materials (**Figure 11f**).[125] As described in chapter "Tandem solar cells", multi-junction solar cells with suitable and optimal bandgaps can enhance solar spectrum utilization and reduce energy losses seen in single-junction devices (heating of high-energy photons and transmission of low-energy photons), potentially achieving power conversion efficiencies over 45%.[126] For example, metal halide perovskites, which are promising solution-processed photovoltaic materials, have achieved high PCEs exceeding 25%. However, despite their excellent visible light absorption, perovskites have limited efficiency in capturing infrared photons. In contrast, PbS CQDs offer strong infrared absorption, an adjustable bandgap and low-temperature solution-processability, which makes them ideal for developing tandem solar cells by combining low-E_g CQDs with high-E_g photovoltaic materials. The combined development of CQDs and perovskites allowed tandem solar cell efficiencies beyond 24%.[127] CQDs can also be integrated with other CQDs (CQDs/CQDs)[128,129], organic photovoltaic materials (CQDs/OPV)[130–132], and dye-sensitized solar cells (CQDs/DSSC)[133] to create efficient tandem solar cells. Although the current efficiency of such tandem solar cells is still lower

than that of the highest efficiencies of perovskite devices, the tandem architecture presents a promising avenue for improving overall photovoltaic performance. The foundation for that lies in complementary light absorption and improvement of the worse performance tandem sub-part, which often is CQDSC. Various studies also have demonstrated that interlayers are crucial for enhancing device performance. Therefore, the challenge remains in finding materials with better matching absorption spectra and fully exploiting the infrared absorption capabilities of CQDs for tandem solar cells.

Charge generation, transport and recombination

As already stressed in previous chapters of this thesis CQDSCs offer a promising approach to photovoltaic technology. Central to maximizing their potential is a thorough understanding of charge generation, transportation, and recombination mechanisms. This chapter explores these critical processes and strategies aimed at optimizing QDSC performance.

When a quantum dot in a CQDSC is illuminated with photons of sufficient energy, excitons are generated. Theoretically, the minimum energy required is equivalent to the QD's bandgap, where absorbing one photon results in the creation of one exciton. However, if the photon energy exceeds twice the bandgap energy, multiple exciton generation can occur, where a single high-energy photon generates multiple excitons.[53–55,134–136] Upon photon absorption, an electron is excited to higher energy states above the conduction band (CB) edge, creating a "hot" electron. This hot electron is unstable and will eventually relax to the CB edge by either releasing excess energy as heat (cooling process) or transferring energy to excite another electron from the valence band (VB) to the CB, thus generating two excitons from a single photon via the MEG process.

Once generated, excitons can undergo various relaxation processes.[137–140] Non-radiative processes include exciton dissociation, where the exciton splits into a free electron and hole for charge extraction, carrier trapping in defect-induced "trap states" within the bandgap,[141–146] and energy transfer to adjacent QDs or Auger recombination[89,147–150], where one exciton recombines non-radiatively by transferring energy to another exciton, which is then ejected as a hot carrier.[151–153] These processes can significantly impact the QDSC efficiency by reducing the number of free charge carriers available for electricity generation.

Charge transport in CQDSCs involves the movement of electrons and holes through the QD solid films (see **Figure 12**).[153–155] This can occur via hopping between adjacent QDs, facilitated by short interparticle distances and suitable surface ligands,[156–159] or through band-like transport in well-ordered QD arrays[160–162].

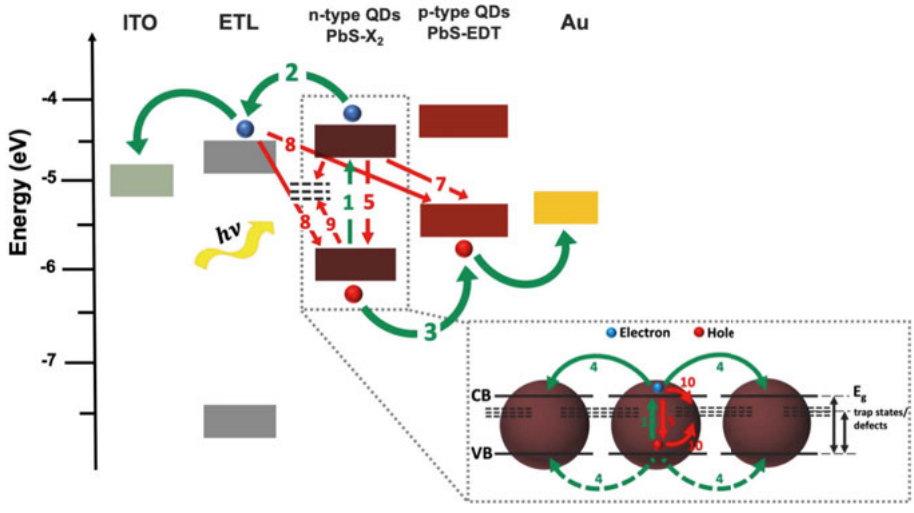

Figure 12. Charge transport and recombination processes in CQD SCs, indicated with green and red arrows, respectively. Figure adapted from Paper VII.

The efficiency is influenced by the QD size, surface ligands affecting the inter-dot coupling, and doping density or band engineering altering the carrier mobility and diffusion length.[163,164] Effective carrier injection from the QD film into the electron/hole transport layers requires good energy level alignment to minimize energy barriers, achieved by engineering the QD surface chemistry and selecting appropriate transport layer materials to facilitate efficient charge transfer.[152,157]

Charge recombination in QDSCs can occur through radiative recombination within QDs, which involves the recombination of an electron and a hole, resulting in the emission of a photon, a process known as photoluminescence, which typically occurs on a timescale of nanoseconds to microseconds, or already mentioned non-radiative processes. Also, surface recombination can occur at the QD film/transport layers interfaces or within the quantum dots themselves due to defects or improper energy level alignment.[165] The typical recombination processes occurring in PbS CQD solar cell are schematically shown in **Figure 12**.

To enhance QDSC performance, surface passivation techniques like ligand exchange or inorganic shell coating can be implemented to reduce surface trap states on the QDs, suppress non-radiative recombination and improve charge extraction. Aligning the energy levels of QDs and transport layers can facilitate efficient carrier injection and minimize interfacial recombination. Whilst optimizing QD size and composition tailors the bandgap for improved sunlight absorption and photocurrent. Nanostructured architectures like core-shell QDs or ordered QD arrays also can improve charge transport and reduce recombination losses.[166]

By addressing the challenges associated with these processes and employing effective improvement strategies, the performance of CQD solar cells can be significantly enhanced, paving the way for their widespread application in photovoltaic technology.

Perovskite Photovoltaics

What is perovskite

The word 'perovskite' refers to the mineral that was discovered in the 19th century and named after the Russian mineralogist Lev Perovski. However, the material crystal structure was first analyzed and described in 1926 by Victor Goldschmidt.[167] Numerous oxide perovskites display valuable magnetic and electrical characteristics. For instance, double perovskite oxides like manganites demonstrate ferromagnetic behavior and significant magnetoresistance effects.[168]

Perovskite materials used for solar cells usually follow the formula ABX_3, where A is a cation, B stands for a metal cation and X is an anion.[169–171] The structure is comprised from the corner-connected BX_6 octahedra, where cation A fill up the in-between spaces and they are sometimes referred to as "organic-inorganic hybrid perovskites". In this chapter I will briefly describe different perovskite materials, the most common solar cell structures based on perovskites, as well as charge dynamics within them.

Materials

In the widely studied organic-inorganic hybrid metal halide perovskite solar cells, the A-site monovalent cation can be either an inorganic ion such as cesium (Cs^+) or rubidium (Rb^+), or a small organic ammonium ion like methylammonium (MA^+) or formamidinium (FA^+). The B-site is typically occupied by a divalent metal cation, usually lead (Pb^{2+}) or tin (Sn^{2+}), while halides such as iodide (I^-), bromide (Br^-), or chloride (Cl^-) occupy the X-site (**Figure 13**). Methylammonium lead iodide ($MAPbI_3$) is a fundamental perovskite material and it was first synthesized in 1978 by Dieter Weber[172,173]. Initially it was studied for its conductive[174,175] and luminescent properties[176,177]. The potential of metal halide perovskite in photovoltaics was first demonstrated by Miyasaka et al. in 2009 when $MAPbI_3$ was employed as light-absorbing material in dye-sensitized solar cells, achieving a PCE of 3.8%.[178] Following that, other research groups independently replaced liquid electrolytes in those cells

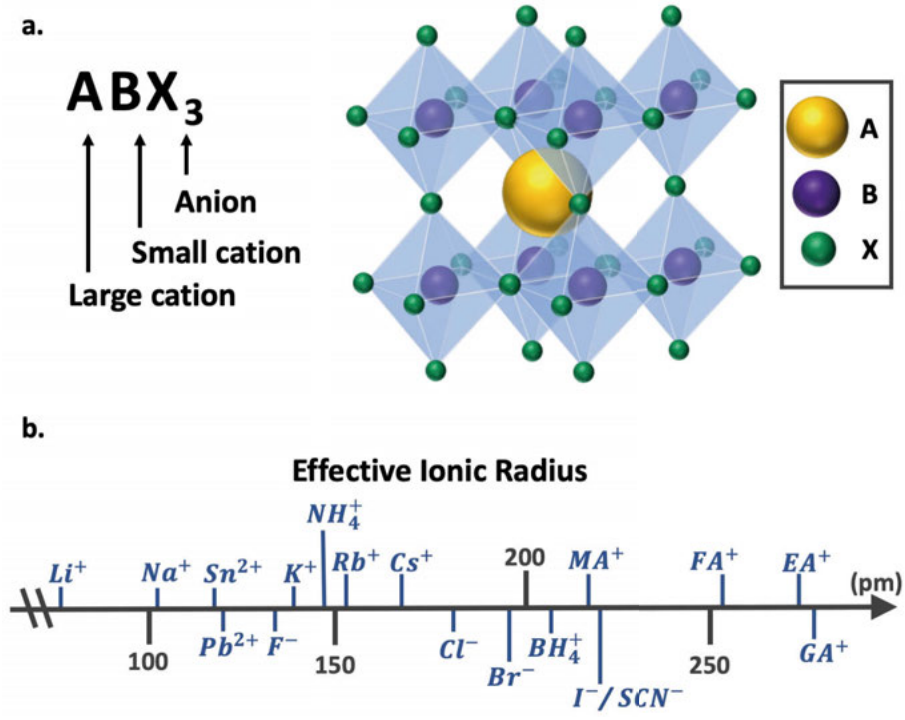

Figure 13. (a) The schematic structure of cubic crystal of the ABX_3 type perovskite. **(b)** Schematic representation of the effective ionic radii for various ions that can be used for ABX_3 perovskites, arranged according to their effective sizes.

with solid-state hole transport materials like Spiro-OMeTAD (2,2',7,7'-tetrakis(N,N-di-p-methoxyphenylamino)-9,9'-spirobifluorene), and subsequently increasing the PCE of these early perovskite solar cells to over 10%.[179,180] This established perovskite solar cells (PSCs) as a focus of global research. The PCE of these early perovskite solar cells exceeded 10%, spurring significant research efforts to enhance cell performance. Through advancements such as compositional engineering, including the development of "triple cation" perovskites, efficiencies continued to improve, with PCEs surpassing 20% by the mid-2010s.[181–183] As of 2024, perovskite solar cells have achieved a certified PCE exceeding 26%, rivaling traditional silicon-based technologies.[15] Additionally, significant strides have been made in addressing the toxicity of lead in PSCs by exploring lead-free alternatives, particularly tin-based perovskites. Even though they face challenges such as stability and defect tolerance, recent developments show promise for achieving competitive efficiencies while mitigating environmental concerns.[184–186]

Perovskite Solar Cell Structure

Similarly to colloidal quantum dot solar cells, perovskite solar cells employ layered device architectures in which the active light-absorbing layer is sandwiched between electron transport layer and hole transport layer. This architectural similarity reflects a shared design strategy aimed at optimizing charge extraction while minimizing recombination losses. Both CQDSCs and PSCs utilize a range of solution-based and vacuum-based deposition techniques, enabling the production of lightweight, flexible photovoltaic devices.[187] Both systems can also be integrated in tandem PV configurations to maximize the utilization of the solar spectrum due to their ability to tune the band gap through material size and/or composition management in CQDSCs and composition engineering in PSCs.[188]

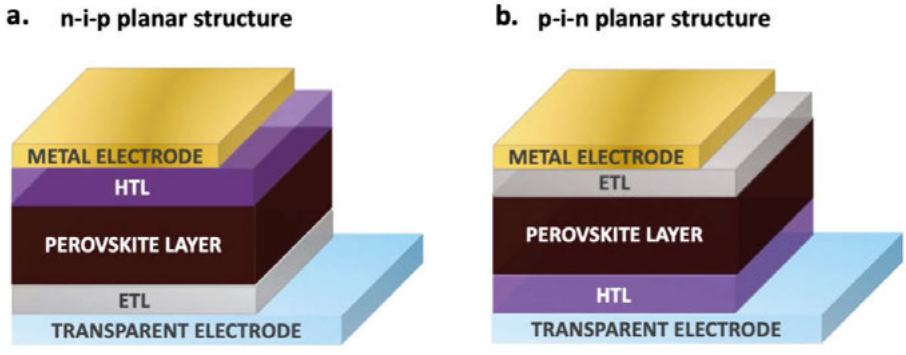

Figure 14. Schematic structures of perovskite solar cells: **(a)** n-i-p planar structure (standard configuration) and **(b)** p-i-n planar structure (inverted configuration).

Two primary single-junction PSC architectures are the n-i-p and p-i-n planar structures, as depicted in **Figure 14**. While n-i-p configurations often yield the highest power conversion efficiencies (PCEs), p-i-n structures offer superior stability and compatibility with tandem PV applications. Perovskite based devices utilized in this thesis are based on n-i-p planar configuration. PSCs are highly versatile due to the wide range of materials used in their multilayer structure, including electrodes, ETLs, HTLs, and the methylammonium halide perovskite (MHP) absorber layer. Structural and material modifications of these basic architectures allow for significant performance tuning. MHP films, composed of various base materials, can be enhanced through doping, alloying, and the incorporation of additives. These films exhibit diverse microstructures and grain-boundary characteristics that influence device efficiency and stability. Thin interfacial layers are also commonly introduced at the MHP/ETL and MHP/HTL interfaces to further optimize device performance.[187]

Perovskite layers can be fabricated using solution-based (wet) or vacuum-based (dry) processes.[189,190] Wet processes, such as spin-coating or blade-

coating, are commonly used for thin films formation but face challenges in scalability to large-area devices.[191–193] Dry processes, like thermal evaporation, offer certain advantages, such as conformal deposition on textured substrates (e.g., silicon), but present difficulties in controlling precursor stoichiometry and incorporating passivation agents. Both methods operate at relatively low temperatures (<150°C), allowing for the production of lightweight and flexible PSCs on plastic substrates.[194–196]

Thanks to their highly tunable bandgaps, wide-bandgap PSCs are ideal as "top" cells in tandem PVs. They can be paired with narrow-bandgap "bottom" cells made from silicon, cadmium telluride (CdTe), copper indium gallium selenide (CIGS), organic photovoltaics (OPVs), other perovskites or quantum dots.[188] Such tandem configuration allows the "top" PSC to absorb shorter wavelengths, while the "bottom" cell harvests longer wavelengths, thereby surpassing the SQ efficiency limit for single-junction PVs. Recent advancements have significantly improved tandem PV performance, and as of 2024 the certified record for PSC/Si tandem has a PCE of 33.7%.[15]

Charge generation, transport and recombination

The operation of perovskite solar cells (PSCs), analogously to the CQD solar cells, relies on efficient charge generation, transport, and minimization of recombination processes within the light absorber layer. Upon photon absorption, excitons (bound electron-hole pairs) are generated in perovskite layer, which quickly dissociate into free charge carriers due to the low exciton binding energy of perovskites, typically a few to tens of meV.[197,198] This rapid dissociation occurs on an ultrafast timescale, similar to the exciton dynamics in quantum dot solar cells (QDSCs).[199–201]

The generated free charges in PSCs must be transported to their respective electrodes to generate photocurrent. Charge transport occurs via band-like mechanisms, facilitated by the unique crystal structure and high dielectric constant of the materials.[202,203] However, defects, such as vacancies or grain boundaries, can act as trap states, impeding charge transport and increasing non-radiative recombination losses.[204,205] This challenge is mirrored in QDSCs, where defect-induced trap states also affect charge dynamics.

Charge recombination is a significant loss mechanism in PSCs. Radiative recombination, which emits photons when electrons and holes recombine, sets a fundamental limit for the V_{oc}.[206] Non-radiative recombination reduces charge carrier lifetimes and overall performance, paralleling the non-radiative processes found in QDSCs, such as carrier trapping followed by recombination.[207] The thermal generation of free charge and low levels of nonradiative recombination are critical properties if PSCs are to approach the Shockley-Queisser efficiency limit, where detailed balance stipulates that all recombination is radiative.[208]

Both PSCs and QDSCs exhibit similar timescales for charge generation, transport, and recombination, which can span from femtoseconds to microseconds, depending on material quality and architecture.[209] Addressing defects through strategies like compositional and interfacial engineering has been extensively explored in PSCs[210,211], just as surface passivation techniques are utilized in QDSCs to enhance charge extraction and reduce non-radiative losses.

There are also few differences between the PSCs and CQD SCs. One of them is the larger surface area of CQDs compared to the larger perovskite crystals in PSCs, making surface passivation even more critical in QDSCs to mitigate the effects of surface defects and ensure efficient carrier dynamics. Also, charge transport mechanisms differ between the two technologies. In PSCs, transport occurs through a band-like mechanism enabled by the long-range order of the perovskite crystals. Whereas in QDSCs, transport is dominated by tunneling or hopping between adjacent quantum dots, which is highly dependent on interparticle distances and surface ligands.

In summary, understanding and controlling charge generation, transport, and recombination are critical for enhancing the efficiency and stability of both perovskite and quantum dot solar cells, given their shared challenges in charge dynamics.

Aim of this thesis

The primary aim of this thesis is to investigate quantum dot solar cells, focusing on enhancing efficiency in tandem applications together with various photovoltaic technologies. The starting point of this research was the fundamental question: How can PbS quantum dots be effectively integrated into tandem solar cells to improve their efficiency in converting near-infrared light into electricity? To address this, the unique properties of QDs with different sizes and different surface ligands and their potential synergies with other promising solar call technologies are analyzed. This research particularly seeks to address the limitations currently hindering QD solar cells from achieving competitive efficiencies for conversion of near infrared light to electricity.

The research presented in this thesis is encapsulated in seven papers, each contributing to a comprehensive understanding of QD solar cells. The initial studies focus on foundational aspects of QD integration, demonstrating how their tunable bandgaps and excellent light absorption capabilities can be harnessed to improve overall device performance in tandem photovoltaics. However, while the integration of QDs in tandem devices was successful, these findings reveal significant challenges: particularly high charge recombination rates and inefficient charge transport mechanisms, which impede the effectiveness of QD solar cells.

Recognizing that the main bottleneck was the performance of QD solar cells, subsequent research focused on finding critical design principles and interfacial engineering strategies for QD solar cells. This includes a thorough examination of surface passivation techniques aimed at mitigating recombination losses and enhancing charge extraction. This prompts the question: How does ligand selection and surface passivation influence charge carrier dynamics and recombination losses in PbS QD solar cells? In parallel, the role of interface engineering in QD solar cells was examined, raising another key question: How can interfacial modifications in QD solar cells improve charge transport and reduce recombination losses?

Beyond that, QD size emerged as another crucial factor influencing device behavior. Larger QDs are particularly attractive for tandem configurations due to their enhanced near-infrared absorption. However, their electronic properties and charge transport behavior differ significantly from smaller QDs. This prompts the question: How does the size of PbS quantum dots impact charge dynamics, recombination rates, and overall solar cell efficiency, particularly

in the context of tandem applications? Understanding these effects is essential for optimizing QD sub-cell in tandem architectures.

Ultimately, this thesis lays a robust foundation for future investigations into QD solar cells and their integration with other advanced photovoltaic technologies in tandem solar cells. The insights gained here not only underscore the promise of QD solar cells in tandem architectures but also pave the way for the development of innovative materials and engineering approaches that could significantly enhance the performance of photovoltaic devices.

Experimental

Synthesis

Hot-Injection Synthesis of QDs

Synthesis of quantum dots can be completed through either bottom-up or top-down methods.[212,213] Top-down techniques involve reducing a bulk material to nanometer-sized fragments through physical or chemical processes. Among them we can distinguish an electron beam lithography and ion implantation. Conversely, bottom-up approaches rely on self-assembly to form quantum dots and involve wet-chemical and vapor-phase methods. However, producing quantum dots with consistent size is difficult because they tend to aggregate, forming more stable, bulk-like materials. To counteract aggregation, quantum dots are typically maintained in colloidal state, where each quantum dot is enveloped by a long-chain organic molecule, such as oleic acid or oleylamine. This help to keep the quantum dots separated from one another.

A commonly used method for synthesizing PbS CQDs, and also the one widely employed in this thesis, is based on the work of Hines and Scholes.[214] This is a wet-chemical synthesis involving a hot-injection technique, where the sulphur precursor, bis(trimethylsilyl)sulfide ($(TMS)_2S$), is swiftly injected into a heated lead precursor - solution of lead oleate ($Pb(OEA)_2$). The process is illustrated in **Figure 15** and starts with in situ preparation of lead oleate solution (SOLUTION 1) by reacting PbO with oleic acid (OEA) in non-polar solvent, 1-octadecene (ODE). First this solution is degassed with a constant nitrogen (N_2) flow through solution for 2-3 hours. Then it is heated up to a desired temperature for the injection of sulphur precursor solution (SOLUTION 2). The lead oleate solution also changes colour from yellow to transparent upon the heating up process. Simultaneously, the sulphur precursor solution is prepared by dissolving appropriate amount of $(TMS)_2S$ in ODE, degassing it under vacuum and heating it up to the desired injection temperature. Upon hot injection, the lead oleate solution quickly turns dark, signifying the nucleation and growth of oleic acid-passivated PbS CQDs. Shortly after the injection the heat source is removed to stop the growth of PbS-OEA

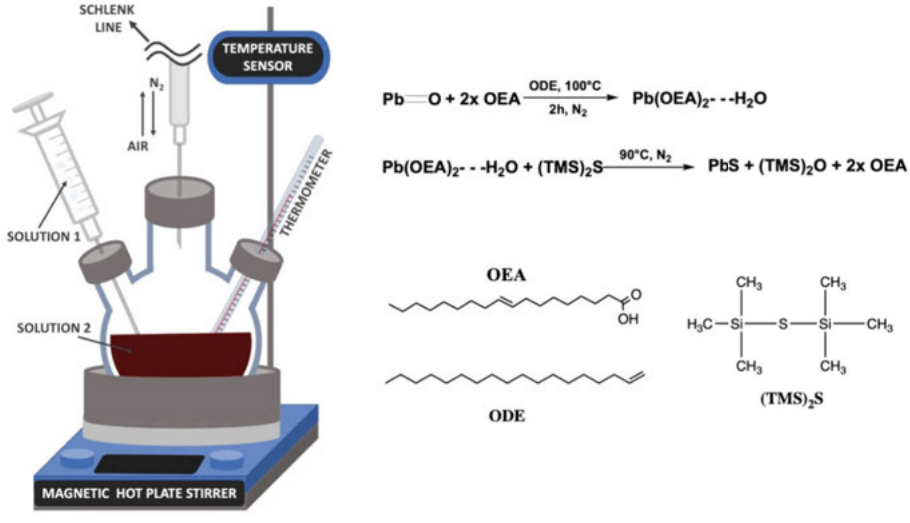

Figure 15. Schematic representation of the hot injection synthesis of PbS colloidal quantum dots. On the left is a schematic apparatus illustration: a three-neck round-bottom flask, sealed with septum, placed on the magnetic hot plate stirrer with temperature control and temperature sensor. The flask is connected via tubing with a Schlenk line to control the flow of air and nitrogen. The thermometer inserted into a flask is for precise control of solution temperature. The SOLUTION 2 is swiftly injected into degassed SOLUTION 1 with a syringe at precisely chosen temperature. On the right are reactions schemes and chemical structures of the substrates.

nanoparticles and allow cooling of the solution. The size of these CQDs can be adjusted by changing the reagent concentrations, injection temperatures, and solution volumes.[22] The exciton peak, which is visible in the absorbance spectra of the CQDs in solution, correlates with their size. **Figure 16**, adapted from **Paper VII**, shows an example of two CQDs sizes that were synthesized in this thesis.

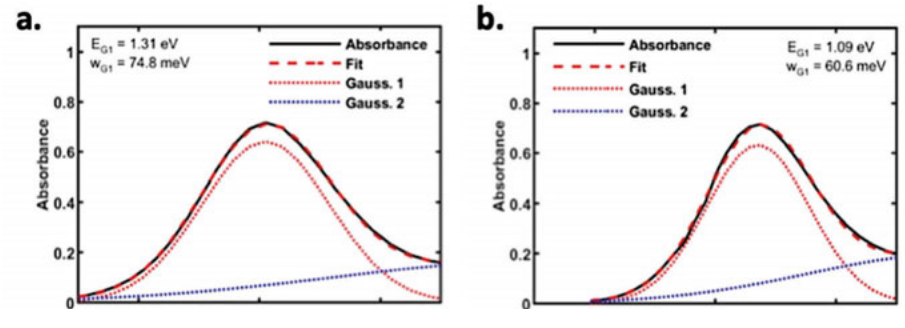

Figure 16. Steady state UV-Vis-NIR absorption spectra with Gaussian fits to the lowest energy exciton band for **(a)** PbS1-OEA and **(b)** PbS2-OEA dispersed in octane. Adapted from **Paper VII**.

During the hot-injection synthesis the nanoparticles grow quickly, stabilized by long OEA molecules that prevent excessive aggregation and precipitation. During growth, ligands attach to and detach from the nanoparticle surface at rates dependent on the solution temperature, affecting the shape of the dots along with the ligands' stereochemistry. Prolonged heating can cause some particles to dissolve while others continue growing, leading to a wide size distribution and unstable solution, necessitating rapid growth termination.[215] The La Mer and Dinegar model can be used to explain and visualize the formation of CQDs (**Figure 17**) in more detail.[216–218]

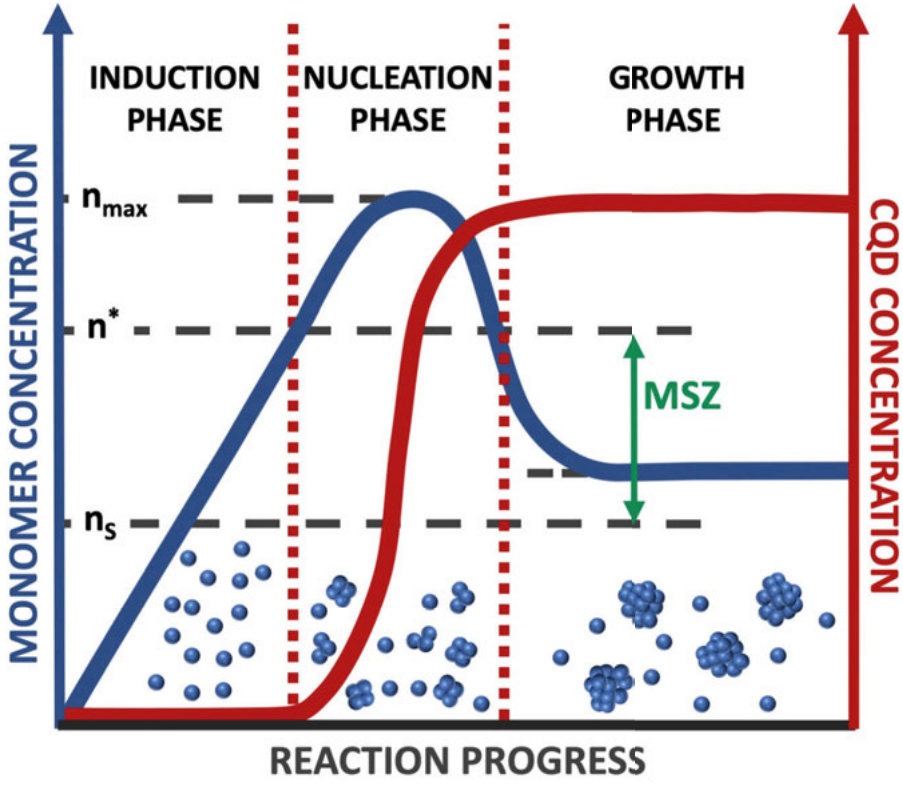

Figure 17. The LaMer – Dinegar model of nucleation and growth dynamics of CQDs. n_s, n^* and n_{max} represent the saturated monomer concentration, the critical monomer concentration and the peak monomer concentration, respectively. The induction phase ends when the monomer concentration surpasses n^*, triggering rapid nucleation. At this stage, the nucleation rate surpasses the monomer consumption rate, resulting in a decline in monomer concentration after n_{max}. Following the second n^* event, nucleation slows significantly, and CQD growth becomes the dominant process. MSZ is the monomer saturation zone.

Once the colloidal solution cools down to room temperature, unwanted residues, unreacted reagents, and potential contaminants must be removed through selective precipitation. This involves adding a polar anti-solvent –

here it is acetone, which is miscible with ODE, to induce precipitation of the OEA-capped QDs. By-products and unreacted residues will remain in the solution. The precipitated quantum dots are collected via centrifugation, forming a compact mass at the bottom of the vial, and the supernatant is discarded. The QDs precipitate is then re-dispersed in a fresh polar solvent - here toluene, and the process is typically repeated 2 more times. After the final precipitation, the QDs are dried and re-dispersed in fresh solvent - octane, a solvent in which they remain stable for extended periods of time.

However, these OEA-PbS CQDs are not immediately suitable for solar cell fabrication, as their long, bulky ligands impede charge transport, reducing overall efficiency. Therefore, post-synthetic ligand exchange is necessary to enable the use of CQDs in electronic devices.

Ligand Exchange Reactions and Film Assembly

The high surface area-to-volume ratio of quantum dots significantly influence their surface chemistry and, consequently, their properties. The surface chemistry of QDs is largely dependent on their structure, which varies with the size of the quantum dot.[219] Due to the abundance of surface atoms compared to bulk materials, QDs often have irregular surfaces with many non-passivated bonds. These bonds, if left 'untreated', can lead to surface oxidation and the formation of trap states and defects. At the same time, the selection of too bulky passivating ligands can hinder the effective charge transfer between adjacent QDs, which is the case of oleic acid molecules used in ODs synthesis. Therefore, selecting appropriate surface ligands is crucial for enhancing charge transport while maintaining stability.[220,221]

For the effective charge transfer between adjacent QDs, electrons must tunnel through potential barriers formed by the surface ligands. If these barriers (a.k.a. passivating ligands) are wide and high, exciton lifetimes increase, but tunnelling rates decrease. On the contrary, smaller barriers enhance tunnelling rates but reduce exciton lifetimes. Tunnelling rate also depends on the electronic coupling of QDs, defined by the interaction of electron wave functions between two dots.[222] Enhanced coupling reduces the height and width of the potential barrier, thereby increasing the tunnelling rate and the material's conductivity. Strong QD coupling, though uncommon, is notable in lead chalcogenides and is highly dependent on inter-dot distance and surface chemistry.[223,224] Increased disorder in the system results in greater inter-dot distances, weaker coupling, and limited charge transfer.

Extensive research has been dedicated to enhancing charge mobility and lifetime, while minimizing defects and charge recombination rates in quantum dot devices.[225] In early quantum dot solar cells, various surface ligands such as thiols (e.g. 1,2-ethanedithiol (EDT), mercaptopropionic acid (MPA), amines (e.g. tetrabutylammonium iodide (TBAI)) and halide salts were utilized.[226] The latter ones contributed to the fabrication of the highest performing ODs solar cells to date.[227,228] It is important to highlight that surface ligands can modify the electronic structure and charge distribution within the

QDs. For instance, certain ligands may introduce electron-donating or electron-withdrawing effects, thereby affecting the overall charge carrier concentration. As a result, depending on the nature of the ligands, quantum dots can be tuned to display either p-type behaviour, where there is a predominance of hole carriers, or n-type behaviour, where there is a predominance of electron carriers. This ability to control the electronic properties through ligand selection is crucial for tailoring quantum dots for various applications within solar cells.[226,229]

Ligand exchange reactions are employed to substitute the extended oleic acid ligands with shorter, conductive ligands. In this thesis, two distinct ligand exchange methods are utilized: solid-state ligand exchange (SSLE) and liquid-state ligand exchange (LSLE).

SSLE or solid-state ligand exchange, is a method employed to create conductive colloidal quantum dot films (**Figure 18**). The process begins by spin-coating a solution of PbS CQDs in a non-polar solvent onto a substrate. The resulting thin film is then subjected to immersion in a polar solution that contains shorter conductive ligands for 30 seconds, facilitating the complete exchange of ligands. After the exchange, excess ligands are removed through subsequent washing and spin-coating cycles with the polar solvent. The resulting film typically measures 10-20 nm in thickness. This place-exchange process is repeated multiple times to achieve a film of adequate thickness for CQD solar cells. If a higher concentration of oleic acid-coated CQDs is used to increase the initial thickness of the film, it may result in cracking due to the loss of the longer ligands. This can be mitigated by the application of thinner layers and repeating the process multiple times (min. 10 cycles).

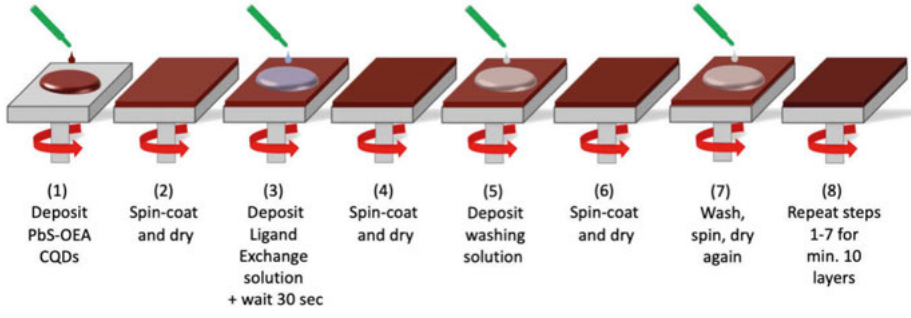

Figure 18. Solid – state ligand exchange (SSLE) process. This process is usually used for deposition of p-type CQDs layers.

In contrast, the LSLE technique (see **Figure 19**) is conducted in a reaction vessel where OEA-PbS CQDs dispersed in a non-polar solvent (octane) are mixed with an immiscible polar solvent (N,N-dimethylformamide (DMF)) containing the new ligands (lead iodide (PbI_2), lead bromide ($PbBr_2$) and ammonium acetate (AAc)) intended to replace the oleic acid ligands. A dilute solution is used to ensure proper dissolution of the exchange species without

reaching saturation. As the result of vigorous stirring, the CQDs are transferred into the polar phase, where the oleic acid ligands are replaced by the new halide ligands. It is clearly visible due to the loss of dark brown colour in the octane phase. The polar DMF solution is then washed with a non-polar solvent (octane or hexane) several times to remove residual oleic acid. The exchanged PbS CQDs need to be concentrated for film deposition. Therefore, a non-polar toluene is added to precipitate the QDs, which are then isolated via centrifugation. The supernatant is discarded, and the QD precipitate is dried into a powder under vacuum. This powder is then re-dispersed in a new volatile solvent (Butylamine ($BuNH_3$)) at a concentration of 200mg/mL. This PbS CQD ink is subsequently spin-coated onto a substrate to produce a film of the desired thickness in a single step.

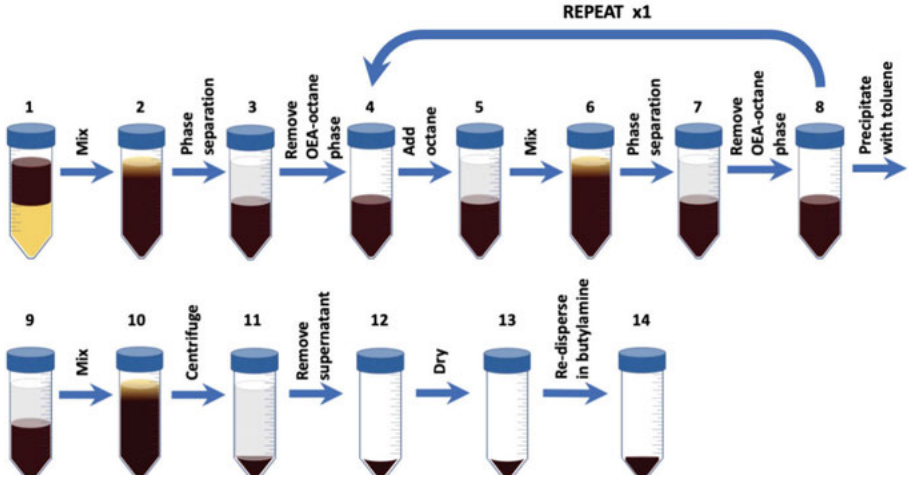

Figure 19. Scheme of liquid state ligand exchange (LSLE) in chronological order.

The solution exchange technique offers several benefits compared to the solid-state method. Large-area processing methods, such as inkjet printing, slot-die casting, and doctor blading, are not well-suited to solid-state ligand exchange (SSLE) due to the laborious and inefficient nature of its sequential soaking and washing steps. Conversely, the solution exchange method generates a concentrated ink that facilitates a more streamlined deposition of colloidal quantum dots (CQDs), making it compatible with both small-scale spin-coating and large-scale deposition processes. Furthermore, this method generally yields higher-performing CQD solar cells, as the repeated soaking steps in SSLE can create additional interface traps that adversely affect device performance.

Aluminium Doped Zinc Oxide Synthesis

The function of the electron transport layer (ETL) is both to extract electrons from the quantum dot layer, as well as, selectively prevent holes from reaching the electrode. ETLs are usually n-type materials with wide band gaps, creating a potential barrier that impedes the movement of holes. This barrier directs the holes towards the metal electrode on the opposite side of the solar cell. As a result, the likelihood of electron-hole recombination within the solar cell is diminished, leading to improved efficiency of the solar cells. The electron transporting materials used in this thesis were aluminium doped zinc oxide (AlZnO or AZO) for CQD-based solar cells and titanium dioxide (TiO_2) for perovskite-based devices.

To fabricate an AZO electron transport layer for the PbS CQDs solar cells, an AlZnO nanoparticles were first prepared. In a standard synthesis procedure, zinc acetate dihydrate ($Zn(Ac)_2 \cdot 2H_2O$) and aluminium nitrate nanohydrate ($Al(NO_3)_3 \cdot 9H_2O$) were combined with ethanol in a three-necked flask. The mixture was then heated to 80°C. To prevent ethanol from boiling off, the cooler was attached to the flask, while allowing ambient air flow to facilitate oxidation. After approximately 30 minutes of reflux at 80°C, ethanolamine was injected. The addition of ethanolamine resulted in the instant dissolution of substrates and solution mixture turning transparent. The nanoparticle growth was continued for 3 hours under 80°C reflux. Subsequently, the AZO solution was cooled to a room temperature, transferred to a vial and stored under ambient conditions until needed.

1,2-Ethanedithiol capped PbS QDs Fabrication

The hole transport layer (HTL) role is reversed comparing to the electron transport layer - it function is to prevent electrons from reaching the metal electrode while selectively allowing holes to pass through. In quantum dot solar cells, the PbS-EDT layer, which acts as the p-type layer within the p-n junction, is commonly designated as the HTL.[229,230] Alternatively, various polymers can also be employed as HTLs for high-efficiency solar cell devices.[121,231]

In case of this thesis the p-type PbS-EDT layers were employed as HTL in CQDs solar cells. They were fabricated using the previously described solid state ligand exchange reaction and its details are presented in **Figure 18.** The difference is that only 2 layers of PbS-EDT were spin-coated using that method (instead of minimum 10 as stated in the Figure 18).

Quantum Dot Solar Cells Fabrication

Over the time, the design of colloidal quantum dot solar cells has evolved from a basic configuration with an absorbing material placed between two electrodes to more intricate multilayered structures.[228] CQD solar cells belong to the thin-film photovoltaics category, similar to perovskite and organic solar cells. These thin-film solar cells are processed in solution, making them easier to prepare with different thick layers for semitransparent solar cells, compared to crystalline solar cells. Furthermore, solution-processed thin-film solar cells can be applied to rounded surfaces and lightweight, flexible substrates, broadening their application spectrum.

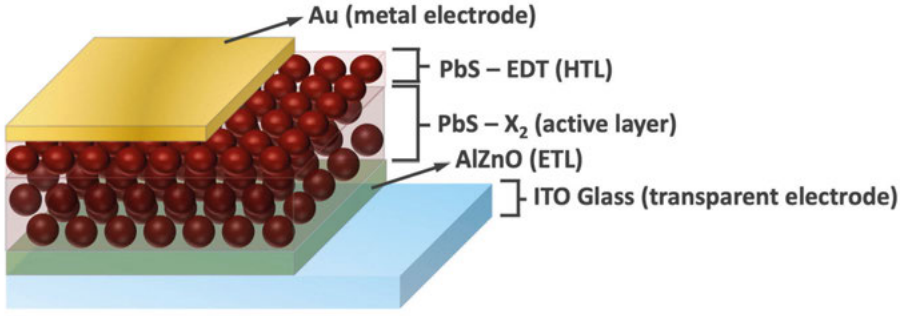

Figure 20. Schematic design of a PbS CQDs Solar Cell.

A colloidal quantum dot solar cell based on the p-i-n heterojunction architecture, used in this thesis, consists of several layers: a transparent conductive oxide (TCO), electron transport layer (ETL), CQD absorbing layer, hole transport layer (HTL), and a top contact (see **Figure 20**).[90,231] The TCO, typically indium-doped tin oxide (ITO), provides the necessary conductivity and transparency for the cell. The ETL is made from n-type wide-bandgap ZnO nanoparticles, which facilitate electron extraction and prevent hole transport. The colloidal quantum dots in the active layer are coated with short conductive ligands, typically halides, to promote charge transport. The HTL comprises p-type EDT-capped PbS CQDs, which support hole transport and block electrons. Lastly, a thermally deposited gold layer serves as the anode for hole extraction. This architectural design has enabled CQD solar cells to achieve power conversion efficiencies (PCEs) of 13.3%.[232]

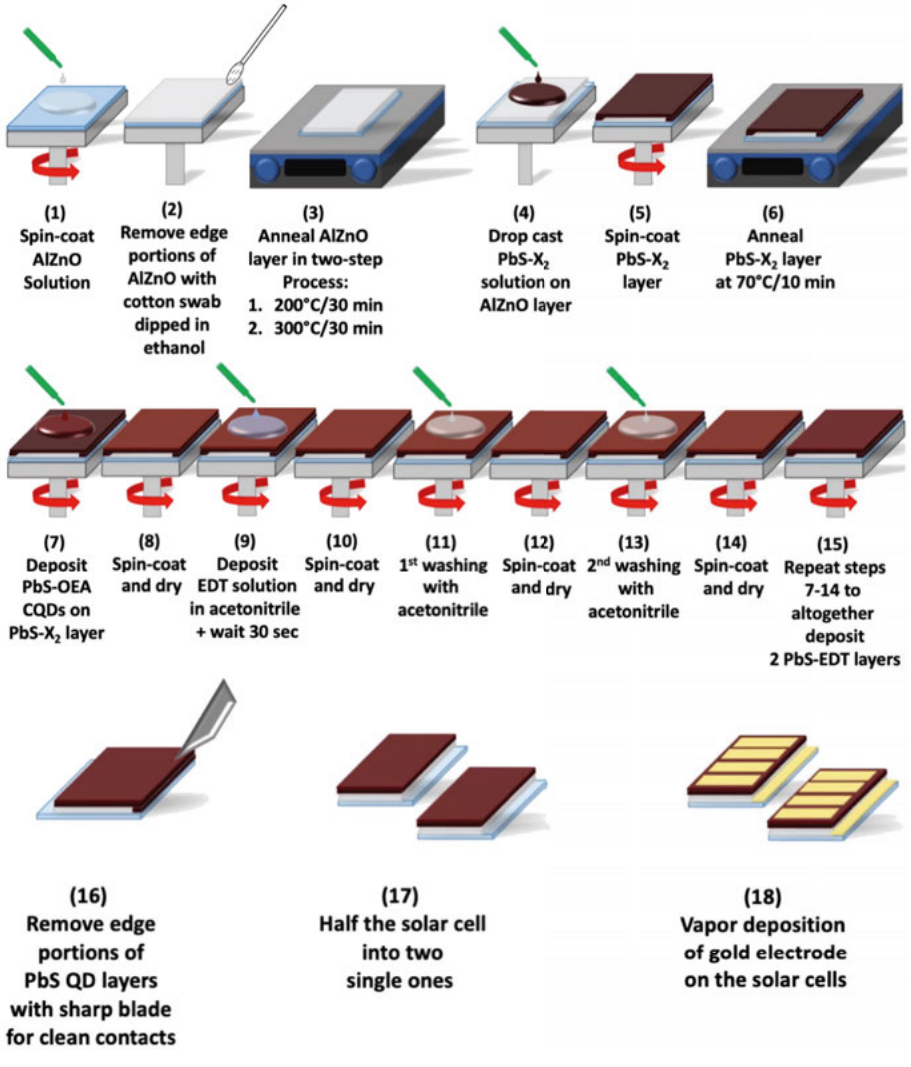

Figure 21. Schematic representation of assembly of the PbS CQD solar cell in chronological order.

Assembling the CQD solar cell essentially consists of constructing a multilayered structure, with each layer carefully chosen and added to achieve the final functional device. The assembly of the solar cell **(Figure 21)** begins with a clean transparent electrode, typically indium-doped tin oxide coated glass. This ITO glass is cut to specific dimensions and etched to minimize the risk of short-circuiting the cell. Etching can be done with zinc powder/2M HCl chemical process or with use of the laser. The ITO glass is then thoroughly cleaned using an ultrasonic bath in three stages with different solvents (10% RBS soap (sodium hydroxide)/water solution, acetone and ethanol) and treated with UV-ozone to fully dispose of any remaining organic contamination. The first layer applied on top of

the ITO is the transparent electron transport layer, which in this thesis was usually aluminum-doped zinc oxide (AZO). The AZO synthesis was already described in one of the previous sections. This solution is spin-coated onto the ITO substrate and carefully cleaned from the edges to later provide the clean contact. Further, the AlZnO layer is annealed at 2-step high temperature (200 and 300°C) to crystallize it into a 30-40 nm thick layer.

Subsequently, the primary absorbing CQD layer, is spin-coated on top of the AZO layer. In case of the solar cells used in this work it is the n-type PbS quantum dots capped with halide ligands (PbS-X_2) of two different diameters. The synthesis of these 2 PbS CQDs and their liquid state ligand exchange processes were detailed in previous sections of 'Experimental' chapter. After the spin-coating of the PbS-X_2 QDs from butylamine solution the film is briefly annealed at 70°C. The thickness of this film is controlled by the solution concentration, spinning speed, and spinning time. Once the main absorbing layer is ready, the p-type PbS-EDT layer is deposited using previously described solid state ligand exchange reaction, forming the p-n junction essential for driving electrons and holes in opposite directions. To reduce short-circuit risk and ensure better contact, the QD layers directly on the ITO are carefully removed with a small sharp blade. Finally, an 80 nm thick gold layer is slowly thermally evaporated on top of the PbS-EDT layer within a metal evaporator.

Perovskite Solar Cell Fabrication

As previously mentioned the perovskite solar cells (PSCs) belong to the same category as CQDs solar cells – thin film photovoltaics. Therefore, their manufacturing process is also solution-processed and they have similar, layered device structure.

The solution-process deposition techniques for perovskite in the leading PSCs can be classified based on the number of steps needed to create the perovskite material. In one-step methods, all the perovskite precursors are dissolved in a single solution and deposited onto a chosen substrate and the perovskite material forms as the solvent evaporates. Two-step methods, on the other hand, involve the sequential addition of perovskite precursors to form the desired perovskite. The perovskite solar cells used in this thesis were all prepared with one-step method. One-step methods were the initial manufacturing processes developed for solid-state perovskite solar cells.[179,180] Their primary advantage is simplicity, involving the fewest possible steps, while also providing precise compositional control. The general procedure for a one-step method includes first dissolving all precursor materials in a single solution to create a perovskite ink, followed by coating the substrate with the perovskite ink and lastly removing the solvent to crystallize the perovskite. While perovskite can form directly through solvent removal, this process is usually boosted by annealing the perovskite film at a specific temperature. This

additional step helps complete the reaction and improves the crystal quality and film morphology.

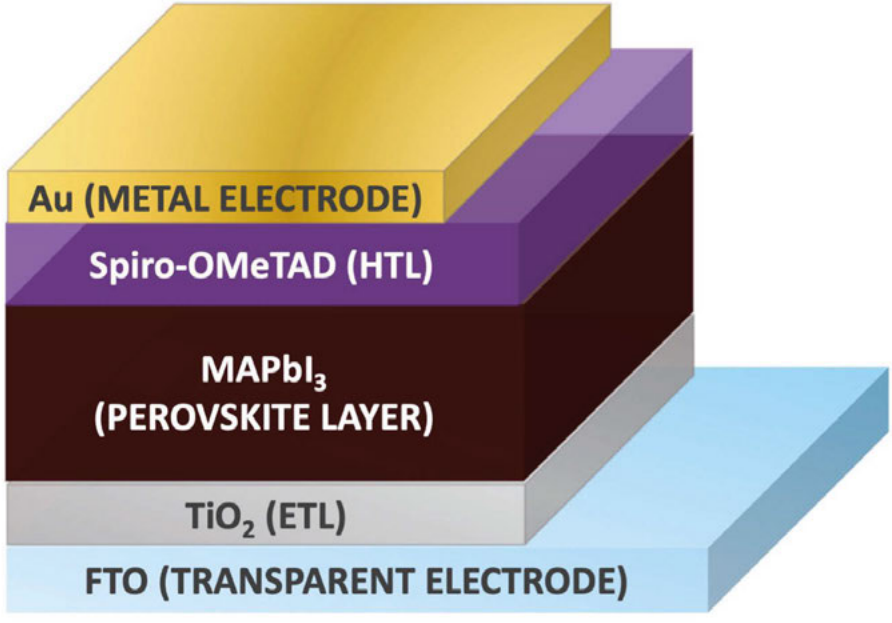

Figure 22. Schematic design of a perovskite solar cell.

The perovskite solar cells used in this thesis are devices with n-i-p planar architecture. Similarly to the colloidal quantum dot solar cells, consists of several layers, including a TCO (typically Fluorine-doped tin oxide (FTO)), ETL (compact and mesoporous titanium dioxide (TiO_2)), perovskite absorbing layer (here Methylammonium lead iodide ($MAPbI_3$/MAPI)), HTL (Spiro-OMeTAD), and a top contact (typically gold (Au)) (see **Figure 22**). The function of each of these layers is equivalent to the description within the 'Quantum Dot Solar Cells Fabrication' section. The detailed assembly of the $MAPbI_3$ perovskite solar cell is described below.

First step of PSC fabrication starts with etching and cleaning of the fluorine-doped tin oxide (FTO) glass (Pilkington TEC 15, 15 Ω/sq). The FTO glass is first cut and covered with tape, leaving areas of the FTO exposed. Zinc powder is then evenly applied to the exposed FTO surface, followed by the addition of 2M HCl. The etching reaction is completed within 3 minutes and followed by the 3-step ultrasonic cleaning process. First substrates were cleaned with 10% RBS soap (sodium hydroxide)/water solution, followed by acetone and ethanol. Each step was lasting 30 minutes. Next step is the deposition of the electron transporting layer composed of compact and mesoporous TiO_2. The precursor solution for compact TiO_2 layer was composed of titanium diisopropoxide bis(acetylacetonate) and ethanol. The TiO_2 was

deposited using a spray-pyrolysis technique, where the solution was sprayed onto the heated FTO substrate (at 500 °C) to form a compact TiO_2 film and further annealed at that temperature for 30 minutes. After cooling down, the previously prepared mesoporous TiO_2 solution (TiO_2 paste (30 NR-D) dispersed in ethanol and sonicated for 2 hours) was evenly spin-coated on top of compact TiO_2 layer. The substrates were then annealed at 500°C for 30 min and then cooled down, resulting in the ready TiO_2 ETL. After the ETL is ready, the $MAPbI_3$ perovskite absorber layer is deposited next. This step is carried out inside the nitrogen (N_2) glovebox to ensure the optimal conditions for the perovskite film crystallization and prevent the premature crystallization. The perovskite precursor film is prepared ahead by dissolving the lead iodide (PbI_2) and methylammonium iodide (CH_3NH_3I/MAI) in a N,N-dimethylformamide (DMF) and Dimethyl sulfoxide (DMSO) solvent mixture (4:1 volume ratio). The perovskite solution is then spin-coated on top of the TiO_2 layers, where halfway through, the chlorobenzene is dynamically dropped onto substrate as the antisolvent treatment. Such fabricated substrates are then annealed at 90°C for 30 minutes. The hole transporting layer, in form of Spiro-OMeTAD, is applied in the next step on top of the perovskite absorbing layer. This stage is also carried out in the N_2 glovebox. The Spiro-OMeTAD solution was prepared beforehand by dissolving Spiro-OMeTAD ($C_{81}H_{68}N_4O_8$) in chlorobenzene. Next, a 4-tertbutyl-pyridine, lithium bis(trifluoromethanesulfonyl)imide solution in acetonitrile and tris(2-(1H-pyrazol-1-yl)-4-tert-butylpyridine)cobalt(III) tri[bis(trifluoromethane)sulfonimide] (FK 209 Co(III)-TFSI salt) solution in acetonitrile were added. Such mixture is then spin-coated on top of perovskite films. After that, the samples are kept in the dark and ambient atmosphere for oxidation. Lastly, the 80 nm Au layer is slowly thermally evaporated on top of the ETL.

Characterisation techniques

UV-Vis-NIR Spectroscopy

Ultraviolet-Visible-Near-infrared absorption spectroscopy (UV-Vis-NIR) is an essential technique for analyzing the optical properties of materials through processes such as absorption, transmission, reflection, and scattering. These optical properties significantly affect a semiconductor's performance in applications like solar cells, determining the spectral regions where effective light harvesting occurs. Absorption measurements in the UV-Vis-NIR range (200-2000 nm) are crucial for understanding a solar cell's and its components interaction with sunlight.

A typical UV-Vis-NIR spectrometer includes one or more light sources to cover the desired spectral regions, monochromators to select specific wavelengths, a sample chamber, and a photodiode detector. Absorption measurements involve evaluating the light intensity across various wavelengths as it

passes through a sample. The Beer-Lambert Law describes light absorption in solutions with the formula:

$$A = log_{10}\left(\frac{I_0}{I}\right) = \varepsilon cl \tag{17}$$

where A is the absorbance, I_0 is the incident light intensity, I is the transmitted light intensity, ε is the molar extinction coefficient, c is the concentration, and l is the path length.[233]
For solid-state films, absorbance is described by:

$$A = log_{10}\left(\frac{I_0}{I}\right) = \alpha d \tag{18}$$

where α is the absorption coefficient and d is the film thickness.

To fully characterize the optical properties of solid materials, including components or complete solar cells, it is important to measure both transmittance (T_λ) and reflectance (R_λ). Transmittance measurements assess the amount of light passing through the sample, while reflectance measurements determine the amount of light reflected from the sample. Absorptance (A_λ) can be calculated by:

$$A_\lambda = 1 - T_\lambda - R_\lambda \tag{19}$$

where T_λ and R_λ are transmittance and reflectance, respectively, in fraction form.

In this study, UV-Vis-NIR absorption spectra were obtained using a Perkin Elmer Carry 5000 spectrophotometer with baseline correction and transmittance spectra was measured with Perkin-Elmer Lambda 900 spectrometer. The analysis covered the wavelength range from 200 to 2000 nm to evaluate the absorption characteristics of thin films.

Photoluminescence Spectroscopy

Photoluminescence spectroscopy is another crucial technique for characterizing the optical properties of semiconducting materials, especially QDs. When a semiconducting material absorbs a photon, an electron is excited from the valence band (VB) to the conduction band (CB). In the absence of an external circuit to extract the charge, the excited electron can return to its ground state through two possible mechanisms: non-radiative or radiative recombination.

Radiative recombination involves the emission of a photon with energy corresponding to the material's band gap (E_g). A strong photoluminescence (PL) signal from a material indicates minimal non-radiative recombination pathways, such as surface defects, suggesting high material quality. The presence of strong PL is thus highly desirable as it implies efficient radiative recombination and fewer defects within the material.

In steady-state photoluminescence spectroscopy, continuous illumination with monochromatic light of higher energy than the material's band gap generates electron-hole pairs. The recombination of these pairs results in the emission of photons, which are then measured to produce the emission spectrum. A second monochromator, positioned perpendicularly to the incident light, is used to collect and analyze the emission spectrum of the sample. This setup allows for the precise measurement of the photoluminescence emitted by the material.[234] While this method is often used to characterize quantum dots, it is important to note that the Stokes shifts, which varies with dot size, can make size determination using this method challenging.[235,236] The peak position in the emission spectrum does not directly correspond to the band gap value due to this shift.

Despite this limitation, photoluminescence spectroscopy remains valuable for detecting flaws in quantum dot solutions. The emission peaks of quantum dots are typically narrow and symmetrical, making this technique highly sensitive in terms of detection limits and chemical specificity.[234] This sensitivity makes photoluminescence spectroscopy an essential tool in the characterization and quality assessment of semiconductor materials. By employing photoluminescence spectroscopy, an insight into the efficiency of radiative recombination is gained and identifying potential material defects become possible, thereby advancing the development and optimization of these materials for various applications.

In this thesis the steady-state photoluminescence of various QDs samples was obtained with FLS1000 Photoluminescence Spectrometer. The details can be found in specific papers.

Currrent-Voltage (J-V) Measurements under Simulated Solar Light

The current-voltage (J-V) characteristics of a solar cell under illumination provide crucial insights into its performance, specifically its power conversion efficiency (PCE or η). These measurements are fundamental to understanding the behavior of solar cells under operating conditions and are integral to evaluating their practical applicability. To determine the PCE of a solar cell, its current-voltage characteristics are measured under simulated solar illumination. This involves shining light on the solar cell and recording the current generated as a function of applied bias voltage across its contacts. The current is normalized to the active area of the solar cell, resulting in a current density (J) versus voltage (V) curve, known as the J-V curve.

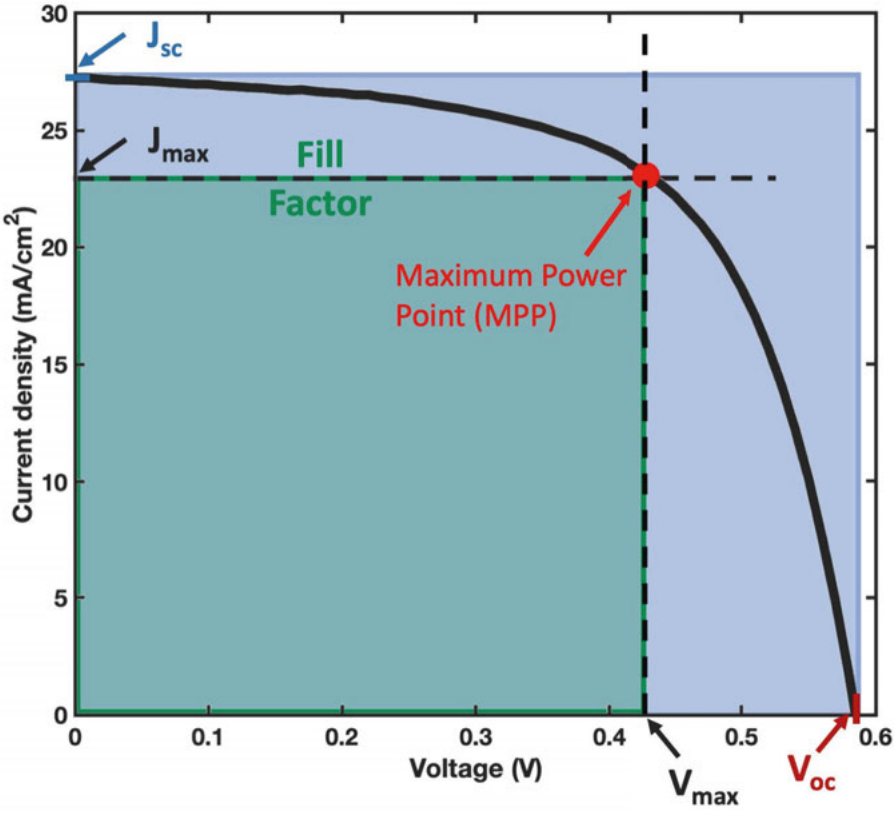

Figure 23. Current-voltage characteristic of a solar cell under illumination with highlighted key photovoltaic parameters.

The J-V curve is analyzed to extract several key parameters: the short-circuit current density (J_{sc}), the open-circuit voltage (V_{oc}), the fill factor (FF), and the maximum power point (MPP) (**Figure 23**). The J_{SC} is the current density when the voltage across the solar cell is zero, indicating the maximum current the cell can produce and is influenced by the cell's photoabsorber properties, such as its absorption spectrum and bandgap energy (E_g). The V_{oc} is the voltage at which the net current through the solar cell is zero, representing the maximum voltage the cell can achieve and is affected by the recombination of charge carriers within the cell. The FF is the ratio of the maximum power output (P_{max}) to the product of J_{sc} and V_{oc}, providing insight into the quality of the solar cell and indicating charge-carrier collection efficiency and potential recombination losses. The MPP is the point on the J-V curve where the product of current and voltage is maximized, and the power at this point, P_{max}, is crucial for determining the cell's operational efficiency. The power conversion efficiency of a solar cell is calculated as the ratio of the maximum power output to the incident illumination power (P_{in}):

$$PCE = \frac{P_{max}}{P_{in}} = \frac{J_{sc} \cdot V_{oc} \cdot FF}{P_{in}} \quad (20)$$

The efficiency and performance of a solar cell are also affected by parasitic resistances. Series resistance (R_s) arises from the slow extraction of carriers from the interfaces and should be minimized to ensure efficient charge collection. Shunt resistance (R_{SH}) should be high as it indicates good carrier blocking and minimal leakage current paths.

When measuring the J-V characteristics of solar cells, it is essential to account for hysteresis effects. Hysteresis refers to the dependence of the J-V characteristics on the direction and speed of the voltage scan, which can lead to anomalous and inconsistent PCE values. To mitigate this, the J-V curve should be measured at a slow scan speed (typically ≤10 mV/s) and in both forward and reverse directions. This approach minimizes the influence of transient effects and ensures a more accurate representation of the solar cell's performance.

In this thesis, the J-V scans are carried out using a self-calibrating WaveLabs SINUS-70 solar simulator with UV and IR range extenders and the current-voltage response was measured with an Ossila X200 sourcemeter. A value of 1000 W/m^2 illumination intensity (1 sun equivalent) is used as a standardized value for testing solar cells. Some solar cell devices were also measured at different light intensities and specifications for that can be found in the relevant papers. In all J-V measurements a black masking was applied on top of the cell with an aperture of 0.065 cm^2 for all PbS CQDSC and of 0.125 cm^2 for all $MAPbI_3$ solar cells. The J-V scans speeds was set to 10 mV/s.

Incident Photon-to-Current Efficiency (IPCE)

Incident photon-to-current efficiency (IPCE), also known as external quantum efficiency (EQE), is another typical characterization method for solar cells. It measures the efficiency with which a solar cell converts incident photons at a specific wavelength into electrical current. In an IPCE measurement, the solar cell is irradiated with monochromatic light, and the resulting current output at that wavelength is monitored. By knowing the incident photon flux, which is the number of photons striking the solar cell per second, the IPCE at that wavelength can be calculated using the following equation:

$$IPCE(\lambda) = \frac{J_{sc}(\lambda)}{e \cdot \varphi(\lambda)} = \frac{J_{sc}(\lambda)}{e \cdot P_{in}(\lambda)} \cdot \frac{hc}{\lambda} = \frac{1240 \cdot J_{sc}(\lambda)}{\lambda \cdot P_{in}(\lambda)} \quad (21)$$

where, e is the elementary charge, φ is the photon flux, h is the Planck constant, c is the speed of light and λ is the light wavelength. The IPCE spectrum of a solar cell depends heavily on the optical properties of the photo-absorbing material and the other layers within the device.

For example, in an IPCE spectrum of a typical solar cell, current generation starts at a wavelength consistent with the bandgap (E_g) of the photo-absorbing

material. All photons with energy higher than the E_g can be absorbed by the material. However, due to the optical properties of various layers in the solar cell and thermodynamic losses, the IPCE spectrum often does not form a perfect square shape. A cut-off in the ultraviolet (UV) range might be observed due to absorption by certain layers, such as ETL or the glass substrate, which generally does not significantly affect performance under sunlight since there are few photons in the UV range in the solar spectrum. However, a downward slope in the visible (Vis) range may indicate charge-collection problems at the back contact or issues with back reflection. Near-infrared (NIR) wavelengths, compared to shorter wavelengths, are typically absorbed deeper in the material due to a lower absorption coefficient. Enhancing back-contact charge collection and increasing the reflective properties of the back contact can help improve the absorption of longer wavelengths in the bulk material.

The expected short-circuit current density (J_{sc}) of the device can be estimated by integrating the solar cell's IPCE with the AM1.5G solar spectral irradiance (I_s) using the equation:

$$J_{sc} = \int PCE(\lambda) \cdot I_s(\lambda) \cdot d\lambda \tag{22}$$

Under most conditions, the J_{sc} value derived from an IPCE measurement should match well with the value obtained from a J-V measurement using a light source with an AM1.5G spectrum. However, discrepancies may occur due to non-linear current responses of the solar cell to varying light intensities. This happens because the monochromatic irradiance of the IPCE instrument is typically a fraction of what is received under 1 sun illumination. To mitigate this, a white-light bias can be used to effectively irradiate the solar cell with 1 sun illumination intensity. A modulated monochromatic light source is then used to measure the cell's response at each wavelength.

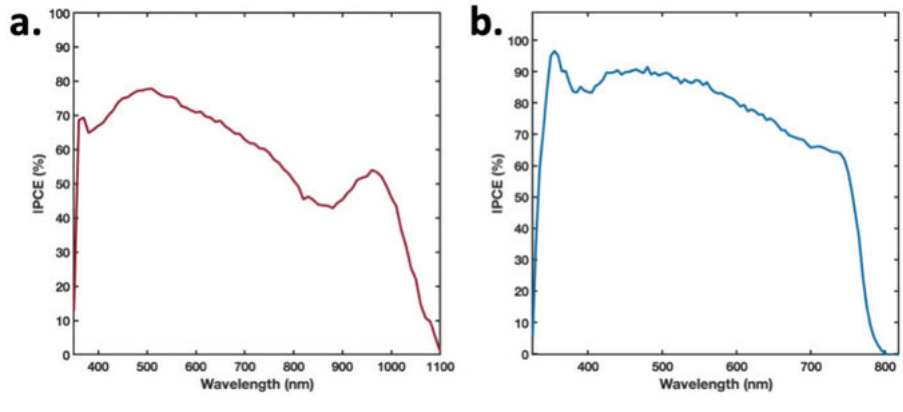

Figure 24. Examples of the incident-photon-to-current conversion efficiency for **(a)** PbS CQD solar cell and **(b)** $MAPbI_3$ perovskite solar cell.

In this thesis, all IPCE measurements were conducted using a computer-controlled system involving a xenon lamp (Spectra Products ASBXE 175), a monochromator (Spectra Products CM110), a LabJack U6, and a potentiostat (PINE AFRDE 5). Measurements were carried out following calibration with a certified reference solar cell from Fraunhofer ISE.

Transient Photoelectrical Measurements

In the characterization of solar cells, transient photovoltage and photocurrent rise or decay measurements are important techniques for understanding the dynamics of charge carriers, including their transport and recombination processes. These methods are particularly valuable in the study of advanced solar cell materials, where charge carrier dynamics significantly influence device performance.

Transient photovoltage decay measurements assess the electron lifetime by observing the decay of the open-circuit voltage (V_{oc}) in response to a modulated light source. This technique involves illuminating the solar cell with an LED whose intensity is precisely controlled and modulated. The modulation is achieved by applying a small voltage fluctuation to the LED, creating a square wave pattern with a specific frequency. The resulting transient voltage response is recorded and analyzed. The electron lifetime obtained from this measurement reflects the average time electrons and holes generated in the light-absorbing film take to recombine. It is a crucial parameter for assessing the recombination processes within the solar cell. The carrier lifetime is influenced by the quality of the material and the presence of defects or traps. For instance, perovskite materials, known for their excellent crystallinity, can exhibit carrier lifetimes up to milliseconds, contributing to their high photovoltaic performance. As light intensity decreases, the carrier concentration decreases, leading to longer carrier lifetimes due to reduced recombination rates.

Similarly, transient photocurrent rise or decay measurements focus on the electron transport properties by monitoring the rise or decay of the short-circuit current (J_{sc}) after a light pulse. The setup is identical to that used in photovoltage measurements, with the primary difference being that the short-circuit current response is measured instead of the voltage. The electron transport time obtained from this measurement indicates how long charge carriers persist within the device and the time they take to reach the contacts. This is critical for understanding the mobility and efficiency of charge collection in the solar cell. Both techniques provide valuable data on the carrier dynamics within the solar cell.

Light intensity dependent measurements

The open-circuit voltage and short-circuit current responses to light intensity variations can be analyzed using the Schottky equation:

$$V_{oc} = \frac{nkT}{q} ln\left(\frac{J_{sc}}{J_0}\right) = \frac{nkT}{q} ln\left(P_{light}{}^{\alpha}\right) + C \tag{23}$$

where J_0 is the dark saturation current, P_{light} is the illumination intensity, α is an empirical parameter, n is the ideality factor, and C is a constant.

The α parameter, also referred to as the power factor, relate the short-circuit photocurrent and light intensity according to following relationship $J_{sc} \propto P_{light}{}^{\alpha}$ and can be calculated from the slope of this plot. The α factor is an indicator of the degree of charge extraction completion and the extent of recombination losses. When α = 1 the charge extraction is completed efficiently without significant losses in the photocurrent due to recombination processes. If α < 1, it suggests that the recombination is significantly influencing the charge extraction, making it incomplete, which can limit the efficiency of the solar cell. The last case of α >1 is less common and may indicate complex mechanisms in the device that enhance charge carrier extraction at higher light intensities.

Another important parameter, that can be extracted from the Schottky equation, is ideality factor (n). It is an indicator of the dominant recombination mechanism and it can be estimated from the from linear regression of V_{oc} as function of light intensity plots. An ideality factor (n) of 1 signifies that the solar cell operates according to the ideal Shockley diode equation, implying that recombination is primarily due to direct band-to-band processes. When the ideality factor ranges between 1 and 2, it typically indicates the presence of Shockley-Read-Hall (SRH) recombination, also known as trap-assisted recombination. These traps can either facilitate or hinder charge transport depending on their nature.

In this thesis the Transient photovoltage and photocurrent measurements were measured using the DSC Toolbox (Dyenamo, Sweden). The solar cells were illuminated with a 1W white LED, with changeable light intensity (0.2, 0.4, 0.6, 0.8 and 1 sun). These measurements were also conducted at elevated temperatures, which was controlled using the Peltier element.

Femtosecond Transient Absorption

Femtosecond Transient Absorption (fs-TA) measurement is a complex technique used to investigate the dynamic processes occurring in materials on extremely short timescales, typically ranging from femto (10^{-15}) to nanoseconds (10^{-9}). This method provides insights into the ultrafast electronic, vibrational, and structural dynamics of a sample by probing its transient optical properties. It is invaluable for studying ultrafast processes in a range of materials, including semiconductors and nanomaterials.

The technique involves the use of a femtosecond laser pulse to excite the sample, which generates a transient population of excited states. Following this excitation, a second probe pulse, delayed relative to the excitation pulse, is used to measure the changes in absorption that occur as the sample evolves over time. The difference in absorbance between the excited and ground states is detected, allowing for the observation of various transient phenomena.

In a typical transient absorption experiment, the sample is illuminated by a femtosecond laser pulse that initiates the electronic excitation. A series of

probe pulses, which are time-delayed relative to the excitation pulse, are then used to monitor the sample's response at different time intervals. By analyzing the changes in absorption as a function of the delay time, the map out of the temporal evolution of excited states, such as charge carrier dynamics, energy transfer processes, and chemical reactions can be performed.

In this thesis the fs-TA measurements were performed for a series of PbS CQDs samples of varying size and coated with assorted ligands, as well as for the multi-layered films assembled from these PbS CQDs. Here, the femtosecond transient absorption experiments employed a Ti regenerative amplifier (Libra, Coherent) to produce the laser output. The 800 nm pulse (3 kHz, ~1.5 mJ/pulse) was split into pump and probe beams and directed into the UV–vis/NIR sample chamber (TAS, Newport Corp.). The 750 nm pump beam was created using optical parametric amplifiers (TOPAS-prime/TOPAS-NIRU-Vis, Light Conversion). A phase-locked chopper reduced the pump beam's repetition rate from 3 kHz to 1.5 kHz, and its intensity was controlled with a neutral density filter before it reached the sample. Broadband UV-Vis/NIR probe beams were generated by focusing approximately 1 μJ of the fundamental pulse onto calcium fluoride (CaF_2) and yttrium aluminum garnet (YAG) crystals. After passing through the sample (with a 2 mm path length for dispersed quantum dots), the probe was focused onto an optical fiber leading to an MS260i spectrometer (Newport Corp.). Films were illuminated from the sample side, except during control measurements where the films were rotated 180 degrees (SI).

Time-Resolved Spectroscopy Techniques

Time-resolved spectroscopy techniques are powerful tools for studying charge dynamics in devices such as solar cells, transistors, and light-emitting diodes. Understanding charge transfer and charge dynamics within these materials is not only of fundamental interest but is also essential for advancing real device applications. Numerous reports have utilized ultrafast spectroscopy to investigate the details of charge carrier generation dynamics and electron–hole separation. However, such methods often lack the element-specific resolution necessary to fully unravel interfacial charge transfer and recombination mechanisms in complex heterostructures.

Time-resolved photoelectron spectroscopy (TRPES), particularly when employing synchrotron-based X-ray source, overcomes these challenges by providing access to element-specific and site-specific electronic dynamics. This technique allows researchers to explore energy levels and charge carrier transitions at femtosecond timescales, delivering unprecedented insight into charge transport and recombination processes.

In a typical TRPES experiment, the sample is excited using an ultrafast laser pulse, inducing photoexcitation or charge carrier generation. Time-delayed probe pulses are then used to eject photoelectrons, whose kinetic energy and angular distribution are analyzed across time delays to construct a detailed temporal and spatial map of charge carrier dynamics, interfacial energy

alignments, and electronic transitions. This enables precise tracking of charge transfer, trapping, and recombination with high temporal resolution.

Despite its advantages, TRPES requires highly sophisticated equipment and infrastructure, such as ultrafast laser systems and synchrotrons, which can limit its accessibility. Nonetheless, in the context of quantum dot solar cells, TRPES provides a unique ability to track interfacial charge transfer and carrier lifetimes, offering critical insights for improving device efficiency and stability.

Results and discussion

Quantum dot solar cells have emerged as a promising technology due to their tunable bandgap, solution-processability, and potential for high power conversion efficiencies. The unique properties of QDs, particularly in the infrared spectrum, make them ideal candidates for tandem solar cells, where multiple sub-cells are stacked to capture a broader range of the solar spectrum. The research presented here explores various aspects of QDSC technology, from material optimization to device architecture, all aimed at enhancing the performance of tandem solar cells.

Project I: Integration of PbS Colloidal Quantum Dot Solar Cells into Tandem Applications

The pursuit of efficient solar energy conversion is crucial in addressing global energy challenges and combating climate change. As the demand for sustainable energy solutions grows, innovative approaches to solar cell technology become essential. Here, results from **Paper I**, **Paper II** and **Paper III** are demonstrated, where the integration of quantum dot (QD) solar cells within tandem configurations is emphasized to enhance overall power conversion efficiency by effectively capturing a broader spectrum of solar radiation.

Paper I lay the groundwork by exploring the combination of PbS CQD solar cells with the dye-sensitized solar cells (DSSCs), in a four-terminal (4T) tandem configuration. This study investigates how the tandem structure, comprising a DSSC top-cell and a PbS CQDSC bottom-cell, can capture a broader spectrum of sunlight in comparison to its single-junction sub-devices, and optimize light utilization and enhance overall energy conversion efficiency. Building on this, **Paper II** delve into similar tandem integration of PbS CQD SCs, but this time with perovskite solar cells, successfully demonstrating the potential for improved light absorption across visible and near-infrared wavelengths. Lastly, **Paper III** investigates the application of QD and perovskite cells in capturing thermal radiation emitted from energy storage materials at high temperatures, addressing traditional limitations in thermophotovoltaic systems. Collectively, these studies highlight the versatility of quantum dot solar cells in various tandem photovoltaic configurations, setting the stage for

a detailed exploration of their performance, interlayer modifications, and synergistic effects on solar energy harvesting.

Paper I: Four-Terminal Tandem Solar Cell with Dye-Sensitized and PbS Colloidal Quantum-Dot-Based Sub-cells

In this work, we investigated the potential of utilizing a combination of a DSSC and a lead sulfide colloidal quantum dot solar cell to create a high-performance four-terminal tandem solar cell. By integrating these two distinct photovoltaic technologies, we aimed to effectively harvest a broad range of wavelengths emitted from the sun, thereby enhancing the conversion efficiency. Our research explores the performance of the tandem device under one-sun illumination (AM 1.5) while evaluating three different dye mixtures (Y123, XY1, and XL) and three varying sizes of PbS CQDs with peak absorbance at 790 nm, 890 nm, and 940 nm.

The architecture of the four-terminal tandem solar cell includes the DSSC as the top-cell, which captures visible light, and the PbS CQDSC as the bottom-cell, designed to absorb near-infrared light. Our approach builds on existing research that has demonstrated the effectiveness of various top-cell materials combined with PbS sub-cells, with notable results previously achieved with CdTe/PbS and PbS/PbS structures. However, to our knowledge, the DSSC/PbS tandem structure had not been investigated prior to this work.

Device Fabrication and Interlayer Optimization

To fabricate the DSSC, we employed a structure comprising FTO/c-TiO_2/mp-TiO2/dye integrated with a redox electrolyte and PEDOT/FTO back contact. The PbS CQDSC was constructed using the ITO/AZO/PbS−PbI_2/PbS-EDT/Au architecture, with the PbS−PbI_2 layer deposited via a one-step solution method after ligand exchange. The schematic of the four-terminal tandem solar cell is presented in **Figure 25a**.

Typically, DSSCs incorporate a TiO_2 light scattering layer to enhance light absorption. However, this layer is not transparent and thus limits the transmission of light to the PbS CQDSC. To improve this transmission, we removed the TiO_2 scattering layer, resulting in an increase in transmission from less than 30% to over 40%, primarily due to the reduced reflectance (see **Figure 25b**). The main loss in transmission can be attributed to the poor transmittance of the PEDOT back contact, which caused more than 30% optical losses.

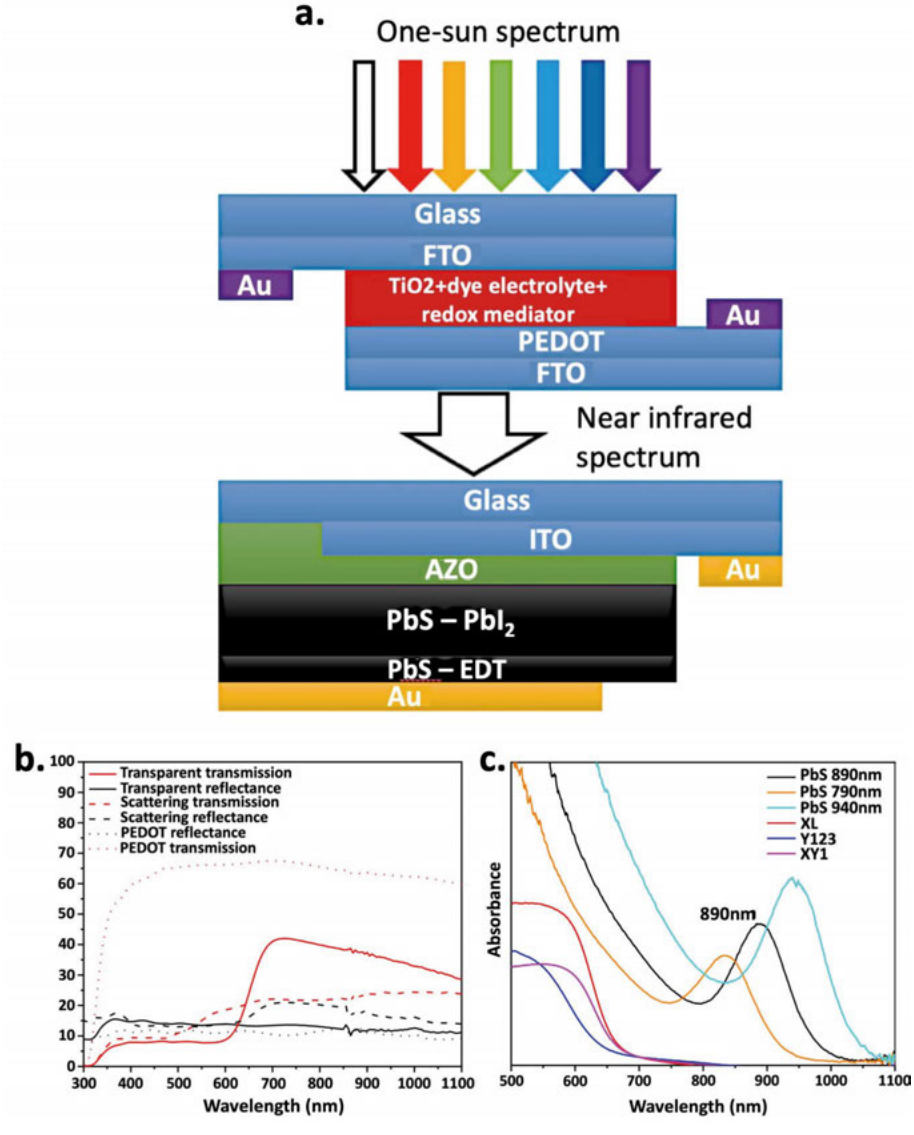

Figure 25. (a) Schematic of the four-terminal tandem structure based on the DSSC and CQDSC. **(b)** Transmission, reflectance, and absorption spectra for XL DSSCs with and without the scattering layer. **(c)** UV–vis–NIR absorbance for different dye mixtures and quantum dots with different sizes. Figure adapted from **Paper I**.

Performance of Dye-Sensitized Solar Cells

We compared the performance of DSSCs with various dye combinations and analyzed the impact of the removal of the scattering layer. As shown in **Figure 26**, the PCE of the DSSCs with different dyes was affected. With the removal of the scattering layer, the PCEs of XL, XY1, and Y123 dyes decreased from 10.20%, 9.0%, and 8.11% to 8.85%, 7.17%, and 7.19%, respectively. The

primary reason for the reduced efficiency in the Y123 dye was its lower light absorption; thus, the absence of the scattering layer decreased the short-circuit current density (J_{sc}).

In contrast, while the XY1 dye offered better light absorption, the removal of the scattering layer resulted in a reduction in fill factor (FF), adversely affecting the overall efficiency. Utilizing a dye cocktail of XY1 and L1 significantly enhanced light absorption, mitigating the impact of removing the scattering layer on J_{sc}.

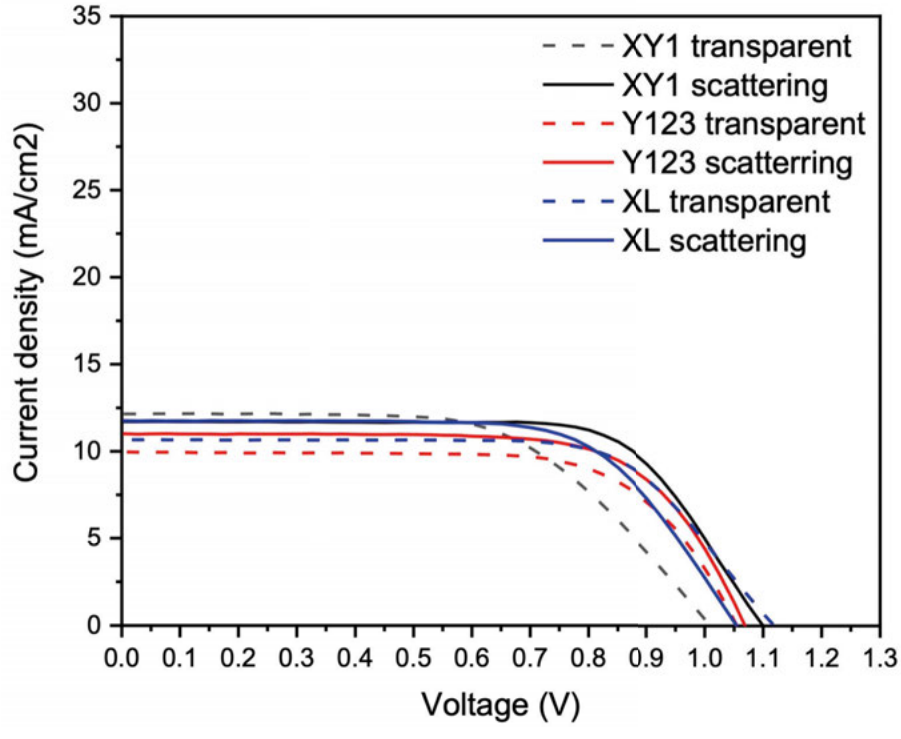

Figure 26. Current–voltage (J–V) measurements under illumination (1000 W/m^2, AM 1.5G) for DSSCs with different dye combinations both for devices with a scattering layer ("scattering") and for devices without the scattering layer ("transparent"). Figure adapted from **Paper I**.

Performance of PbS Colloidal Quantum Dot Solar Cells

Following the assessment of DSSC performance, we measured the efficiency of PbS CQDSCs using different sizes of quantum dots. As illustrated in **Figure 27a**, without the top-cell, the highest PCE for the PbS CQDSCs was recorded at 10.85% for devices with CQDs absorbing at 890 nm.

Upon stacking the DSSC top-cell onto the CQDSCs, the PCEs of the PbS CQDSCs diminished to 3.64%, 1.82%, and 1.78% for the CQDs with absorption at 890, 940, and 790 nm, respectively. This significant performance drop was primarily due to reduction in J_{sc}, as the incident photon-to-current

efficiency (IPCE) indicated that the visible light blocked by the DSSC top-cell accounted for over 60% of the J_{sc} in the CQDSC (see **Figure 27b**).

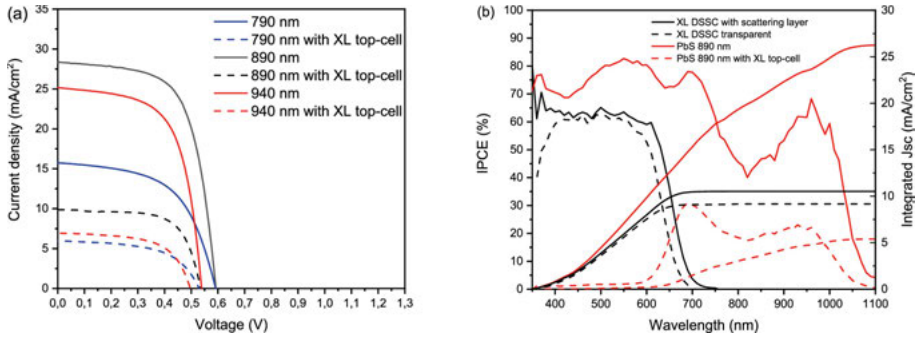

Figure 27. (a) Current density–voltage (J–V) measurements under illumination (1000 W/m^2, AM 1.5G) for different size PbS CQDSCs with and without the XL DSSC top-cell. **(b)** IPCE and calculated J_{sc} of XL DSSC and 890 nm PbS CQDSC under different conditions. Figure adapted from **Paper I**.

By combining the XL DSSC top-cell with the CQDSC bottom-cell based on CQDs absorbing at 890 nm, we achieved the highest overall efficiency of 12.37% for the four-terminal tandem system. This result represents approximately a 7.4% increase relative to the single-junction PbS CQDSC and a 41% enhancement compared to the standalone DSSC (see **Table 1**). The data demonstrate that the integration of the DSSC with the CQDSC leads to significantly improved performance, primarily due to better utilization of infrared light.

Table 1. Performance of single cells and of subcells in the four-terminal tandem solar cell, and the total efficiency of the four-terminal tandem solar cell

	V_{oc} (mV)	J_{sc} (mA/cm^2)	FF (%)	PCE (%)
Single XL DSSC with scattering layer	1050	12.90	75.0	10.20
Single PbS CQDSC (based on CQDs with 890 nm abs. peak)	592	28.33	64.7	10.85
Single XL DSSC without scattering layer	1018	12.30	71.0	8.85
PbS CQDSC as bottom-cell (with XL DSSC as top-cell)	534	9.88	66.7	3.52
4-terminal tandem solar cell based on the XL DSSC (without scattering layer) and PbS CQDSC (based on CQDs with 890 nm abs. peak)	-	-	-	12.37

Conclusions

Although we achieved significant performance improvements, we recognize that further work is required to optimize the light management within the DSSC to reduce infrared light reflection and absorption. Moreover, the rather similar current outputs from both the DSSC and PbS CQD cells suggest the potential for developing a two-terminal tandem structure in future iterations.

In conclusion, we successfully demonstrated a high-performance four-terminal tandem solar cell by employing a DSSC as the top-cell and a PbS CQD solar cell as the bottom-cell. We explored three different dye types (XL, XY1, and Y123) and three distinct PbS CQDs with varying absorption peaks (790 nm, 890 nm, and 940 nm). The PbS CQDSC with a peak absorption at 890 nm exhibited the best performance, leading to relative efficiency increases of approximately 41% for the XL dye, 21% for XY1, and 31% for Y123.

Beyond these specific findings, this work highlights the potential of QD-based tandem solar cells as a promising route for next-generation photovoltaics. The demonstrated integration of DSSCs and PbS CQDSCs underscores the versatility of QDs in tandem architectures, while insights into dye selection, QD absorption tuning, and interfacial optimization can inform future research on hybrid solar cells. Further advancements in charge transport, QD compositions, and device design will be essential for enhancing the efficiency and stability of QD-based photovoltaics.

Paper II: Perovskite and quantum dot tandem solar cells with interlayer modification for improved optical semitransparency and stability

PbS colloidal quantum dots, with their tunable bandgap and broad light absorption, are key materials for absorbing NIR light in tandem solar cells. When paired with perovskite as front solar cells, known for their impressive efficiencies in the visible spectrum, such tandem configuration offers the potential to absorb both visible and infrared light, maximizing overall device efficiency.

In this study, we successfully developed a 4T tandem solar cell that integrates methylammonium lead iodide ($MAPbI_3$) perovskite solar cell as the front sub-cell and PbS colloidal quantum dot (CQD) solar cell as the back sub-cell (**Figure 28a**). This combination of materials is highly advantageous because it provides efficient and spectrally matched absorption of both visible and near-infrared light. The perovskite solar cell absorbs light up to around 800 nm, while the PbS CQD solar cell extends the absorption range up to 1100 nm, as illustrated in **Figure 28b**. Our main objective was to enhance the transmission of lower-energy photons through the perovskite top-cell, enabling these photons to be absorbed by the PbS CQD back-cell. This was achieved through the modification of the interlayer between the two sub-cells. Specifically, we incorporated a semi-transparent thin gold electrode (Au) on top of the $MAPbI_3$ perovskite solar cell and further enhanced this structure by adding a molybdenum(VI) oxide (MoO_3) or surlyn ionomer resin interlayer. Both the thin Au electrode and metal oxide layers had been used in previous work to improve solar cell transmittance.

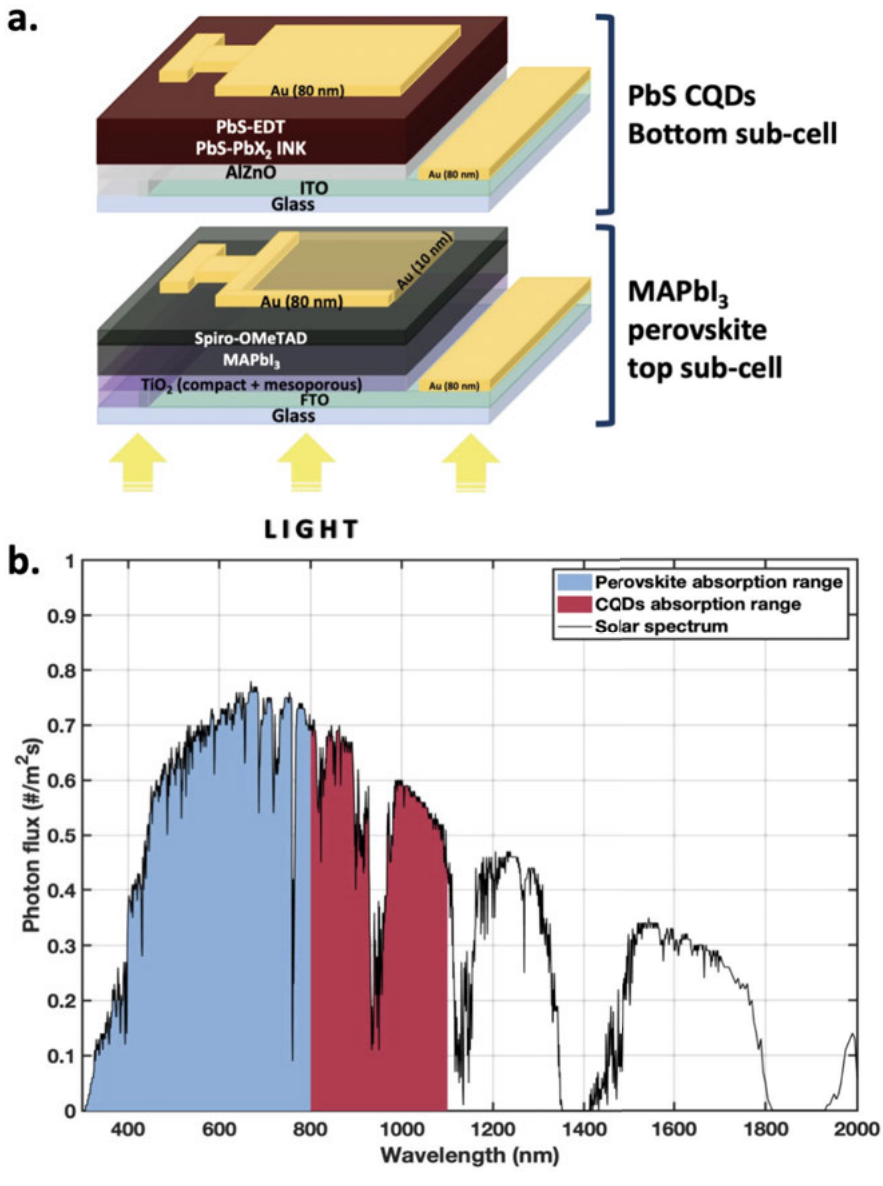

Figure 28. Perovskite quantum dot tandem design: **(a)** schematic design of a 4-termianl (4T) tandem device, where the front sub-cell is $MAPbI_3$ perovskite and the back sub-cell is PbS colloidal quantum dots (PbS CQDs). **(b)** Solar spectrum with highlighted light absorption regions for both perovskite and CQD solar cells in this work. Figure adapted from **Paper II**.

Interlayer Modification for Enhanced Light Transmission

In order to improve the transmission of NIR light through the perovskite front-cell to the PbS CQD back-cell, we first focused on optimizing the thickness of the gold electrode. Typically, perovskite solar cells incorporate a thick 80 nm gold electrode, which greatly reduces device transmittance in the infrared region. In this work, we systematically tested 10 nm, 15 nm, and 80 nm gold layers and observed that the 10 nm Au layer provided the highest infrared transmittance, as shown in **Figure 29a**.

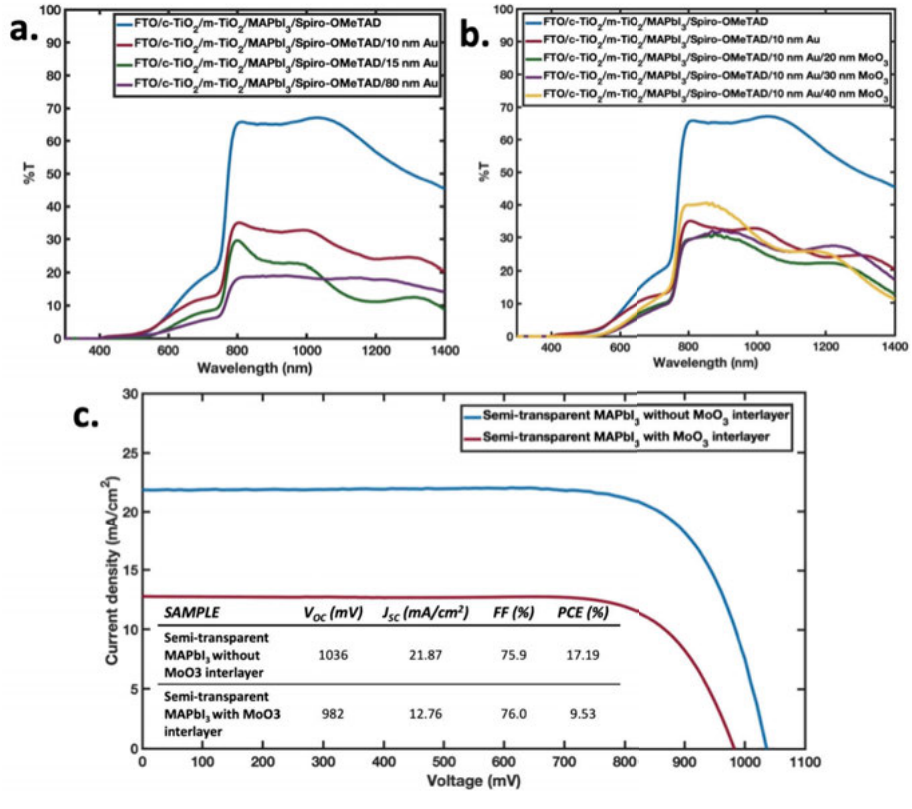

Figure 29. (a) Transmittance spectrum of the perovskite solar cell with the following structure: FTO glass/compact TiO_2/mesoporous TiO_2/$MAPbI_3$ perovskite/Spiro-OMeTAD with different thicknesses of the Au electrode (10, 15 and 80 nm). **(b)** Transmittance spectrum of the perovskite solar cell with the following structure: FTO glass/compact TiO_2/mesoporous TiO_2/$MAPbI_3$ perovskite/Spiro-OMeTAD/10nm Au with different thicknesses of MoO_3 layer on top (20, 30, 40 nm). **(c)** Current-voltage measurements of the semi-transparent $MAPbI_3$ solar cell with 10 nm Au electrode (blue line) and with 10 nm Au electrode followed by 20 nm MoO_3 interlayer (red line) The table includes the photovoltaic parameters extracted from the measuremnts. Figure adapted from **Paper II**.

We further enhanced the interlayer by testing various thicknesses of MoO_3, a transparent metal oxide known for improving solar cell transmittance. We tested 20 nm, 30 nm, and 40 nm MoO_3 layers on top of the 10 nm Au electrode in perovskite sub-cell. The 40 nm MoO_3 layer demonstrated the best performance, with approximately 40% transmittance in the NIR region, as depicted in **Figure 29b**. Despite the optical improvements, the incorporation of MoO_3 caused significant decrease in the current-voltage performance, likely due to interactions between MoO_3 and the very sensitive Spiro-OMeTAD layer, which affected device stability, as shown in **Figure 29c**.

Introduction of Surlyn Encapsulation for Stability and Light Management

In order to optimize light management and improve the stability of the tandem device, we incorporated surlyn encapsulation as an alternative interlayer. Surlyn is a transparent ethylene and methacrylic acid copolymer, which has excellent chemical resistance, flexibility, and optical transparency, especially when used in thin layers. We used surlyn with a thickness of 25 μm, which effectively eliminated the air gap between the sub-cells, reducing reflections and thereby improving light coupling between the perovskite and PbS CQD cells. By minimizing reflections at the interfaces, the surlyn encapsulation enhanced the light transmission to the CQD bottom-cell. This interlayer also contributed to improving the chemical stability of the $MAPbI_3$ perovskite sub-cell by protecting it from environmental degradation.

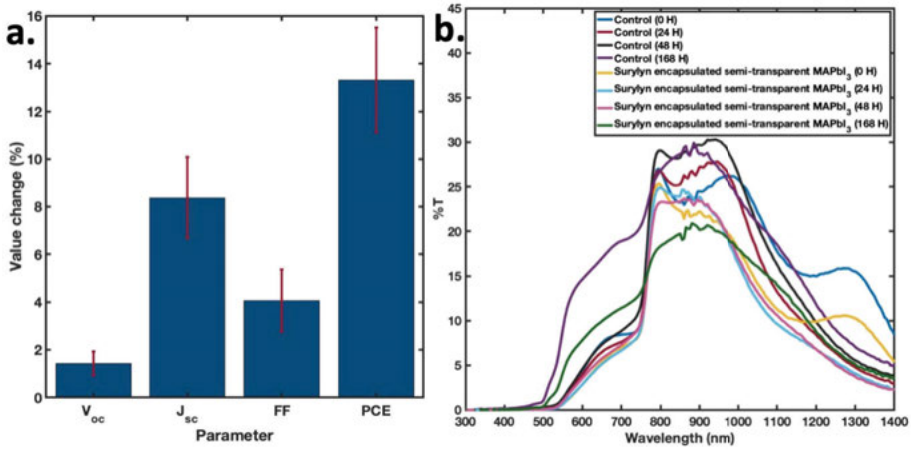

Figure 30. (a) Percentage value of an average increase in photovoltaic parameters after incorporating surlyn into the tandem solar cell structure. For this statistical measurement, 12 samples of PbS CQD solar cells with λ_{max} values equal to both 901 and 935 nm, respectively, were used. **(b)** Optical stability measurements for tandem solar cells after incorporation of surlyn into the device structure. The control sample is the non-encapsulated semi-transparent $MAPbI_3$ solar cell with the following structure: FTO/c-TiO_2/m-TiO_2/$MAPbI_3$ perovskite/Spiro-OMeTAD/10 nm Au. Surlyn-encapsulated $MAPbI_3$ samples have the following composition: FTO/c-TiO_2/m-TiO2/ $MAPbI_3$ perovskite/Spiro-OMeTAD/10 nm Au/surlyn/ITO/AlZnO. Figure adapted from **Paper II**.

To analyze the impact of the surlyn interlayer, we compared the photovoltaic performance of tandem devices before and after surlyn was incorporated. On average, tandem devices with surlyn demonstrated a 13% increase in PCE and an 8% increase in J_{sc} compared to devices without surlyn (**Figure 30a**). These results confirmed that surlyn significantly improved light transmission to the CQD bottom-cell by reducing reflection losses at the interfaces. The surlyn interlayer thus played a crucial role in enhancing both the optical and electrical performance of the tandem device.

In addition to its positive effect on performance, the surlyn interlayer also contributed to the stability of the tandem device. We compared the optical stability of the semi-transparent $MAPbI_3$ devices with and without surlyn encapsulation over a period of 7 days under AM 1.5 illumination in ambient air. As shown in **Figure 30b**, non-encapsulated devices exhibited approximately 10% higher transmittance in the visible region than encapsulated devices during the testing period. Also, the degradation of the $MAPbI_3$ perovskite layer was significantly reduced in the surlyn-encapsulated devices. This indicates that surlyn not only improves light transmission but also acts as a protective barrier, preserving the optical and chemical integrity of the perovskite layer.

Power Conversion Efficiency (PCE) Improvements

To evaluate the overall performance of the 4T tandem device, we fabricated a semi-transparent $MAPbI_3$ perovskite solar cell with a 10 nm Au electrode and stacked it on top of a PbS CQD solar cell. We then measured the current-voltage characteristics and power conversion efficiency of the tandem device. The best-performing J-V characteristics for the perovskite and PbS CQD solar cells are displayed in **Figure 31a**. When the perovskite front-cell was stacked on top of the PbS CQD back-cell, a decrease in the PCE of the bottom PbS CQD cell was observed, which was expected due to the reduced light intensity reaching the CQD cell. Despite this expected reduction, the tandem structure still exhibited significant performance enhancement compared to individual sub-cells. The IPCE, shown in **Figure 31b**, revealed that the perovskite cell converts light up to 800 nm, while the PbS CQD cell absorbs light up to 1100 nm. The combination of the semi-transparent $MAPbI_3$ front-cell and the PbS CQD back-cell using the surlyn interlayer achieved an overall efficiency of 18.9% (see **Table 2**), representing a clear improvement over the single-junction sub-cells. This performance enhancement can be attributed to more efficient light utilization in the tandem configuration, as well as reduced carrier thermalization losses.

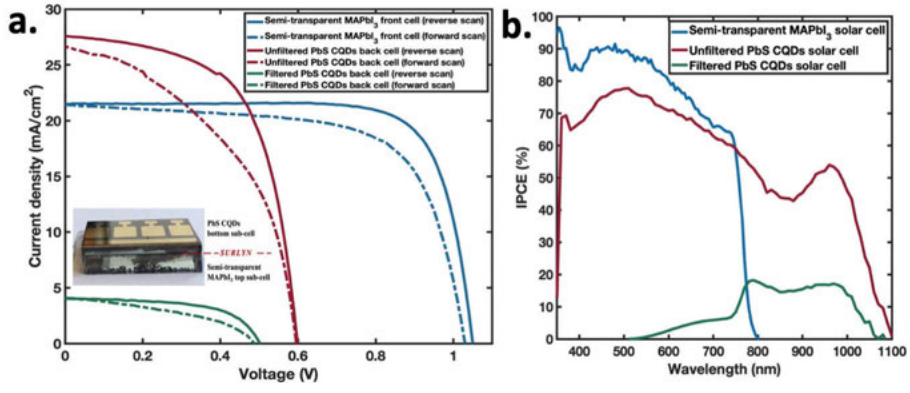

Figure 31. (a) J–V characteristics of unfiltered (red line) and filtered (green line) PbS CQD devices and the semi-transparent $MAPbI_3$ device (blue line), under AM 1.5G illumination. The semi-transparent $MAPbI_3$ SC structure: FTO glass/compact TiO_2/mesoporous-TiO_2/$MAPbI_3$ perovskite/Spiro-OMeTAD/10 nm Au/surlyn (25 μm). The PbS CQD SC architecture: ITO glass/AlZnO layer/PbS-PbX_2/PbS-EDT/80 nm Au. PbS CQDs of λ_{max} = 935 nm were used for these measurements. The filtered PbS CQD cell means that during the measurement, the semi-transparent $MAPbI_3$ solar cell was placed above the CQD cell – see the included profile picture of the perovskite-CQD tandem solar cell (2.4 × 1.4 cm in size). (b) IPCE spectra of the PbS CQD cell (red line), the $MAPbI_3$ perovskite cell with a 10 nm semi-transparent Au electrode (blue line) and the filtered PbS CQD cell with a semi-transparent $MAPbI_3$ cell as the filter (green line). Figure adapted from **Paper II**.

Table 2. Summary of the photovoltaic performance of the champion 4T perovskite-CQD tandem solar cell, together with the performance of individual components.

DEVICE	V_{oc} (V)	J_{sc} (mA/cm^2)	FF (%)	PCE (%)
Semi-transparent $MAPbI_3$ front cell (reverse scan)	1.050	-21.50	76.9	17.37
Semi-transparent $MAPbI_3$ front cell (forward scan)	1.030	-21.45	67.3	14.88
Unfiltered PbS CQDs back cell (reverse scan)	0.598	-27.58	61.0	10.06
Unfiltered PbS CQDs back cell (forward scan)	0.595	-26.67	46.6	7.40
Filtered PbS CQDs back cell (reverse scan)	0.517	-4.83	61.1	1.53
Filtered PbS CQDs back cell (forward scan)	0.500	-4.82	43.4	1.05
4-terminal tandem solar cell (reverse scan)	-	-	-	18.90
4-terminal tandem solar cell (forward scan)	-	-	-	15.93

Conclusion

In conclusion, our study demonstrated the successful development of a 4T tandem solar cell that integrates PbS CQD solar cells with $MAPbI_3$ perovskite solar cells. By optimizing the interlayer with a 10 nm Au electrode and surlyn encapsulation, we achieved a significant improvement in overall performance, with a PCE of 18.9%. The surlyn interlayer not only enhanced light transmission to the CQD bottom-cell but also improved the stability of the perovskite top-cell, making this tandem device a promising candidate for high-efficiency photovoltaic applications.

This work underscores the potential of hybrid tandem architectures combining quantum dot and perovskite materials to harness their complementary properties, offering pathways for further optimization in tandem device design, stability, and performance. The insights gained here contribute to the ongoing efforts to push the efficiency limits of photovoltaic technologies and open avenues for more sustainable, scalable, and high-performance solar cells in the future.

Paper III: Combining Quantum Dot and Perovskite Photovoltaic Cells for Efficient Photon to Electricity Conversion in Energy Storage Devices

In this work, we investigated the potential of combining a quantum dot (QD)-based photovoltaic cell with a perovskite-based photovoltaic cell from **Paper II** to efficiently convert a broad range of wavelengths emitted from energy storage materials into electricity. By utilizing a tandem configuration, we aimed to enhance the conversion efficiency of light emitted at high temperatures, specifically from materials heated to 1000°C and 2000°C, which exhibit broad black-body radiation spectra. Our approach focused on optimizing the photovoltaic response and electrical power output, comparing the performance of single QD cells against the tandem QD-perovskite configuration.

The black-body radiation spectra for materials at these two temperatures are depicted in **Figure 32**, demonstrating that the spectrum at 1000°C primarily consists of infrared radiation, with minimal visible light, while the spectrum at 2000°C extends further into the visible region. This broad emission necessitates the effective absorption of infrared light by the QD cells to achieve high conversion efficiency, particularly in thermophotovoltaic (TPV) applications, which have traditionally faced challenges in efficiency due to significant heat losses in fuel combustion systems.

Evaluation of Photovoltaic Response and Power Output

To evaluate the conversion of photons to electricity, we utilized light spectra that mimic black-body radiation. The spectral distributions for both 1000°C and 2000°C, highlights the predominance of infrared emissions at lower temperatures (**Figure 32**). Our results indicate that a QD photovoltaic cell, specifically based on PbS, can effectively convert infrared light, thereby making it a suitable candidate for application in a photon glow battery designed to utilize heat energy.

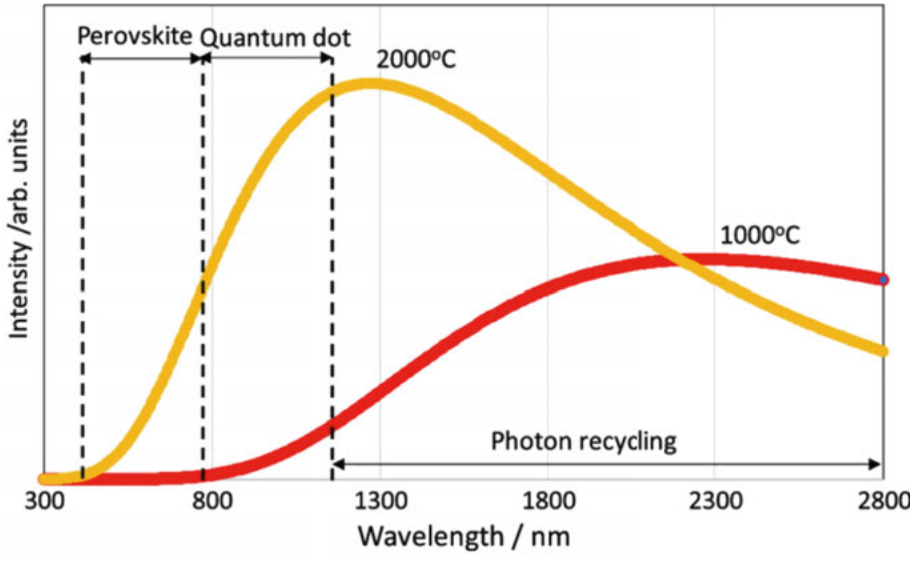

Figure 32. Schematic of spectra for the light emitted from hot energy storage material and which parts of these spectra that can be converted in photovoltaic devices or recycled back to the energy storage material by a reflector. The black-body light emission spectra are shown for 1000 and 2000 °C. In the figure are also indicated the spectral regions absorbed by the perovskite photovoltaic cell and QD photovoltaic cell in this work. Figure adapted from **Paper III**.

In this study, the PbS QD photovoltaic cell was shown to convert light up to approximately 1100 nm (see **Figure 33a**), thereby facilitating the conversion of a significant portion of infrared radiation into electricity. The architecture of the QD photovoltaic cell is illustrated in the inset of **Figure 33b**, alongside an energy level diagram of the various layers involved (see **Figure 33c**). Current-voltage measurements for the QD photovoltaic cell under simulated black-body radiation at 1000°C and 2000°C revealed light intensities of 9.0 mW/cm² and 11.1 mW/cm², respectively, demonstrating the device's capacity to harness energy from the emitted spectra (**Figure 33b**).

The power conversion efficiency was calculated based on the illumination power and the electrical output from the photovoltaic cell. However, it is important to note that the light not absorbed by the QD cell is reflected back to

the energy storage material, which is an essential consideration in our analysis. The efficiency results indicate approximately 12.5% PCE for simulated light from a 2000°C energy storage material, and around 9.6% PCE for 1000°C light. These numbers underscore the advantages of using QD photovoltaic cells for infrared light conversion.

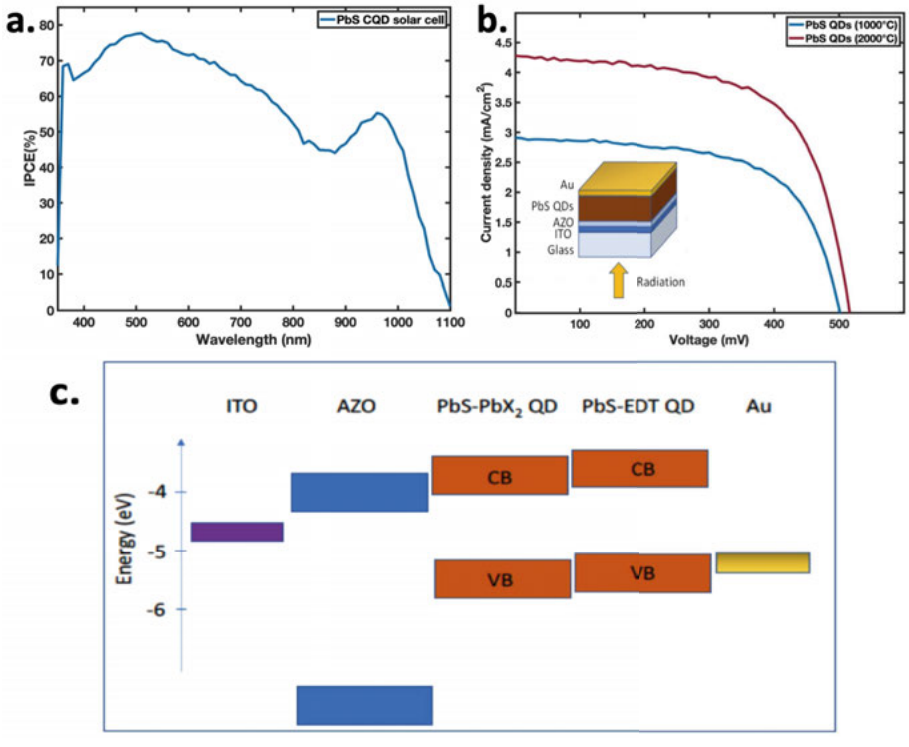

Figure 33. (a) IPCE spectra of PbS quantum dot photovoltaic cell. Integrated current for solar light (AM 1.5G 1000 W/m^2) was calculated to 26.75 mA/cm^2. **(b)** Current–voltage measurements of a PbS QD-based photovoltaic cell under illumination with simulated black-body radiation for 1000 and 2000 °C hot energy storage materials with light intensity 9.0 and 11.1 mWcm^{-2}, respectively. The inset shows the architecture of the photovoltaic cell. **(c)** Schematic approximative energy level diagram for the layers in the quantum dot photovoltaic cell. Indium tin oxide (ITO), Aluminium doped zinc oxide (AZO), PbS quantum dots with PbI_2 and $PbBr_2$ ligands, PbS quantum dots with EDT ligands, and a gold (Au) contact. Figure adapted from **Paper III** and the values are obtained from ref.4 and ref.5 from **Paper III**.

Comparison of QD and Perovskite Solar Cells

In addition to evaluating the performance of the QD photovoltaic cells, we also assessed the contribution of $MAPbI_3$ perovskite solar cells in our tandem configuration. The perovskite solar cell is effective in absorbing visible light, converting photons up to approximately 770 nm into electricity. **Figure 34a** presents the J-V characteristics of the semi-transparent perovskite

photovoltaic cell when subjected to simulated black-body radiation at both 1000°C and 2000°C. The results demonstrate a PCE of approximately 23% for the higher temperature spectrum and around 8.2% for the lower temperature spectrum, reflecting the enhanced photocurrent generation at elevated temperatures.

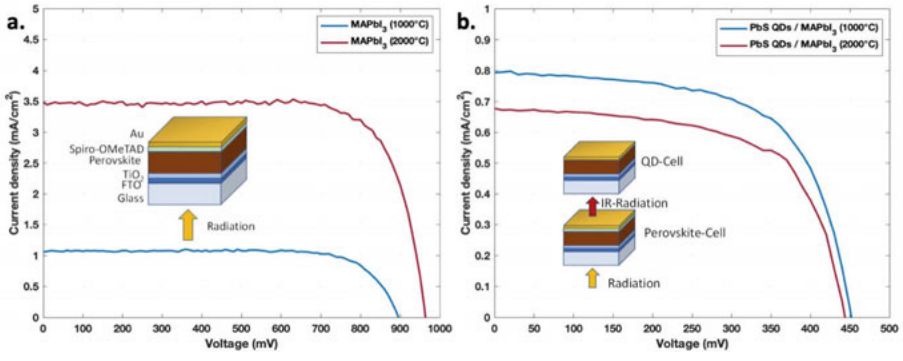

Figure 34. (a) Current–voltage measurements of a semitransparent $MAPbI_3$ perovskite-based photovoltaic cell under illumination with simulated black-body radiation for 1000 and 2000 °C hot energy storage materials with light intensity 9.0 and 11.1 $mWcm^{-2}$, respectively. The inset shows the architecture of the photovoltaic cell. **(b)** Current-voltage measurements of a PbS QD-based solar cell behind a semitransparent $MAPbI_3$ perovskite-based photovoltaic cell, under light illumination with simulated black-body radiation for 1000 and 2000 °C hot energy storage materials with light intensity 9.0 and 11.1 $mWcm^{-2}$, respectively. The inset shows how the radiation first reaches the semitransparent perovskite photovoltaic cell, and part of the infrared light is transmitted through the perovskite photovoltaic cell and reaches the PbS QD photovoltaic cell. Figure adapted from **Paper III**.

By placing the perovskite photovoltaic cell in front of the QD cell, we effectively absorb high-energy photons first, which allows the lower-energy photons to be converted by the QD photovoltaic cell. This arrangement is illustrated in **Figure 34b**, which shows the current-voltage measurements of the QD photovoltaic cell when positioned behind the perovskite photovoltaic cell under simulated black-body radiation conditions. Notably, the PCE for the PbS QD photovoltaic cell displayed a higher efficiency for the 1000°C spectrum compared to the 2000°C spectrum. This observation can be attributed to the increased light intensity in the infrared region reaching the PbS QD photovoltaic cell through the perovskite cell.

Calculating the overall efficiency of the tandem structure, we determined an approximate PCE of 11% for light emitted from a 1000°C energy storage material and about 25% for the 2000°C source. The combination of QD and perovskite photovoltaic cells led to improved conversion efficiencies compared to using either cell type alone. These results are competitive with existing heat-to-electricity conversion technologies, including TPV devices and solid-state thermoelectric.

Future Directions and Potential Improvements

Despite the promising results, we recognize that further optimization is necessary to enhance the performance of our photovoltaic devices. The QD photovoltaic cell can be optimized for better infrared light absorption by increasing the size of the QDs, which would allow for greater photocurrent generation, particularly from lower temperature energy storage radiation. The data presented in **Figure 35c,d** illustrates the performance of QD photovoltaic cells with larger QDs, which extend their absorption range up to 1200 nm (see **Figure 35a,b**). These larger QDs yield a higher photocurrent for the black-body radiation spectrum at 1000°C, compared to the smaller QDs used in our current configuration.

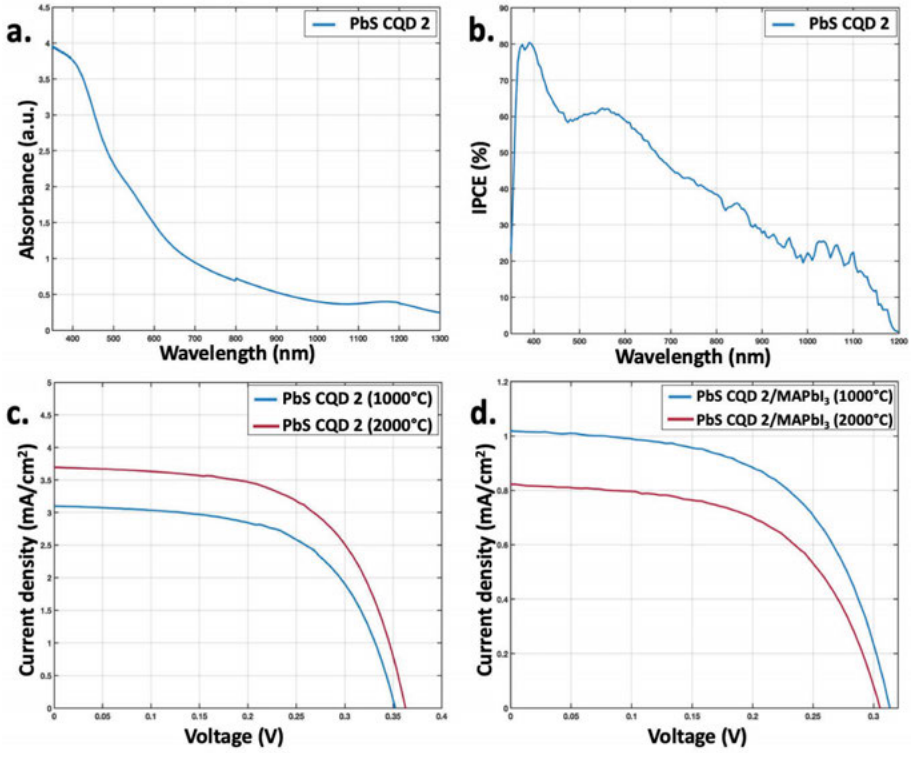

Figure 35. (a) UV-Vis-NIR absorbance spectrum of large PbS CQDs, with absorption maximum around 1170 nm. **(b)** IPCE spectra of PbS quantum dot (large QDs) photovoltaic cell. **(c)** Current-voltage measurements of a PbS quantum dot (large QDs) based photovoltaic cell under illumination with simulated black-body radiation for 1000°C and 2000°C hot energy storage materials with light intensity 9.0 and 11.1 mW/cm^2, respectively. **(d)** Current-voltage measurements of a PbS QD (large QDs) based solar cell behind a semitransparent $MAPbI_3$ perovskite based photovoltaic cell, under light illumination with simulated black-body radiation for 1000°C and 2000°C hot energy storage materials with light intensity 9.0 and 11.1 mW/cm^2, respectively. Figure adapted from **Paper III**.

Moreover, we acknowledge that the transmission of infrared light through the perovskite cell is not perfect. Future work may involve optimizing the semi-transparent gold electrode or exploring alternative transparent materials, such as indium tin oxide (ITO), to enhance infrared light transmittance. Implementing these improvements could lead to higher efficiencies and increased electrical power output in subsequent iterations of this device.

In the context of a complete photon glow battery, it is also essential to consider the overall system efficiency and thermal losses. Efficient insulation materials are necessary to minimize heat loss from the energy storage material, thereby improving the overall heat-to-electricity conversion efficiency. While existing technologies such as batteries exhibit lower losses, our tandem photovoltaic system presents a competitive alternative for large-scale energy storage with potential for very low cost due to the less complexity in design.

Conclusion

In summary, this work demonstrates the successful integration of QD and perovskite photovoltaic cells into a tandem configuration designed for efficient conversion of light emitted from energy storage materials. By combining the complementary absorption characteristics of the QD and perovskite cells, we achieved competitive power conversion efficiencies under both simulated black-body radiation and standard solar conditions. Our findings pave the way for further advancements in tandem photovoltaic technology, with a focus on optimizing performance and enhancing the energy efficiency of future photon glow battery systems. This research not only contributes to the development of innovative tandem solar cells, but also highlights the broader potential of hybrid photovoltaic systems in addressing the challenges of energy conversion and storage. By leveraging the unique properties of quantum dots and perovskites, this work underscores the promise of multi-junction architectures to push the boundaries of energy efficiency and sustainability, offering pathways for more versatile, scalable, and cost-effective technologies in the future.

Project II: Optimizing Charge Dynamics Through Charge Extraction Materials in PbS Colloidal Quantum Dot Solar Cells

The integration of PbS colloidal quantum dot solar cells into tandem configurations, as explored in **Project I**, demonstrated promising advancements in enhancing solar energy conversion efficiencies. By leveraging the distinct spectral absorption properties of PbS CQD and other photovoltaic technologies, this project successfully established a pathway for improved light harvesting across a broader spectrum of sunlight. However, despite the overall success, a recurring theme emerged: the PbS CQD sub-cell consistently exhibited performance limitations.

Project II, including **Paper IV** and **Paper V,** builds upon the insights gained from **Project I** and tries to address the deficiencies of the PbS CQD devices. It aimes to enhance the performance and stability of PbS colloidal quantum dot solar cells by focusing on ligand engineering and its effects on charge recombination, extraction, and overall device efficiency, ultimately contributing to the advancement of CQD-based tandem solar technologies. **Paper IV** investigated the role of thiol ligands in reducing charge recombination losses and improving surface passivation for better efficiency and stability of PbS CQDSCs. Whilst **Paper V** examined interfacial charge transfer dynamics between PbS QDs and 2H-MoS_2 charge transport material, emphasizing the importance of ligand chemistry in enhancing charge extraction and overall PbS CQDs device performance.

Paper IV: Regulating Thiol Ligands of p-Type Colloidal Quantum Dots for Efficient Infrared Solar Cells

The performance of colloidal quantum dot solar cells (CQDSCs) is highly influenced by the surface chemistry of the CQDs, specifically the ligands used for surface passivation. Thiol ligands play a critical role in determining the optoelectronic properties of p-type CQD solid films. However, the widely used 1,2-ethanedithiol (EDT) ligand, while effective in forming p-type CQDs, has been shown to negatively impact the underlying n-type CQD layers in p-n heterojunction devices, leading to charge recombination losses and lower efficiency.

In this study, we systematically investigated the potential of 2-propanethiol (PT), and 4-aminobenzenethiol (ABT) ligands as alternatives to EDT for passivating p-type CQDs in infrared CQDSCs. By employing a combination of density functional theory (DFT) calculations and experimental studies, we aimed to optimize the interaction between thiol ligands and CQDs, enhance surface passivation, and ultimately improve the efficiency of CQDSCs. Our focus was on understanding the limitations associated with EDT ligands and exploring how ABT ligands, in particular, could enhance device performance by reducing recombination and improving charge extraction.

Theoretical Analysis of CQD-Ligand Interactions

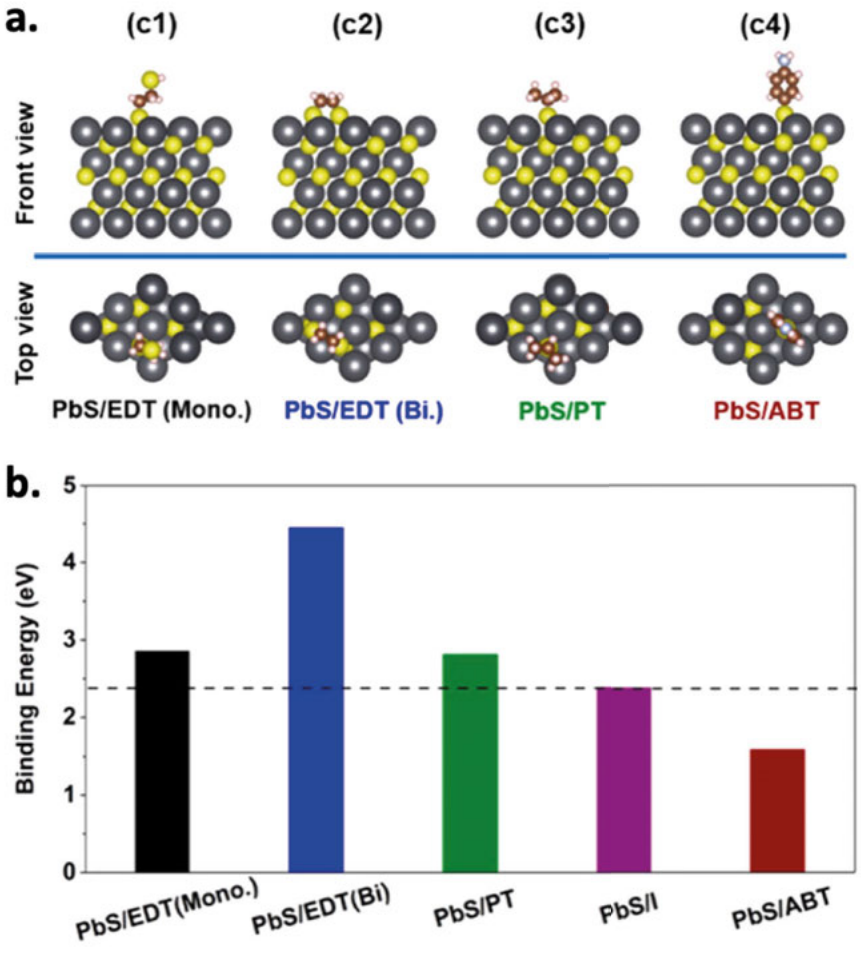

Figure 36. (a) Front views (up) and top views (down) of the calculated structures of the (c1) CQD/EDT (Mono.), (c2) CQD/EDT (Bi.), (c3) CQD/PT, and (c4) CQD/ABT systems. **(b)** Binding energies of the ligands on the CQD surface. The binding energy of I^- on the CQD surface was also calculated for comparison, as marked with the dotted line. Figure adapted from **Paper IV**.

To gain insight into the atomic interactions between CQDs and thiol ligands (EDT, PT, and ABT), we performed DFT calculations, using the Vienna *Ab initio* Simulation Package. The {111} facet of PbS CQDs was selected for the theoretical models, as this surface is prone to oxidation if not properly passivated. We simulated the bonding configurations of the CQDs with EDT, PT, and ABT ligands, and the optimized structures are presented in **Figure 36a**. Results showed that the S atoms in the thiol ligands are coordinated by three

Pb atoms, and the calculated Pb−S_{ligand} bond lengths were similar across the different ligand systems and equal around 3.0 Å (**Table 3**). For comparison, the bond length of Pb−I_{ligand} in n-type CQDs is 3.428 Å, suggesting that the thiol ligands form stronger bonds with the CQD surface than halide ligands. The binding energies for the different ligands are presented in **Figure 36b**, showing that the binding energy of Pb−S in the EDT system is higher than that of Pb−I. This suggests that EDT ligands are likely to displace I^- ions on the n-type CQD surface, leading to recombination losses at the p-n junction. In contrast, ABT ligands exhibit a lower binding energy with PbS, making them less likely to replace I^- ions and therefore more suitable for use in p-type CQD films.

Table 3. The calculated bond length of Pb-S_{ligand} for different thiol-ligand systems, the bond length of Pb- I_{ligand} was also included for comparison.

Name	Pb-X (ave.)/ Å
PbS/EDT (Mono.)	3.036
PbS/EDT (Bi.)	3.019
PbS/PT	3.098
PbS/ABT	3.031
PbS/I	3.428

Charge Transfer and Electronic Properties

To further understand the electronic interactions between CQDs and thiol ligands, we analyzed the charge density differences and Bader charge distributions. As illustrated in **Figure 37a**, significant charge accumulation was observed around the sulfur atoms of the thiol ligands, indicating strong ionic bonding between the CQD and ligand. The Bader charge analysis (**Figure 37b**) shows that the EDT ligands transfer more electrons to the CQD surface than PT and ABT ligands. However, excessive charge transfer, as seen with EDT, can lead to increased recombination losses. ABT ligands, on the other hand, provide more balanced charge transfer, which is favorable for reducing recombination and enhancing charge extraction.

Further, the density of states (DOS) calculations showed that the electronic coupling between CQDs and ABT ligands was stronger than that with PT ligands but slightly weaker than with EDT ligands. However, the hybridization of the ABT states occurred at slightly deeper energy levels compared to EDT, potentially improving light absorption and reducing surface trap states, which could benefit charge transport in CQDSCs.

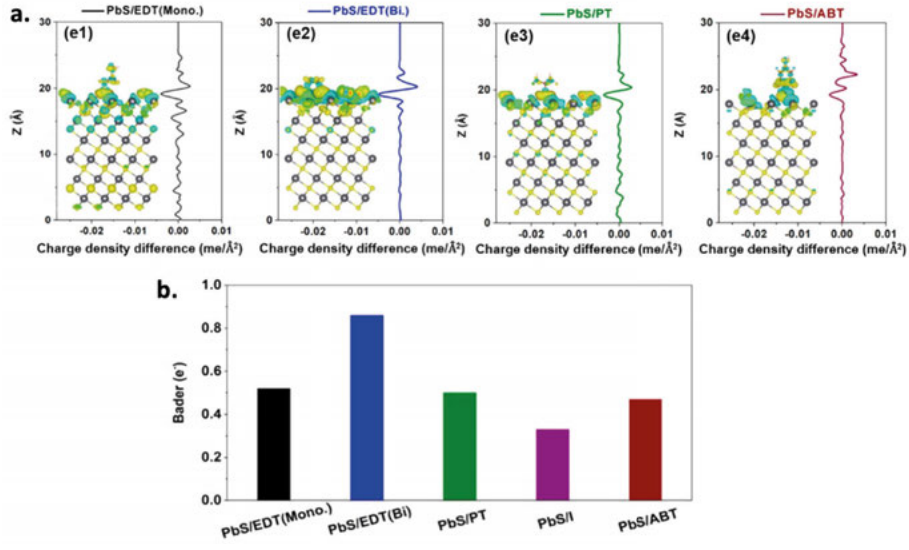

Figure 37. (a) Charge density differences and Z-axis line profiles of the charge density differences of the (e1) CQD/EDT (Mono.), (e2) CQD/EDT (Bi.), (e3) CQD/PT, and (e4) CQD/ABT systems. **(b)** Bader charges of the interfaces between the CQD and surface ligand. Figure adapted from **Paper IV**.

Optoelectronic Properties of Thiol-Passivated CQD Films

The optical properties of CQD films passivated with EDT, PT, and ABT ligands were assessed using UV-Vis absorption spectroscopy. As shown in **Figure 38a**, CQD-EDT and CQD-ABT films exhibited a slight red-shift in their first exciton absorption peaks compared to pristine CQD-OA films, indicating successful ligand exchange. The blue-shift in CQD-PT films, attributed to surface oxidation, suggests incomplete passivation.

Further analysis with Fourier Transform Infrared Spectroscopy (FTIR) spectroscopy (**Figure 38b**) confirmed efficient ligand exchange for CQD-EDT and CQD-ABT films, as evidenced by the near disappearance of oleyl group peaks and a significant reduction in the carboxyl group's asymmetric stretching ($\nu as(COO^-)$). In contrast, CQD-PT films showed only a slight reduction in oleyl group signals, indicating less effective ligand exchange. Also, the distinct FTIR signals for CQD-ABT, including a strong absorption band at ~3345 cm^{-1} (symmetric stretching of NH_2) and characteristic peaks of the aromatic ring (1600–1400 cm^{-1}), confirmed ABT's robust attachment to the CQD surface, suggesting it is highly effective for passivation and OA replacement.

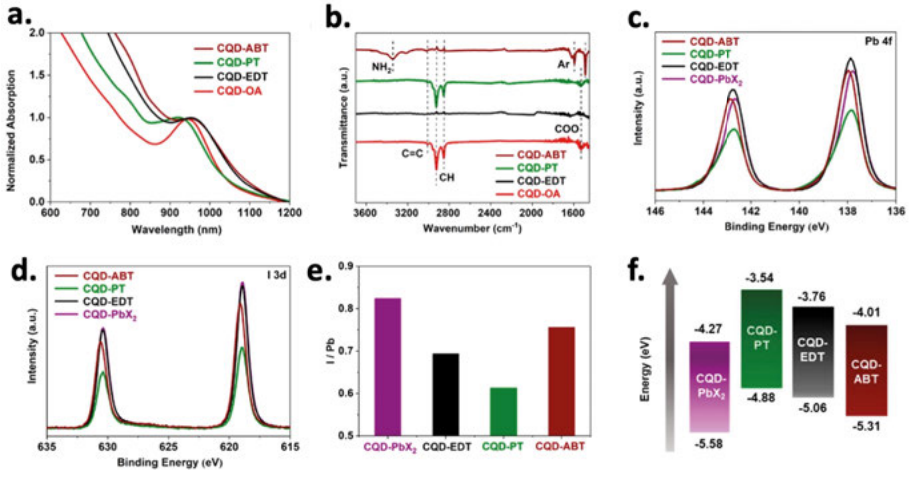

Figure 38. CQD solid films. **(a)** Light absorption spectra and **(b)** FTIR spectra of the CQD solid films with different thiol ligands passivating the quantum dot surface. The CQD-OA is also included for comparison. Core-level spectra of **(c)** Pb 4f and **(d)** I 3d of CQD-PbX_2 and the CQD-PbX_2 solid film treated with different thiol ligands. **(e)** Mole ratio of I/Pb in the CQD-PbX_2 solid and the CQD-PbX_2 solid film treated with different thiol ligands. **(f)** Schematic diagram of the energy levels of the CQD solid films with different ligands passivating the dot surface. Figure adapted from the **Paper IV**.

X-ray photoelectron spectroscopy (XPS) revealed key insights into the elemental composition and surface passivation of thiol treated CQD samples (**Figure 38c,d**). The analysis of I/Pb ratios (**Figure 38e)** showed that soaking CQD-PbX_2 solid films in thiol ligand solutions led to a decrease in the I/Pb ratio across all samples, suggesting that the thiol ligands partially replaced I^- on the CQD surface. Among the samples, CQD-ABT exhibited the highest I/Pb ratio, implying that ABT ligands caused the least disturbance to the CQD-PbX_2 structure, aligning with theoretical predictions.

We also studied the energy level alignment of the thiol-passivated CQD films using ultraviolet photoemission spectroscopy (UPS) in combination with the optical bandgap calculations from the light absorption spectra. As shown in **Figure 38f**, the energy levels of the CQD-PbX_2 films were compared to those of CQD-EDT, CQD-PT, and CQD-ABT films. The valence band maximum (VBM) of the CQD-ABT film was found to be lower than that of the CQD-EDT film, which reduces the band offset between the p-type and n-type CQD layers. This reduction in band offset is expected to diminish interfacial recombination, thereby enhancing charge extraction and improving device performance.

The crystal structures of the CQD films were characterized by X-ray diffraction (XRD), and the results, presented in **Figure 39a**, reveal no significant differences in the crystal structure after ligand exchange. This indicates that the thiol ligands do not affect the overall crystallinity of the CQD films. Additionally, atomic force microscopy (AFM) measurements (**Figure 39b**)

analysis revealed uniform films with root-mean-square (RMS) roughness values of ~4.36 nm for CQD-EDT and ~4.75 nm for CQD-ABT films, confirming smooth surface morphology essential for high-efficiency solar cells. The smoother surface roughness could contribute to improved surface passivation and reduced recombination at the CQD surface.

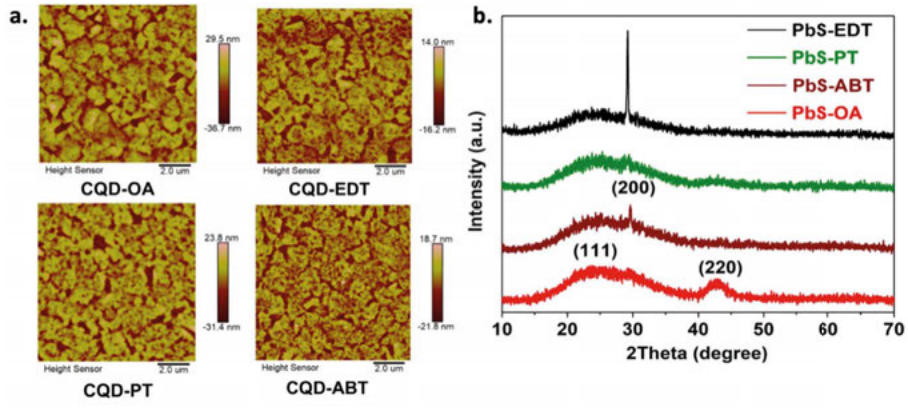

Figure 39. (a) AFM images of the CQD-OA solid film, CQD-EDT solid film, CQD-PT solid film and CQD-ABT solid film. **(b)** XRD patterns of the CQD solid films with different ligands passivating CQD surface. After the ligand exchange, the crystal facets and crystal orientations of CQDs may be arranged differently and may show slight changes in XRD patterns. Meanwhile, the distance between dot-to-dot also changed due to the various degrees of ligand exchange, therefore affecting the crystal orientation. Figure adapted from **Paper IV**.

J-V Characteristics and Power Conversion Efficiency

To evaluate the impact of the different thiol ligands on CQD solar cell performance, we fabricated CQDSCs with the structure glass/ITO/AZO/CQD-PbX_2/CQD-thiol/Au (**Figure 40a**). The current density-voltage characteristics of the devices under AM1.5G illumination are shown in **Figure 40b**, and the photovoltaic parameters are summarized in **Table 4**.

Table 4. Photovoltaic Parameters of the CQDSCs with Different p-Type CQD Solid Films as Hole Conductors. The data in parentheses are statistics from 20 devices fabricated from different branches.

Device	V_{oc} (V)	J_{sc} (mA/cm^2)	FF	PCE (%)
CQD-EDT	0.63 (0.61 ± 0.02)	28.1 (27.2 ± 0.9)	0.65 (0.63 ± 0.02)	11.5 (10.9 ± 0.6)
CQD-PT	0.59 (0.57 ± 0.02)	28.7 (27.4 ± 1.3)	0.61 (0.57 ± 0.04)	10.3 (9.5 ± 0.8)
CQD-ABT	0.64 (0.62 ± 0.02)	28.8 (27.8 ± 0.9)	0.66 (0.64 ± 0.02)	12.2 (11.6 ± 0.5)

The device with the CQD-EDT film as the hole transport layer (HTL) achieved a PCE of 11.5%, which is consistent with previously reported values. However, the device with the CQD-ABT film exhibited a significantly higher PCE of 12.2%. This improvement was primarily driven by an increase in the open-circuit voltage (V_{oc}) and fill factor (FF), suggesting better charge extraction and reduced recombination. The CQD-PT-based device, by contrast, showed a lower PCE of 10.3%, likely due to incomplete ligand exchange with PT, as indicated by the FTIR spectra.

These results demonstrate that ABT ligands offer superior surface passivation and are more effective in enhancing device efficiency compared to EDT and PT.

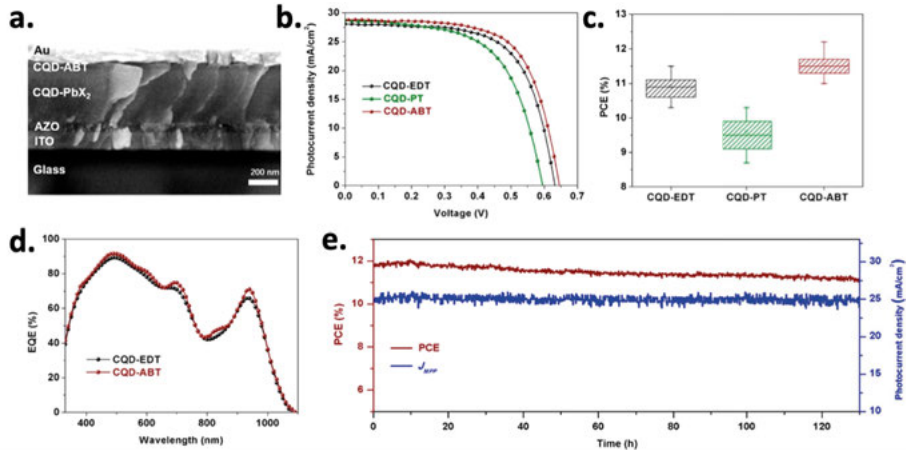

Figure 40. (a) Cross-sectional SEM image of the CQDSC with a p-type CQD-ABT solid film as a hole conductor. **(b)** J–V curves and **(c)** PCE statistics of the CQDSCs with different p-type CQD solid films as hole conductors. **(d)** EQE spectra of the EDT- and ABT-based CQDSCs. **(e)** Steady-state output of PCE and J_{sc} of the ABT-based CQDSCs under continuous illumination with an intensity of 100 mW/cm^2. A white LED was applied as a light source, and the light intensity was calibrated before the measurement. Figure adapted from **Paper IV**.

Charge Carrier Dynamics and Recombination Losses

To evaluate the effect of surface passivation on charge carrier dynamics, steady-state photoluminescence (PL) and ultrafast transient absorption spectroscopy (TAS) measurements were conducted. The steady-state PL spectra (**Figure 41a**) show that CQD-ABT films have a higher PL intensity than CQD-EDT films, indicating better surface passivation. Ultrafast transient absorption spectroscopy (**Figure 41b**), after fitting with three exponential functions, revealed three charge recombination mechanisms: ultrafast Auger recombination, medium electron-hole recombination, and long negative band-tail state decay. The ultrafast lifetimes for CQD-EDT and CQD-ABT were 3.15 ps and 3.31 ps, while the medium lifetimes were 42.6 ps and 50.5 ps, respectively. Long lifetimes were 2.1 ns for CQD-EDT and 2.5 ns for CQD-

ABT. The higher PL intensity and longer lifetimes of CQD-ABT confirm improved defect passivation and reduced trap states.

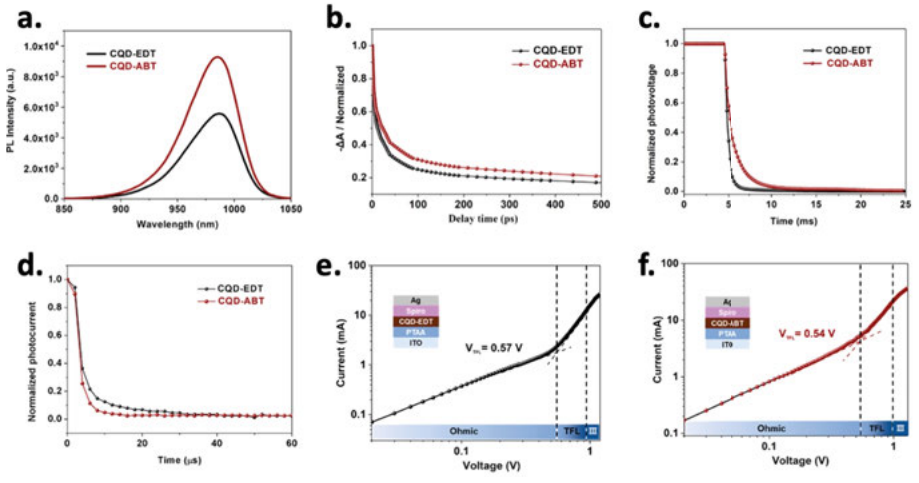

Figure 41. (a) Steady-state PL spectra and **(b)** TA decay curves of the p-type CQD-EDT and CQD-ABT solid films. **(c)** Normalized TPV and **(d)** TPC decay curves of EDT-based and ABT-based CQDSCs. SCLC curves of **(e)** CQD-EDT and **(f)** CQD-ABT solid films. The insets show the device structures for SCLC measurements. Figure adapted from **Paper IV**.

To gain further insight into the improved performance of the ABT-based devices, we investigated the charge carrier dynamics using transient photovoltage (TPV) and transient photocurrent (TPC) measurements. As shown in **Figure 41c**, the ABT-based devices exhibited longer charge carrier lifetimes (1.36 ms) compared to the EDT-based devices (0.98 ms), indicating reduced charge recombination. The TPC measurements (**Figure 41d**) also revealed faster charge transport times in the ABT-based devices, further supporting the conclusion that ABT passivation improves charge extraction.

Additionally, space charge-limited current (SCLC) measurements were conducted, using only hole transport devices, to quantify the trap density in the CQD films (**Figure 41e,f**). The CQD-ABT films exhibited a slightly lower trap density (1.62×10^{16} cm^{-3}) compared to the CQD-EDT films (1.71×10^{16} cm^{-3}) and a lower trap-filled limit voltage (V_{TFL}). This reduction in trap density is consistent with the improved surface passivation provided by ABT, which leads to fewer recombination losses and higher device efficiency.

Device Stability Under Continuous Illumination

In addition to enhanced efficiency, the ABT-based CQDSCs demonstrated excellent stability under continuous illumination. As shown in **Figure 40e**, the ABT-based devices maintained 97% of their initial PCE after 130 hours of continuous illumination at 100 mW/cm^2. This stability is comparable to that of EDT-based devices, which have been shown to maintain high levels of

stability under similar conditions in the literature.[237,238] The high photostability of the ABT-based CQDSCs further supports the use of ABT ligands as a superior alternative to EDT for long-term photovoltaic applications.

Conclusion

The findings from this study had important implications for the broader field of quantum dot solar cells, particularly in tandem solar cell configurations. In **Project I**, we explored the integration of CQDs with perovskite and dye-sensitized solar cells to create tandem devices. However, the performance of these tandem devices was limited by the poor performance of the CQD sub-cells, which suffered from high recombination losses and inefficient charge extraction. The results presented in **Paper IV** showed that the shortcomings of CQDs could be addressed through careful ligand selection. By replacing EDT with ABT, we significantly improved surface passivation, reduced recombination, and enhanced charge extraction. These improvements are expected to directly translate into better performance in tandem solar cell configurations, where efficient infrared light absorption by CQDs is crucial for maximizing overall power conversion efficiency.

In summary, this study highlighted the significance of ligand selection in enhancing the performance of p-type CQDs for infrared solar cells. Through comprehensive theoretical and experimental investigations, we demonstrated that ABT ligands provided superior surface passivation compared to traditional EDT ligands. The improvements in charge extraction, reduced recombination losses, and enhanced stability confirmed the potential of ABT as a better ligand for CQD solar cells. These findings reinforce the importance of tailored surface chemistry in optimizing CQD performance and pave the way for future progress in tandem solar cell technology. More broadly, this work underscores the growing importance of interfacial and surface engineering in the development of high-performance quantum dot-based photovoltaic devices. By understanding and controlling the chemical and physical interactions at the surface of quantum dots, we can unlock further advancements in the efficiency of solar cells, not only in tandem configurations but across a range of applications in energy harvesting and conversion.

Paper V: Interfacial charge transfer dynamics between 2H-MoS2 and PbS quantum dots, the role of quantum confinement

This study investigates the charge transfer dynamics between PbS QDs and monolayer 2H-MoS_2 using Time-Resolved Photoelectron Spectroscopy. 2H-MoS_2 shows potential as a charge extraction layer to enhance charge separation and extraction efficiency in QD-based solar cells. We focus on how quantum confinement and the choice of ligands impact the efficiency of charge separation and recombination at the interface.

Experimental Methods and Sample Preparation

We synthesized the PbS QDs with halide (PbI_2/$PbBr_2$) and ethanedithiol (EDT) ligands using a standard hot-injection method, followed by liquid-state and solid-state ligand exchange respectively (**Figure 42a**). Monolayer 2H-MoS_2 was produced via Chemical Vapor Deposition (CVD) on Si/SiO_2 substrates, onto which we later spin-coated thin films of PbS QDs. The samples were prepared with film thicknesses of 25 nm for the EDT-treated QDs and 50 nm for the halide-treated QDs (samples with halide ligands will be indicated by -PbI_2). The combination of PbS and MoS_2 forms heterostructures that were characterized using XPS, prior to TRPES measurements, to investigate the core-level binding energies of the constituent elements.

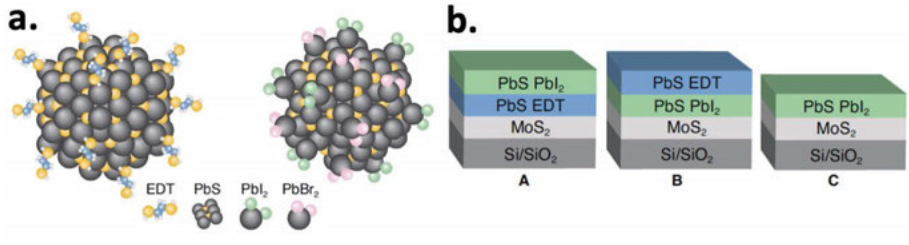

Figure 42. (a) Schematic of PbS QDs with EDT and PbI_2 ligands. **(b)** Schematic description of samples A, B and C measured with TRPES. Figure adapted from **Paper V**.

The spectroscopic studies were performed at the PM4 end-station at the Low-DosePES beamline at BESSY II. Measurements were conducted using a 10.4 kHz laser with a wavelength of 515 nm and a pulse duration of 350 fs. Utilizing a pulsed laser source, we optically excited the MoS_2/PbS system and tracked the binding energy shift of the Pb 4f electrons, enabling us to examine the photovoltage generated at the interface. We investigated differences in photovoltage between various junction configurations involving 2H-MoS_2, PbS-PbI_2 QDs and PbS-EDT QDs (**Figure 42b**). This study provided insights into the charge dynamics at the interfaces.

Role of 2H-MoS_2 as a Hole Transport Material

2H-MoS_2, a widely studied Transition Metal Dichalcogenide (TMDC), exhibits strong potential for optoelectronic applications due to its two-dimensional nature, which provides excellent charge transport properties and enhanced surface-to-volume ratio for better interaction with quantum dots. In the studied system, monolayer 2H-MoS_2 serves as a charge extraction layer, facilitating efficient separation and extraction of photogenerated electron-hole pairs at the interface with PbS QDs. While previous studies have shown that holes are efficiently transferred from PbS QDs to MoS_2, electron transfer is less favored, highlighting the potential selectivity of MoS_2 in charge extraction.[239–241] This selective extraction capability makes MoS_2 a promising material for

improving the energy alignment and overall charge extraction efficiency in QD-based heterostructures.

X-ray Photoelectron Spectroscopy (XPS)

First, XPS characterization was conducted, prior to the time-resolved measurements, to determine the elemental composition and electronic structure of the samples. The core-level spectra of sulfur, lead, and iodine were analyzed, revealing information about the surface chemistry and ligand interactions.

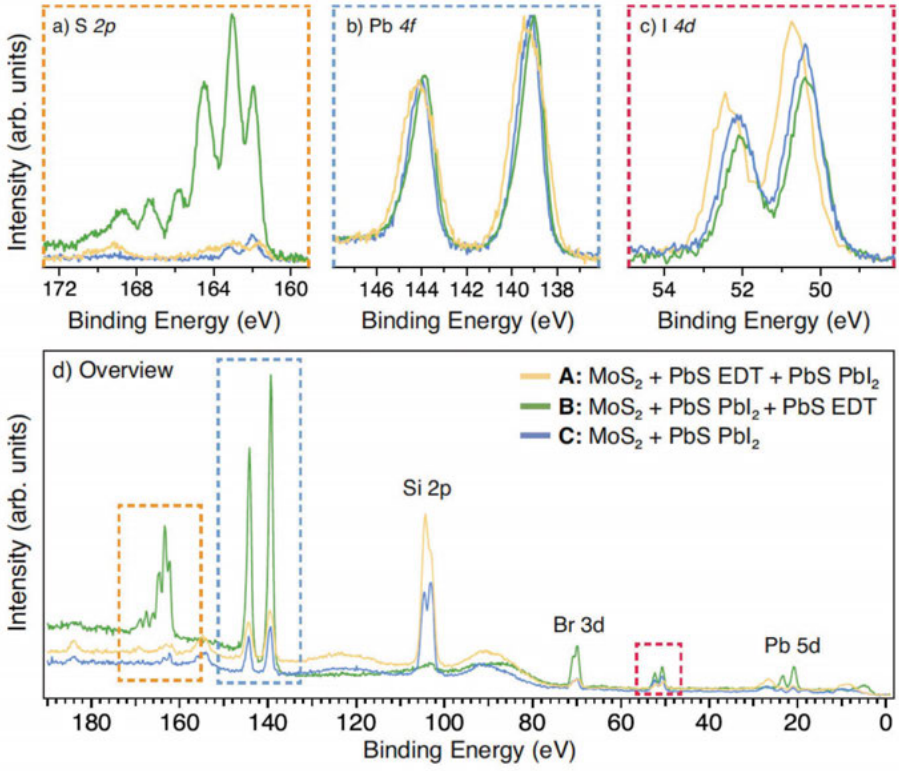

Figure 43. Core level XPS spectra of the: **(a)** Sulfur 2p, **(b)** lead 4f, **(c)** iodine 4d. **(d)** Overview spectrum of all samples, recorded at photon energy 350 eV. Figure adapted from **Paper V**.

Figure 43 presents the sulfur spectra, showing similarities between samples A and C, with two main components of the S 2p peak at 161.63 eV and 162.98 eV for sample A, and at 161.97 eV and 163.19 eV for sample C. In the sample with PbS-EDT on the surface, we observed several sulfur species, indicating both PbS and oxidized states of S 2p, highlighting the role of ligand exchange in modifying the electronic properties of the QDs.

The Pb 4f spectra revealed a distinct lead species at 139.01 eV ($4f_{7/2}$) for the PbS-EDT sample, confirming the formation of PbS. For the samples with PbI_2, we identified two lead species at 138.98 eV and 139.82 eV. The iodine spectra indicated the presence of I 3d peaks at 50.34 eV and 52.03 eV for the PbS-EDT sample. For the PbI_2 samples, the peaks shifted to higher binding energies, suggesting a change in chemical environment due to ligand interactions.

Charge Dynamics Investigation

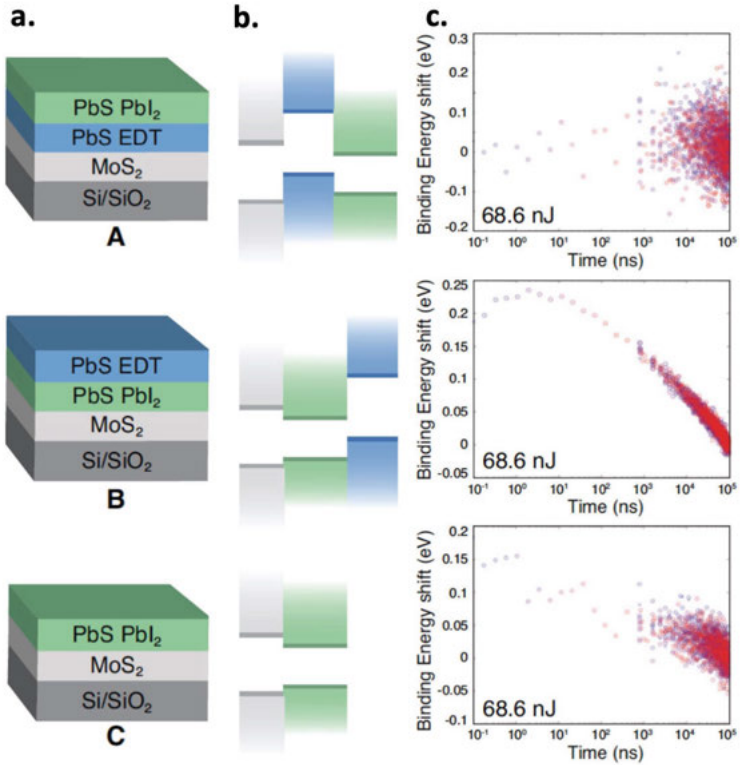

Figure 44. (a) Schematic description of samples A, B and C. **(b)** band diagram of respective sample. **(c)** TRPES spectrum of the Pb 4f core-level shift as a function of delay time between laser and X-ray pulse. Laser power of 68.6 nJ and excitation energy 350 eV. Figure adapted from **Paper V**.

TRPES measurements were conducted to investigate the charge transfer dynamics at the PbS/MoS_2 interface. By tracking the shift in binding energy of the Pb 4f core level as a function of the delay time between the laser (pump) and X-ray (probe) pulses, the generated photovoltage and charge separation dynamics were probed. Three different junction configurations were studied as shown in **Figure 44a** and represented by sample A, B, and C. The results

showed that sample B exhibited the largest photo-induced voltage shift (0.24 eV), followed by sample A (0.22 eV) and sample C (0.16 eV). This indicates that the ligand choice and junction orientation significantly affect the efficiency of charge separation.

Influence of Laser Power on Photovoltage Generation

The influence of laser power on the generated photovoltage was investigated for sample B, which had the highest observed photovoltage. By varying the laser power from 0.8 nJ to 274.0 nJ per pulse, a clear dependence on both the magnitude and timescale of the photovoltage was observed (see **Figure 45**). Results indicated that higher laser power correlates with an increased binding energy shift of the Pb 4f core level. Additionally, the time scale for maximum peak photovoltage generation was shorter at higher laser powers, indicating a rapid charge generation and separation process. These findings highlight the importance of optimizing laser excitation parameters to control the photovoltage generation and enhance charge separation efficiency in these heterostructures.

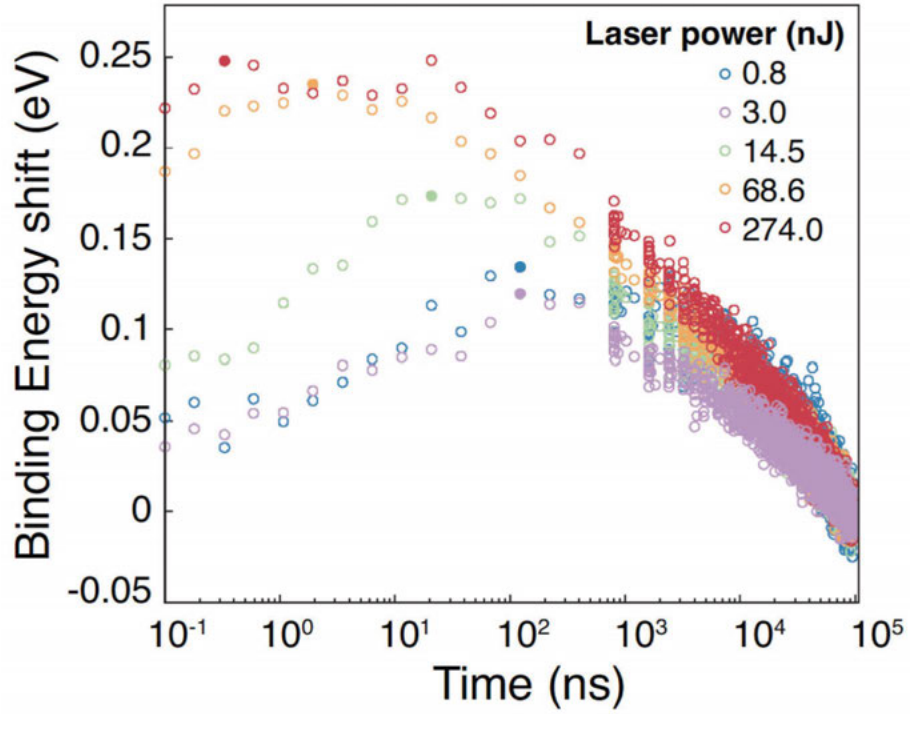

Figure 45. Time-resolved measurements for sample B with monolayer 2H-MoS_2 + PbS PbI_2 + PbS EDT with laser power 0.8 nJ, 3.0 nJ, 14.5 nJ, 68.6 nJ and 274.0 nJ. Figure adapted from **Paper V**.

Kinetics of Charge Separation and Recombination

The TRPES measurements provided insights into the kinetics of charge separation and recombination at the PbS/MoS_2 interface. The binding energy shift of the Pb 4f core level, indicative of photovoltage generation, was used to study the timescales of these processes. For all three samples, the photovoltage reached its maximum within a few picoseconds, with recombination occurring on a longer timescale. Sample B, with the PbS-PbI_2 QDs, demonstrated faster charge separation kinetics compared to samples A and C, suggesting that the PbI_2 ligand plays a critical role in promoting efficient charge separation.

Conclusions

This study highlights the role of surface ligands in controlling the interfacial charge transfer dynamics between PbS QDs and 2H-MoS_2. The choice of ligand significantly impacts photovoltage generation and the kinetics of charge separation. Halide-capped PbS QDs demonstrated superior performance in terms of both photovoltage magnitude and charge separation speed compared to EDT-capped QDs. These findings emphasize the potential of 2H-MoS_2 as a charge extraction layer in QD solar cells, facilitating selective charge transfer and extraction.

Moving forward, we aim to further explore the interplay between charge dynamics and interface properties in QD-based systems. By tuning the energy landscapes at the junctions and utilizing advanced time-resolved techniques, we seek to enhance charge separation and minimize recombination losses, ultimately improving the efficiency and stability of QD-based solar cells.

This research underscores the critical role of surface and interface engineering in optimizing the performance of quantum dot-based photovoltaic devices. As the field of quantum dot solar cells continues to progress, understanding and controlling the interactions at the interfaces between quantum dots and charge transport materials will be key to overcoming current limitations and advancing device efficiency. The insights gained here not only contribute to improving QD-based systems but also open the door for innovations in the broader field of nanomaterial integration in renewable energy technologies.

Project III: Charge Transport and Recombination Control in PbS Quantum Dot Solar Cells

The performance of PbS CQDs was found to be a bottleneck of **Project I** due to high charge recombination rates and inefficient charge transport, despite their promising spectral properties for infrared light absorption. These issues underscored the need for a more focused study on charge dynamics, particularly in controlling recombination and optimizing charge extraction mechanisms in PbS CQD solar cells. **Project II** focused on optimizing charge extraction and reducing charge recombination by investigating and tailoring

charge transporting materials and improving surface passivation, with notable advancements achieved through ligand engineering, as highlighted in **Paper IV** and **Paper V**.

Project III, involving **Paper VI** and **VII** aimed to serve as the extension of the previous work, targeting the exploration of the mechanisms that govern charge carrier dynamics and recombination processes at the interfaces of PbS CQD-based devices. The objective was to try to identify the drawbacks in carrier dynamics in PbS colloidal quantum dot solar cells through the optimization of quantum dot size and film thickness. **Paper VI** analyzed charge transport and recombination dynamics using time-resolved photoelectron spectroscopy, focusing on the impact of film thickness on charge mobility and efficiency.

Following that research, **Paper VII** investigated how varying quantum dot sizes affect charge transport, recombination rates, and overall photo-voltaic efficiency, highlighting the importance of tuning all the layers in the device for different QD sizes, to enhance device performance.

Paper VI: Time-Resolved Photoelectron Spectroscopy on PbS Quantum Dots

In this section, we present the detailed results from our investigations utilizing time-resolved photoelectron spectroscopy (TRPES) on lead sulfide (PbS) quantum dot samples. Our study aimed to gain insights into charge carrier dynamics at the interfaces of materials that are significant for photovoltaic applications, specifically focusing on the mechanisms that influence the performance of PbS quantum dot solar cells. By employing TRPES, we were able to observe charge transport and recombination processes that are crucial for enhancing quantum dot solar cell efficiencies, particularly in tandem configurations.

Sample Preparation and Characterization

In this study we prepared thin films of PbS quantum dots using a highly concentrated quantum dot ink containing lead iodide/bromide ligands in a 5:1 molar ratio. This ink was deposited onto indium-doped tin oxide (ITO) substrates that were pre-coated with a thin layer of magnesium-doped zinc oxide (MgZnO), serving as an electron extraction layer. The complete solar cell architecture was finalized with a p-type PbS layer treated with 1,2-ethanedithiol (EDT) as a ligand, and a thin gold layer for the back contact, as illustrated in **Figure 46**.

Following sample preparation, we characterized the thin films using steady-state photoelectron spectroscopy (PES) before conducting TRPES measurements. The core-level binding energies indicated the presence of both sulfur and lead species typical of PbS quantum dots. The S/Pb ratio measured was approximately 1:2, indicating high-quality bulk material with minimal oxidation, which is critical for effective charge dynamics.

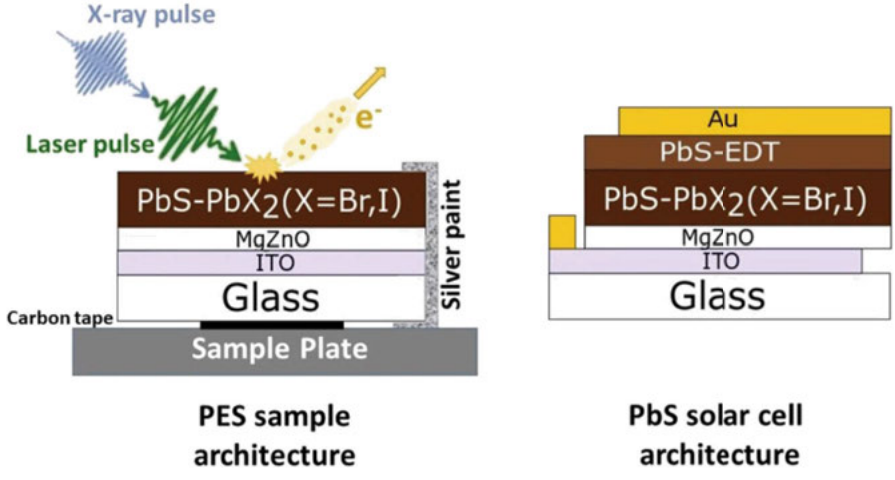

Figure 46. Architecture of QD samples used in photoelectron spectroscopy (left). The sample is connected to a metal sample plate through carbon tape and is grounded by applying silver paint. Architecture of a PbS-QD solar cell, which also includes a quantum dot layer with ethanedithiol ligand (EDT) and a gold contact (right). Figure adapted from **Paper VI**.

TRPES Measurements and Methodology

The TRPES experiments were conducted at the LowDosePES end-station at the BESSY II synchrotron. The X-ray pulses were synchronized with external laser pulses, enabling us to monitor changes in core-level peak positions over time. This setup allowed for a comprehensive examination of charge dynamics and photovoltage generation within the PbS QDs across a broad temporal window, spanning six orders of magnitude from 10^{-1} to 10^{5} ns.

We generated trigger time maps of the Pb 5d core level to observe shifts indicative of charge separation and photovoltage generation. For example, in **Figure 47a**, a shift in the core level position was evident at delay times below 20 μs, highlighting the rapid dynamics of charge carrier processes following laser excitation.

In addition to trigger time maps, we executed delay scans that revealed the evolution of binding energy shifts at various laser to X-ray delay times **(Figure 47b)**. The extensive dataset generated from these scans, comprising 1800 spectra, facilitated intricate kinetic analyses. We employed a fitting routine using Gaussian peaks and a polynomial background to extract parameters related to binding energy shifts.

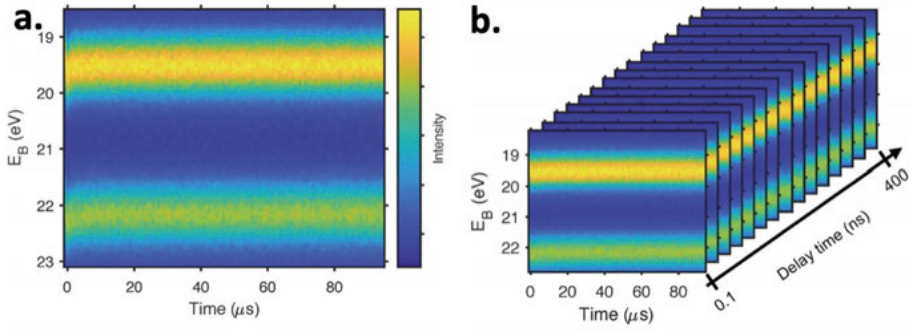

Figure 47. Visualisation of the data obtained in TRPES measurements: **(a)** Trigger time map of the Pb 5d core level measured at a delay time of 122 ns for a 250 nm thick PbS quantum dot sample with a laser pulse energy of 15.4 nJ and a probe energy of 90 eV. **(b)** Visualization of a delay scan on the same sample. Trigger time maps are obtained at 15 different pump-probe delay times. Figure adapted from **Paper VI**.

Our results exhibited clear variations in peak positions, with the photovoltage demonstrating a distinct temporal evolution that correlated with charge carrier dynamics. Notably, we observed that the average binding energy position shifted over time, indicating ongoing charge separation and recombination processes.

Influence of Laser Power and Quantum Dot Film Thickness

We further investigated the impact of laser power and quantum dot film thickness on the kinetics of binding energy changes. Our findings indicated that increasing the laser pulse energy enhanced the magnitude of the binding energy shift, which corresponded to greater charge separation and higher photovoltage generation (**Figure 48**). The photovoltage decay kinetics were modeled using multi-exponential fits, which highlighted the complex nature of the underlying processes.

Table 5. Maximum photovoltage (V_{max}) and delay time at which the maximum photovoltage was observed (t_{max}) of kinetic traces obtained for the 250 nm and the 50 nm thick PbS samples at laser pulse energies of 15.4 and 4.3 nJ.

PbS thickness/nm	**250**	**250**	**50**	**50**
Laser pulse energy/nJ	15.4	4.3	15.4	4.3
V_{max}/eV	0.160	0.123	0.150	0.096
T_{max}/ns	69	145	18	27

The influence of quantum dot film thickness on charge transport dynamics was particularly notable. Thinner PbS quantum dot films exhibited faster rise times for photovoltage generation due to reduced distances for charge carriers to traverse before reaching the substrate (**Table 5**). Conversely, thicker films demonstrated slower charge transport, implicating charge mobility as a limiting factor in these thicker structures.

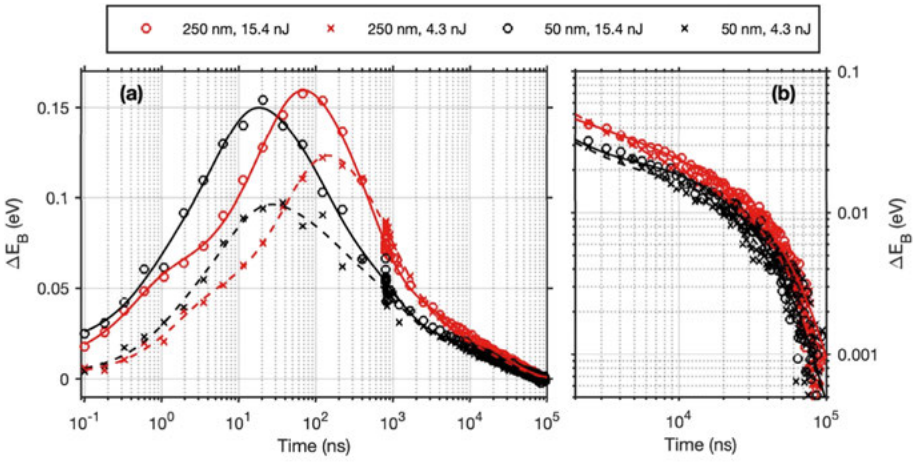

Figure 48. Kinetic traces obtained from delay scans on two PbS quantum dot samples with different thicknesses (250 nm, red and 50 nm, black) at two different laser pulse energies (15.4 nJ, circles and 4.3 nJ, crosses). Multiexponential fits to the data are included as a guide to the eye. **(a)** Complete time range, **(b)** focus on longer times (> 2 μs) of the same delay scans with both axes on a logarithmic scale. Figure adapted from **Paper VI**.

Recombination Dynamics

The decay of photovoltage was also analyzed in terms of recombination rates. We speculated that the recombination dynamics depended on several factors, including charge trapping in the MgZnO layer and the rate of hole diffusion. Notably, the increased thickness of the PbS QD film provided a larger volume for hole dispersion, which could affect the recombination kinetics and overall charge dynamics.

Conclusions and Implications for Quantum Dot Solar Cells

In conclusion, our study illustrated the effectiveness of TRPES in probing charge dynamics within PbS quantum dot solar cells. We elucidated the mechanisms of charge separation and recombination across interfaces, which are crucial for optimizing solar cell performance. The insights gained from our TRPES measurements contribute to the understanding of factors limiting quantum dot performance and offer pathways for future enhancements in tandem configurations.

The results underscored the importance of optimizing ligand exchange, film thickness, and charge transport dynamics to enhance the efficiency and stability of quantum dot solar cells. Future work will focus on extending these findings to investigate other material interfaces within solar cell architectures, thereby advancing the development of high-efficiency photovoltaic devices.

By providing a deeper understanding of the intrinsic properties of quantum dots and their behavior in photovoltaic devices, this work contributes to the ongoing evolution of solar cell technologies. These findings not only advance quantum dot-based systems but also have broader implications for a wide range of materials and device architectures, paving the way for more efficient, stable, and cost-effective renewable energy solutions. The insights gained here can influence the design of more efficient tandem solar cells, inspire the development of novel material combinations, and guide future research in the pursuit of sustainable energy technologies.

Paper VII: Comparing Charge Generation, Transport, and Recombination in PbS Quantum Dot Solar Cells Prepared from Two Sizes of Quantum Dots

In this study, we investigated the charge generation, transport, and recombination dynamics in lead sulfide (PbS) quantum dot solar cells (QD SCs) utilizing two different sizes of PbS quantum dots: PbS1-OEA and PbS2-OEA. The performance of these solar cells is influenced by the electronic properties of the quantum dots, which can be tailored by adjusting their size and ligand environment. Our findings provide critical insights into the interplay between charge dynamics and photovoltaic efficiency, emphasizing the role of quantum dot size and charge extraction layer, in optimizing solar cell performance.

Synthesis and Characterization of Quantum Dots

The PbS colloidal quantum dots were synthesized using a modified hot injection method, resulting in two distinct oleic acid (OEA) capped QD solutions: PbS1-OEA and PbS2-OEA. As shown in **Figure 49**, the optical UV-Vis absorption spectra revealed a significant redshift of the peak from PbS1-OEA (1.31 eV) to PbS2-OEA (1.09 eV), indicating a larger diameter for the PbS2-OEA QDs. This size-dependent behavior is further supported by the steady-state emission spectra, where the first excitonic peak is found at 1.17 eV for PbS1-OEA and at 0.98 eV for PbS2-OEA.

The light absorption peaks for PbS1-OEA and PbS2-OEA are of similar width, suggesting that the size distribution for both QD samples is comparable. The photoluminescence quantum efficiency (PLQE) measurements indicated a value of approximately 40% for PbS1-OEA, while PbS2-OEA exhibited a PLQE of around 16%, suggesting increased non-radiative recombination in the larger QDs. These findings suggest that the higher PL for the PbS1 QDs might be an effect of better surface passivation and not necessarily related to the QD size, setting the stage for evaluating their performance in solar cell applications.

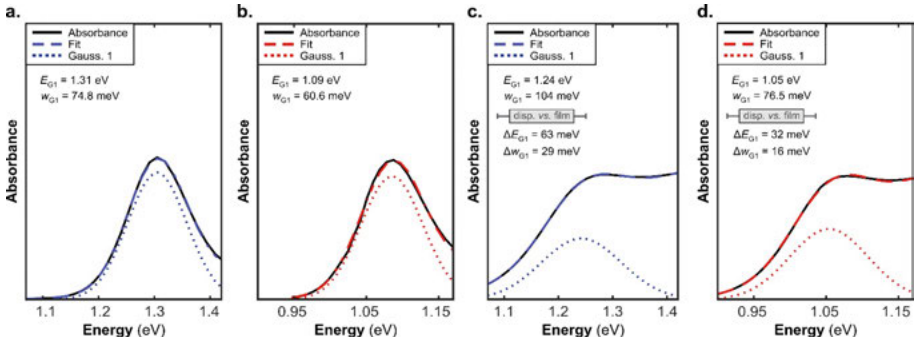

Figure 49. Steady-state absorption spectra, including Gaussian fits, showing the lowest energy exciton band for **a)** PbS1-OEA and **b)** PbS2-OEA dispersed in octane. E_{G1} is the centre peak position (in eV) and w_{G1} is the width of the 1st exciton absorption obtained from the lowest energy Gaussian (Gauss. 1; dotted lines). The dashed lines represent the total fit result. The corresponding results for the halide coated PbS QD films are shown in **c)** for PbS1-X_2 and **d)** for PbS2-X_2 films. The peak shift (ΔE_{G1}) and broadening (Δw_{G1}) relative to the dispersions are shown in the insets. Figure adapted from **Paper VII**.

Recombination Mechanisms in QD Solar Cells

In solar cells, various recombination mechanisms significantly impact overall device performance, including radiative recombination, non-radiative recombination through defect states, and interface recombination. Radiative recombination involves the emission of photons when an electron and hole recombine. While intrinsic to semiconductor materials, this process is often overshadowed by non-radiative recombination, which occurs through defect states on the surface of the QDs or traps within the QD material, capturing carriers and releasing energy as heat rather than photons. Interface recombination occurs at the boundaries between different materials, where the energy alignment of conduction bands or valence bands can create conditions favorable for increased recombination (for example energy barriers, or interface states), resulting in lower charge collection efficiency and reduced power conversion efficiency.

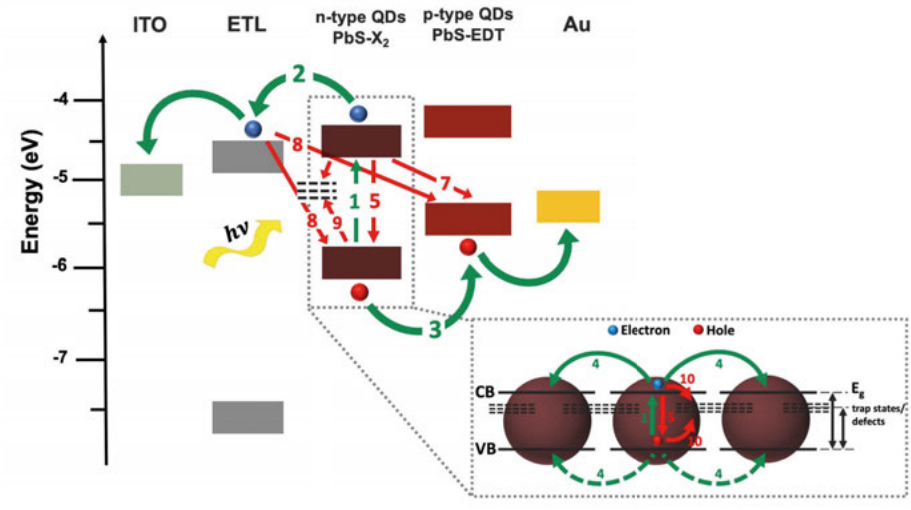

Figure 50. Schematic representation of charge carrier dynamics in quantum dot thin films. Green arrows refer to charge transport processes occurring in QD solar cell: electron-hole pairs (exciton) production (1), electrons and holes hopping between QDs (4), electrons and holes being collected respectively by electron transporting layer (2) and hole transport material (3) and then transported to respective electrodes. Red arrows refer to possible recombination routes in the QD solar cell: recombination of photogenerated species (5), back charge transfer at the following interfaces within the cell: ETL – PbS (6), HTM - PbS (7) and ETL – HTM electrodes. Red arrows refer to possible recombination routes in the QD solar cell: recombination of photogenerated species (5), back charge transfer at the following interfaces within the cell: ETL – PbS (6), HTM - PbS (7) and ETL - HTM (8), recombination of electrons/holes to interface trap states (9) or bulk trap states (10). VB and CB are valence and conduction band respectively and E_g is electronic band gap energy. Figure adapted from **Paper VII**.

Figure 50 illustrates charge carrier dynamics in QD thin films, with green arrows indicating charge transport and red arrows representing various recombination pathways. These include recombination within the QDs (5), back charge transfer at the ETL-QD (6) and HTM-QD (7) interfaces, recombination at the ETL-HTM (8) interface and recombination to interface trap states (9) and bulk trap states (10). Energy misalignment or increased trap state density can significantly increase the likelihood of carriers recombining before collection, diminishing overall device efficiency. This is particularly notable in PbS2 devices and supported by various measurements in further sections. The larger diameter of PbS2 QDs may result in more pronounced bulk trap states, increasing the likelihood of non-radiative recombination. Additionally, the activation energy for recombination in the PbS2 QD based devices deviates significantly from the expected bandgap energy, indicating inefficient charge injection and enhanced interface recombination at the AlZnO/QD layer. This

poor energy alignment leads to substantial losses in open-circuit voltage (V_{oc}) and short-circuit current density (J_{sc}), ultimately reducing solar cell efficiency.

In conclusion, understanding and addressing these recombination mechanisms, particularly at the ETL interface, is crucial for enhancing the performance of PbS QD solar cells, especially those utilizing larger QDs like PbS2.

Device Fabrication and Photovoltaic Performance

Using a layer-by-layer deposition approach, we fabricated complete solar cells incorporating both quantum dot sizes. Active layers of PbS quantum dots (QDs) passivated with halides (iodide and bromide, denoted as X_2) - referred to as PbS1-X_2 and PbS2-X_2 – were used, along with 1,2-ethanedithiol (EDT)-capped QD films serving as hole transporting materials (**Figure 51a**). The current-voltage characteristics of these devices, measured under AM1.5G 100 mW/cm² illumination, are presented in **Figure 51b**.

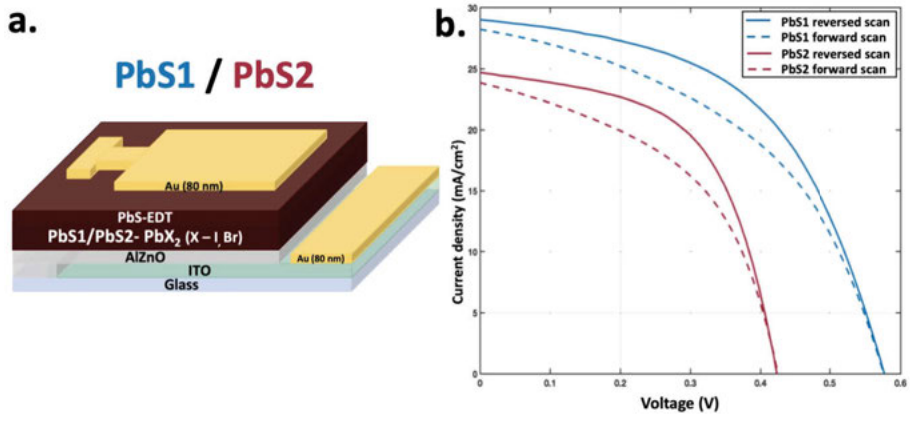

Figure 51. (a) Schematic of the PbS1 and PbS2 colloidal quantum dot solar cells structure used. **(b)** Current – voltage characteristics with summary of photovoltaic parameters (PCE, FF, J_{sc} and V_{oc}) of PbS 1 CQD (blue) and PbS 2 CQD (red) solar devices of architecture as shown in scheme (a), with different scanning directions. Figure adapted from **Paper VII**.

From the analysis of photovoltaic parameters summarized in **Table 6**, we observed that PbS1 CQD solar cells exhibited a power conversion efficiency (PCE) of approximately 8.7%, with an open-circuit voltage (V_{oc}) of 580 mV, a short-circuit current (J_{sc}) of 29 mA/cm², and a fill factor (FF) of about 52%. In contrast, the PbS2 CQD solar cells showed inferior performance, with a PCE of approximately 5.9%, V_{oc} of 420 mV, J_{sc} of 25 mA/cm², and a slightly increased fill factor of around 56%.

Table 6. Photovoltaic parameters extracted from the current-voltage characteristic in **Figure 51b**.

Device	Scan direction	PCE(%)	FF(%)	J_{sc}(mA/cm^2)	V_{oc}(mV)
PbS1	*Reverse*	8.7	51.8	29.0	580
	Forward	7.5	46.2	28.2	580
PbS2	*Reverse*	5.9	56.2	24.7	420
	Forward	4.9	48.1	23.3	420

The observed decrease in photovoltaic performance for the PbS2 solar cells can be attributed to several factors, including increased recombination processes resulting from larger QD diameter and potential interface issues between different device layers. The decrease in V_{oc} may be linked to enhanced recombination at these interfaces, while the reduced J_{sc} is likely due to increased non-radiative recombination of charge carriers within the solar cell.

Both devices exhibited hysteresis in the J-V curves under forward bias, attributed primarily to a decrease in FF with changes in applied bias, further indicating enhanced recombination of charge carriers within the semiconductor material or at interfaces.

Temperature Dependence of Photovoltaic Parameters

To further understand the charge dynamics, we estimated the activation energy (E_a) for both PbS1 and PbS2 devices from V_{oc} as a function of temperature, as depicted in **Figure 52a**. Utilizing the standard diode equation, we found that the activation energy for PbS1 devices was approximately 1.30 eV, closely matching the energy bandgap calculated from UV-Vis measurements (Eg = 1.31 eV). In contrast, for PbS2 devices, the estimated activation energy of 1.34 eV significantly deviated from the calculated bandgap of 1.09 eV (see **Figure 49a,b**). This discrepancy suggests potential inefficiencies in charge injection from the QDs to the electron transport layer (ETL), further supported by the lower photovoltaic performance of the PbS2 devices.

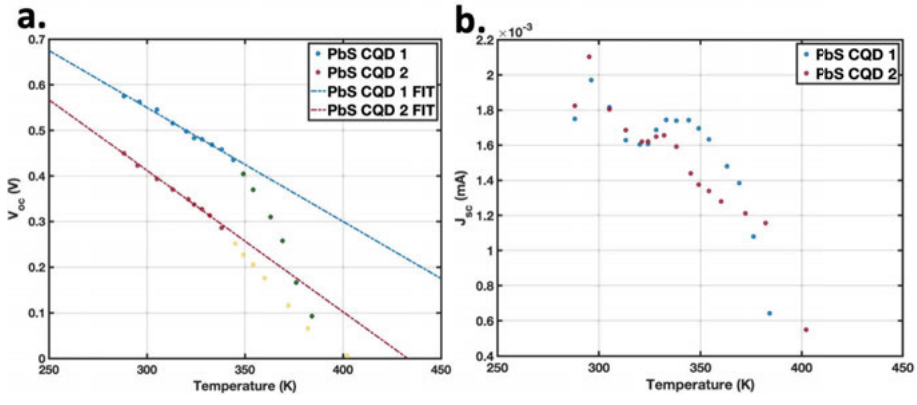

Figure 52. Linear regression plots of PbS1 (blue) and PbS2 (red) solar cell devices: **(a)** the open circuit voltage (V_{oc}) as a function of temperature, **(b)** the short circuit current (J_{sc}) as a function of temperature. Figure adapted from **Paper VII**.

As illustrated in **Figure 52b**, the photocurrent exhibited a peak around 300 K, decreasing at lower temperatures due to reduced carrier mobility. At elevated temperatures, a decrease in photocurrent was observed, likely due to increased recombination, with degradation processes beginning to manifest at around 350 K.

Light Intensity Dependence of Photovoltaic Parameters

The relationship between light intensity and short-circuit photocurrent (J_{sc}) is depicted in **Figure 53a**, revealing a power factor (α) close to 1 for both devices, indicating efficient charge extraction. However, the ideality factor (n) derived from the open-circuit voltage as a function of light intensity (**Figure 53b**) showed values of $n \approx 1.93$ for PbS1 and $n \approx 1.44$ for PbS2, indicating trap-assisted recombination as the dominant process in both cases.

Transient photovoltage (TPV) and transient photocurrent (TPC) measurements allowed us to analyze charge carrier dynamics under varying light intensities. The TPV decay half-times for PbS1 devices decreased with increasing light intensity, while the PbS2 devices exhibited shorter TPV half-times across all intensities, further supporting the observation of increased recombination in PbS2 devices.

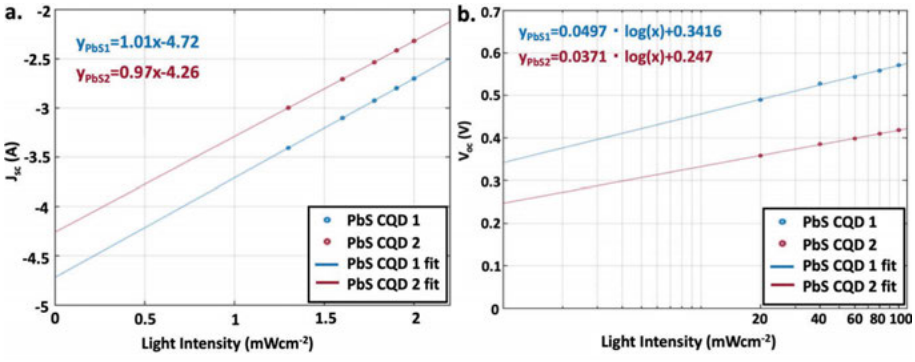

Figure 53. Linear regression plots of PbS1 (blue) and PbS2 (red) solar cell devices: **(a)** the open circuit voltage (V_{oc}) as a function of the light intensity (logarithmic scale), **(b)** the short circuit current (J_{sc}) as a function of the light intensity. All the values were extracted from transient photovoltage and photocurrent measurements at different light intensities (20-100 mW/cm^2) at room temperature. Figure adapted from **Paper VII**.

Charge Carrier Dynamics in PbS Quantum Dot Solar Cells

Utilizing femtosecond transient absorption spectroscopy (fs-TAS), we investigated the photoexcited carrier dynamics in both dispersed PbS QDs and assembled films, examining carrier relaxation, transport, and recombination processes. The transient absorption spectra (**Figure 54**) indicated that photoexcited carriers relax to band-edge states within a sub-ps timescale, followed by a dynamic redshift attributable to charge or exciton transfer between quantum dots.

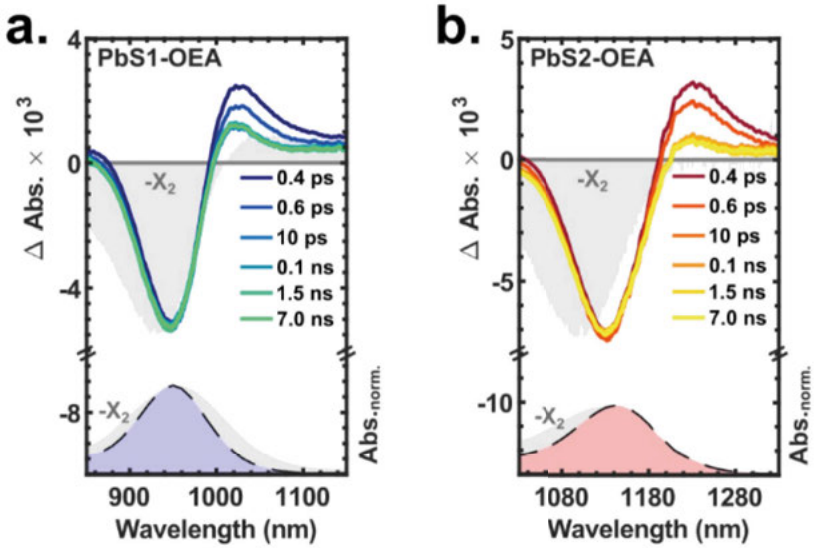

Figure 54. Fs-TA spectra (pump: 750 nm) of **(a)** PbS1-OEA and **(b)** PbS2-OEA dispersed in octane. Their corresponding steady-state absorption spectra are shown at the bottom (dashed lines, colored areas). The grey shaded regions show the fs-TA spectra at t = 1 ns and absorption spectra for PbS-X2 in butylamine. Figure adapted from **Paper VII**.

In our analysis of the halide-coated QD films (PbS-X_2), we observed significant broadening and redshift of the first exciton band compared to the dispersed QDs, with an estimated shift (ΔE) of around 60 meV for PbS1 and approximately 30 meV for PbS2. The redshift dynamics (see **Figure 55**), reflecting carrier hopping probabilities, indicated a higher coupling for the smaller PbS1 QDs, correlating with faster charge transport observed in complete solar cell devices. Furthermore, our transient absorption measurements revealed efficient hole transfer from PbS-X_2 to PbS-EDT, with carriers exploring the energetic landscape of the thick films within approximately 50 ps. This rapid hole transfer contributes to prolonging the lifetime of photogenerated charges in the QDs, thus enhancing overall device performance.

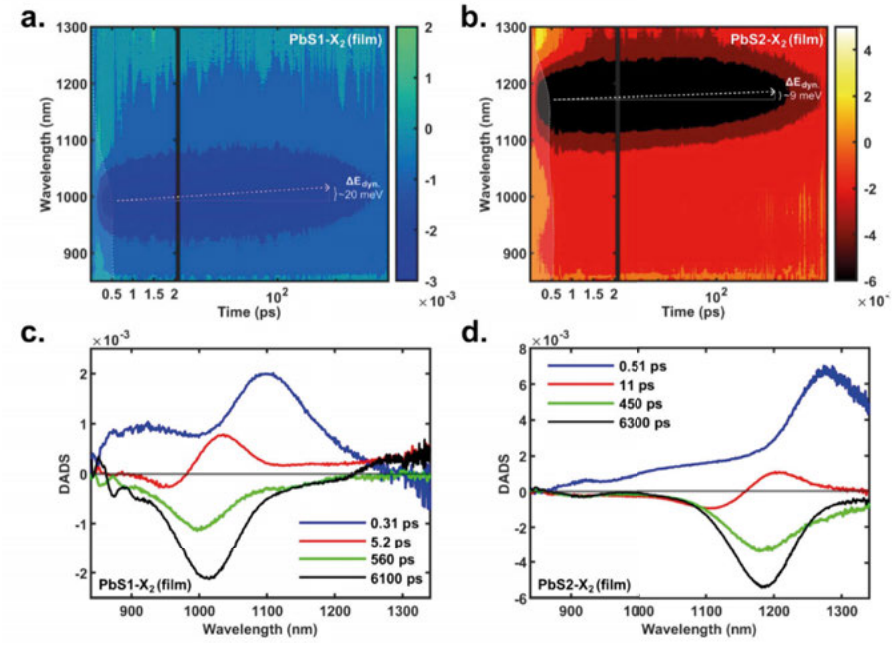

Figure 55. Fs-TA maps (pump: 750 nm) of **a)** PbS1-X_2 and **b)** PbS2-X_2 films. The white arrows in a-b indicate the dynamic redshift with respect to the steady-state absorption (shaded area). DADS obtained from global analysis are shown in **c)** for PbS1-X_2 and **d)** for PbS2-X_2 films. Figure adapted from **Paper VII**.

Conclusions

In summary, our study highlights the critical role of quantum dot size for charge generation, transport, and recombination dynamics within PbS quantum dot solar cells. The PbS1 devices, with smaller QDs exhibited superior charge carrier dynamics compared to the PbS2 devices, with larger QDs, as evidenced by activation energy calculations, power factors, and ideality factors. Higher light intensity resulted in accelerated recombination rates, with the PbS1 devices maintaining efficient charge transport and extraction.

Furthermore, a detailed analysis of the recombination pathways in QDs, has suggested the underlying reasons for the performance differences observed between PbS1 and PbS2 solar cells. Specifically, the devices based on the larger diameter of PbS2 QDs show increased non-radiative recombination, primarily due to enhanced interface issues and energy misalignment at the ETL/QD interface. This poor energy alignment leads to significant losses in open-circuit voltage (V_{oc}) and short-circuit current density (J_{sc}), ultimately reducing solar cell efficiency. These findings underscore the importance of optimizing the ETL/QD interface alignment, to enhance the performance of PbS QD solar cells, especially those utilizing larger QDs like PbS2.

Moreover, transient absorption measurements demonstrated rapid charge dynamics, with efficient hole transfer processes occurring between the QDs and HTM layers, suggesting further pathways to optimize quantum dot solar cell designs. Overall, our findings provide valuable insights into the interplay of charge dynamics in PbS quantum dot solar cells, underscoring the significance of material properties in enhancing photovoltaic performance and stability.

This research illustrates how the intricate balance between quantum dot size, interface engineering, and charge dynamics is crucial for the development of high-performance photovoltaic devices. The findings emphasize the need for a comprehensive approach to material design, focusing on both the intrinsic properties of the quantum dots and the optimization of their interfaces with other materials. These insights extend beyond the specific PbS QD systems studied here, offering broader implications for the design of other quantum dot-based solar cells, as well as emerging materials for next-generation photovoltaic technologies. By advancing our understanding of these charge dynamics, this work lays the groundwork for the development of more efficient and stable solar cells, which are essential for achieving the global goals of renewable energy and sustainability.

Conclusions and outlook

This thesis presents a comprehensive investigation into the integration of quantum dot (QD) solar cells with other photovoltaic technologies for tandem applications. Throughout the research, significant findings from each of the seven papers highlight both the potential of QD-based tandem solar cells and the challenges that must be addressed to enhance their efficiencies. In the thesis, also fundamental aspects of the QD solar cell function are investigated with a range of techniques, to find possible ways for improvement of the QD solar cells.

In **Papers I, II, and III**, the initial focus was on the foundational aspects of integrating QD solar cells with traditional photovoltaic technologies. These papers explored various configurations that could harness the unique properties of QDs while identifying the limitations that currently prevent them from achieving efficiencies comparable to state-of-the-art solar technologies. The research confirmed that quantum dots display remarkable benefits, such as tunable bandgaps and excellent spectral absorption properties, making them promising candidates for use in tandem architectures.

Paper I served as an introduction to the potential benefits of combining QD solar cells with established technologies, in this case a dye-sensitized solar cell. It outlined the advantages of using QDs to capture a broader range of the solar spectrum, particularly in the infrared region, where traditional solar cells may struggle. The paper emphasized that QDs could effectively supplement existing solar technologies by enhancing overall light absorption and conversion efficiency. However, it also highlighted critical challenges, including the high rates of charge recombination and insufficient charge transport in QD materials. These findings set the stage for subsequent research efforts aimed at addressing these limitations.

In **Paper II**, the focus shifted to specific methods of optimizing the performance of QD solar cells when integrated into tandem configuration together with a perovskite solar cell. This paper detailed the design principles necessary for effective light management within tandem devices, including the selection of appropriate layer thicknesses and materials that would maximize light harvesting and minimize losses. It further investigated the role of interfacial engineering to improve the overall tandem device performance through lowering optical losses at interfaces. Although promising strategies were proposed, the paper ultimately concluded that the efficiencies of QD solar cells must be

significantly improved to compete with the highest-performing solar technologies.

Paper III provided a deeper exploration of the electro-optical properties of QD solar cells in tandem applications not only for solar light conversion but also for energy storage. It focused on the investigation of low energy photon conversion to electricity using the QD based photovoltaic devices, and also in tandem QD/perovskite photovoltaic devices. The results indicated that while QD solar cells could be engineered to achieve better light absorption in the IR region, their performance remained significantly hindered by the aforementioned challenges related to charge recombination and transport, particularly for large QDs with absorption in the IR region. The research emphasizes the need for a multifaceted approach to tackle these issues.

The analysis of **Papers I,II and III** revealed that while PbS QD solar cells are capable of efficiently harnessing infrared light in a range of device architectures, and for different applications, their performance is significantly hindered by high charge recombination rates and inefficient charge transport mechanisms. This analysis underscored the necessity of optimizing interfacial dynamics and surface properties to unlock the full potential of QDs in tandem architectures.

The research presented in **Paper IV** shows the critical role of surface passivation in improving the performance of PbS QDs in devices absorbing long-wavelength light. By exploring the use of different thiol ligands, the findings demonstrated that effective surface passivation significantly enhances the efficiency of PbS quantum dots. This work highlighted the importance of optimizing surface chemistry, which directly impacts the electronic properties of the quantum dots. It became evident that high-quality interfaces between QDs and hole transport materials are essential for improved charge extraction and minimized recombination losses in tandem solar cells. Building on these insights, **Paper V** examined the interfacial charge transfer dynamics between PbS QDs and a charge transport material, specifically 2H-MoS_2, emphasizing the role of surface ligands in governing these interactions. The results highlighted the potential suitability of 2H-MoS_2 as a charge extraction layer in QD solar cells, enabling efficient and selective charge transfer. Enhancing the compatibility of quantum dots with charge extraction materials will be critical for improving charge extraction in tandem solar cells.

In **Papers VI and VII**, the focus centered on understanding charge carrier dynamics within PbS quantum dot solar cells, emphasizing the critical processes of charge generation, transport, and recombination. **Paper VI** employed time-resolved photoelectron spectroscopy (TRPES) to probe these mechanisms in detail, revealing that charge transport properties are significantly influenced by quantum dot surface ligands, film thickness, and interfacial properties. The findings underscored the critical impact of quantum dot surface ligands and film thickness on charge transport properties. Efficient charge extraction was identified as a key determinant for maximizing solar

cell performance, with optimized ligand exchange and film properties being crucial to minimizing recombination losses.

Paper VII delved further into how quantum dot size affects charge generation, transport, and recombination dynamics. The findings demonstrated that smaller PbS quantum dots exhibit superior charge transport properties and reduced recombination rates compared to larger QDs, as evidenced by their enhanced activation energies, power factors, and ideality factors. The study also identified challenges associated with larger QDs, such as increased non-radiative recombination and energy misalignment at the electron transport layer (ETL)/QD interface, which contribute to significant losses in V_{oc} and J_{sc}. These results underscore the importance of tailoring quantum dot size and improving energy level alignment at interfaces to optimize device performance.

Throughout this research, several significant limitations concerning PbS QD solar cells were identified. The most critical challenges include high charge recombination rates and inefficient charge transport. Addressing these issues requires a multifaceted approach, combining advanced materials science with innovative device engineering. The studies underscore the necessity for effective surface passivation as a vital strategy to mitigate recombination losses, while optimizing ligand chemistry is also essential to enhance the compatibility of QDs with hole transport materials and improve charge extraction. Furthermore, the impact of quantum dot size on charge transport and recombination rates highlights the need for tailored approaches in designing all the layers in QD-based solar cells. Mastering the interplay between size, surface chemistry, and device architecture will be crucial for enhancing overall efficiency.

The research findings from this thesis lay a solid foundation for the continued advancement of QD solar cells in tandem applications. Several promising avenues for future research have emerged. Enhanced surface engineering could explore alternative ligand chemistries and advanced surface treatment techniques to further minimize recombination losses and enhance charge extraction in QD-based solar cells. Tailoring the surface properties of QDs to optimize their electronic behavior is essential for driving further improvements in performance. For example, while thiol-based or halide-based ligands are commonly used for surface passivation in PbS QDs, especially for smaller diameter QDs, they may not fully address the problem of surface recombination, especially in larger QDs, where the electronic structure is more sensitive to surface states, and the surface may contain other facets, compared to smaller QDs. Therefore, alternative ligands or composite ligand strategies may be required. Inorganic ligands like phosphines and phosphine oxides can offer stronger surface bonding, improving passivation by reducing defects and preventing oxidation, thus enhancing QD stability and minimizing recombination. Amino acids, such as cysteine or glutamine, can also potentially form strong bonds with PbS surfaces, stabilizing them and reducing recombination, especially in larger QDs. Their zwitterionic nature provides additional surface stability and tunability of surface properties to suit different QD sizes, which could be especially beneficial for larger PbS QDs, which are more prone to

recombination. Hybrid ligand systems, combining inorganic and organic components, could provide a synergistic effect, offering strong passivation and improved charge transport, particularly for larger QDs. Conjugated organic molecules, such as anthraquinone derivatives, can passivate surfaces while enhancing light absorption and charge transfer, boosting the efficiency of QDs. Exploring these new passivating alternatives, could significantly enhance the performance of QD solar cells, however a detail research is needed, especially to identify which ligands offer a balance of effective surface passivation, charge transport enhancement, and stability under operational conditions.

Future studies should also further consider hybrid systems that combine QD solar cells with other advanced photovoltaic technologies, such as organic solar cells or other perovskite materials. Such integration, as already shown, could lead to enhanced efficiencies and create innovative solutions for energy conversion.

Lastly, conducting comprehensive long-term stability studies on QD solar cells in tandem configurations is crucial for their commercial viability. Understanding degradation mechanisms and developing strategies to mitigate these challenges will be vital for practical applications in real-world environments.

In summary, this thesis has underlined the potential of quantum dot solar cells for tandem applications while addressing the challenges that limit their efficiency. By systematically investigating the performance dynamics of QD solar cells through the lenses of integration, surface passivation, and charge dynamics, a detailed understanding of the mechanisms at play has been provided. The research findings underscore the need for ongoing efforts to optimize QD solar cell performance. As the quest for sustainable energy solutions continues, the insights gained from this work will contribute to the advancement of high-efficiency photovoltaic devices, ultimately supporting the global transition toward renewable energy sources. The future of quantum dots in tandem solar cell applications is promising, and further exploration in this field will pave the way for breakthroughs that can significantly enhance the efficiency and reliability of solar energy technologies.

Acknowledgments

A PhD journey is never a solo journey. It is full of people who help you with experiments and data analysis and those who take the time to listen and help you drink away your frustrations. Here, I'd like to use the opportunity and express my heartfelt thanks to everyone who simply made it worthwhile.

First and foremost, I want to thank my supervisor *Prof. Erik M. Johansson* for giving me the chance to pursue my PhD. I am especially grateful for your continuous guidance, insightful discussions whenever I needed them and occasional boost of confidence when things were not going according to the plan. Your optimism and passion for science make you an amazing supervisor. I consider myself very lucky to have worked with you.

A very special thanks also goes to my co-supervisor *Prof. Gerrit Boschloo* for his invaluable support, expertise, and constructive feedback throughout my research. I am truly grateful for the opportunity to learn from you.

What would research be without collaborators. My projects would not have been possible without you, *Dr. Xiaoliang Zhang*, thank you for all the experimental knowledge you have taught me at the start of my journey. It was an invaluable foundation for this thesis. A heartfelt thank you also goes to *Dr. Malin Johansson*, for not only helping with the experiments but also for engaging in some really fascinating conversations, both about work and beyond. A big shout-out to *Dr. Marina Freitag* for all the invaluable advice and discussions and for introducing me to the world of possibilities international conferences and internships have to offer. Thank you to *Nora Eliasson and Prof. Leif Hammarstöm, Elin Carthwright, Prof. Andreas Lindbald*, and *Dr. Tamara Sloboda*. Your expertise and insights into time-resolved spectroscopy have opened up an entirely new horizon for me, reminding me of how much more there is to learn. It was truly a pleasure to work with all of you!

Thank you to all my amazing friends and colleagues around Ångström Laboratory, included (but not limited to) *Andjela Brnovic, Anuja Vijayan, Dr. Byeong Jo Kim, Dr. Fuxiang Ji, Dr. Hannes Michaels, Dr. Harnush Durgaryan, Dr. Hua Wu, Dr. Huimin Zhu, Javier Sebastian Alonso, Dr. Jesper Johansson, Dr. Kristina Komander, Dr. Leif Häggmann, Dr. Lin Yuan, Dr. Princess Cabotaje, Rima Charaf, Dr. Shipra Prakash, Dr. Victor Öberg, Dr. Vishnu Vijayakumar, Dr. Yawen Liu* and *Zack Ashworth*. You've all helped me in so many ways—whether it was showing me the ropes with instruments and experiments, having great scientific discussions, helping out with data analysis, or just making the journey more fun with all fantastic times in and

out of the lab. A heartfelt thank you to *Fiona Treber* for being an incredible friend and fellow QD enthusiast. From day one, your kindness, encouragement, and willingness to share your knowledge made all the difference. Whether tackling research challenges, navigating setbacks, or venting over coffee, you were always there with advice, reassurance, and motivation. To *Catherine Johnson*, thank you for being an incredible friend and an irreplaceable part of this journey. You never turned down an after-work pub visit to unwind with good beer and music. Your impeccable taste introduced me to the best Asian cuisine spots, turning every meal into an experience. More than that, you were always there—whether for work-related chaos or life's ups and downs—making everything more manageable and infinitely more fun. I'm beyond grateful for the unforgettable memories we've made.

For my time in Newcastle, thank you to all the incredible friends I met in and outside the Freitag group—*Dr. Natalie Flores-Diaz, Dr. Iacopo Benesperi, Giovanni Spinelli, Harvey Morritt, Timo Keller, David Bradford, Dr. Fabio Cucinotta, Nathan Hill, Ella Fidment, Abigail Seddon,* and *Amy Neild*. You made this time unforgettable, from lab work to countless pub nights, great restaurants, and fantastic group parties.

Thank you to my amazing Gothenburg Krokslättgirlzz gang—*Anna, Hyui, and Nhung*—for the countless fika breaks, lighthearted conversations, and always being there for me. You provided a much-needed escape from work stress and PhD challenges, filling this journey with laughter, confidence, and friendship. I couldn't have done it without you!

Thank you to my amazing friend *Clara*—meeting you nine years ago in Uppsala sparked it all. You're an incredible person, passionate about your work, and you made me believe that pursuing a PhD was possible. Having you by my side throughout this journey made it so much more enjoyable.

To my best friends of over 15 years, *Ola and Agata*—thank you for your constant support and belief in me. Despite the distance and busy lives, you were always there, offering encouragement and the confidence boost I needed to see this through. Your friendship means the world to me, and I will always appreciate knowing I can count on you, no matter the time or place.

To my second family in Sweden—*Erica, Olof, Victor, Elin, Tom, Millie, Aline,* and *Axel*—thank you for your unwavering support throughout this journey. Your kindness and encouragement made Sweden feel like a true second home. From offering advice and a helping hand to ensuring I never faced challenges alone, your support has been a constant source of strength. The incredible adventures we've shared have been a highlight, and I look forward to many more to come. *Axel*, your belief in me and constant encouragement, especially during times of doubt, has been one of the key reasons I've made it through. I love you.

Na koniec chciałabym podziękować mojej rodzinie – *Mamie, Tacie, Ani, Maćkowi, Babci Zosi i Babci Mieci*. Żadne słowa nie oddadzą w pełni, jak bardzo Was szanuję, kocham i jestem wdzięczna za wszystko. Wasze

nieustanne wsparcie i motywowanie mnie do dążenia do lepszego pozwoliły mi być w tym miejscu, w którym teraz jestem. Bez Was nie byłoby mnie.

Popular science summary

The accelerating pace of climate change, underscores the critical need for renewable energy solutions. Fossil fuels have long been the primary source of energy, but their use results in significant greenhouse gas emissions, contributing to global warming. Transitioning to renewable energy sources like solar power has become essential. Solar energy is abundant and has the potential to meet global energy demands, and solar cell devices have the ability to directly convert sunlight into electricity. However, traditional silicon-based solar cells, which dominate the market, have limitations in capturing the full spectrum of sunlight, particularly in the infrared (IR) region, leading to significant energy losses. This gap necessitates the development of new photovoltaic technologies that can harness a broader range of the solar spectrum.

The research presented in this thesis focuses on colloidal quantum dot (CQD) solar cells, a promising technology that addresses the limitations of traditional silicon-based solar cells. CQDs, especially lead sulfide (PbS) quantum dots, possess unique optoelectronic properties, including tunable bandgaps and the ability to harvest infrared light. Quantum dots are very small particles that behave differently from their larger counterparts due to quantum mechanics. They can be tailored to absorb different parts of the sunlight spectrum by changing their size, shape, or surface properties. These features give CQDs high potential for use in tandem solar cells.

Tandem solar cells stack different types of solar cells on top of each other, each layer capturing a different part of the sunlight spectrum. This stacking allows for more efficient use of sunlight compared to a single type of solar cell. For instance, a layer that captures visible light can be paired with a layer that captures infrared light, increasing overall energy conversion. While CQD solar cells offer a potential solution, their individual performance and integration into tandem solar cells present several challenges, such as charge recombination, the need for effective surface passivation, and interfacial optical losses. However, the complexity of optimizing solar cells for maximum efficiency highlights the need for advanced research into CQD performance enhancement and integration into tandem structures. This research is highly relevant as it offers a pathway to more efficient solar devices, contributing to the broader goal of reducing reliance on fossil fuels and mitigating climate change.

The main objectives of this thesis are to investigate the integration of CQD solar cells with other photovoltaic technologies for tandem applications and

to address the challenges that limit their efficiency. The research explores foundational aspects of integrating CQD solar cells with dye-sensitized and perovskite solar cells, optimizes the performance of CQD solar cells through surface passivation and charge carrier dynamics investigation, enhances charge extraction, minimizes recombination losses, and develops advanced materials and device engineering approaches to unlock the full potential of QD solar cells.

This research employs a variety of methods to achieve its objectives. Key techniques include the synthesis of PbS CQDs using a hot-injection method to ensure uniform size and high-quality quantum dots, integration of CQD solar cells in tandem configurations through interfacial engineering, surface passivation techniques to reduce trap states and improve charge transport properties, characterization of photovoltaic performance through current-voltage measurements, and investigation of charge carrier dynamics using advanced spectroscopy methods.

The research findings, described in seven papers, demonstrate the significant potential of QD-based tandem solar cells and the challenges that must be addressed to enhance their efficiencies. **Papers I, II, and III** focus on integrating QD solar cells with other photovoltaic technologies (DSSCs and perovskites). They show that QDs can capture a broader range of the solar spectrum, especially in the infrared region, enhancing overall light absorption and conversion efficiency. However, they also identified critical challenges, such as high charge recombination rates and inefficient charge transport, which hinder QD solar cell performance. As well as importance of effective light management and interfacial engineering. **Papers IV and V** provides deeper insights into improving QD solar cells, demonstrating that surface passivation with different thiol ligands significantly enhances efficiency by reducing recombination losses and showing that efficient charge transfer is crucial for better performance. **Papers VI and VII** focus on understanding charge carrier dynamics within QD solar cells. They show that surface ligands and film thickness greatly influence charge transport properties and reveal that smaller QDs exhibit better charge transport properties and reduced recombination rates compared to larger QDs. This indicate the importance of further tailoring quantum dots for optimal performance.

Overall, this research successfully integrated QDs into tandem configurations and addressed key challenges in optimizing various aspects of QD solar cells. The findings lay a solid foundation for the continued advancement of this promising technology, emphasizing the need for ongoing efforts in surface passivation, interfacial engineering, charge dynamics optimization, exploration of new materials and combinations for tandem devices, long-term stability testing, and scaling up the production of QD-based solar cells for commercial applications.

The findings of this research have significant implications for the development of next-generation solar cells. The enhanced efficiency of QD-based tandem solar cells can lead to more effective and sustainable solar energy

solutions. Potential applications include high-efficiency solar panels for residential and commercial use, integration into building materials for energy-efficient buildings, and development of flexible and lightweight solar cells for wearable technology and portable devices.

Populärvetenskapligsammanfattning

Den accelererande takten i klimatförändringarna understryker det kritiska behovet av förnybara energilösningar. Fossila bränslen har länge varit den primära energikällan, men deras användning leder till betydande utsläpp av växthusgaser, vilket bidrar till den globala uppvärmningen. Övergången till förnybara energikällor som solenergi har blivit avgörande. Möjligheterna att ta tillvara på solenergin är stor och har potential att möta globala energibehov och solcellsenheter har förmågan att direkt omvandla solljus till elektricitet. Men traditionella kiselbaserade solceller, som dominerar marknaden idag, har begränsningar när det gäller att fånga upp hela spektrumet av solljus, särskilt i den infraröda (IR) regionen, vilket leder till betydande energiförluster. Denna begränsning nödvändiggör utvecklingen av ny solcellsteknik som kan utnyttja ett bredare spektrum av solspektrumet, och därmed effektivare omvandla solljuset till elektricitet.

Forskningen som presenteras i denna avhandling fokuserar på kolloidala kvantprick-solceller (CQD-solceller), en lovande teknologi som tar itu med begränsningarna hos traditionella kiselbaserade solceller. CQD, särskilt blysulfid (PbS) kvantprickar, har unika optoelektroniska egenskaper, inklusive avstämbara bandgap och förmågan att skörda infrarött ljus. Kvantprickar är mycket små partiklar som beter sig annorlunda än sina större motsvarigheter på grund av kvantmekaniken. De kan skräddarsys för att absorbera olika delar av solljusspektrumet genom att ändra deras storlek, form eller ytegenskaper. Dessa funktioner ger kvantprickar en hög potential för användning i tandemsolceller.

Tandemsolceller staplar olika typer av solceller ovanpå varandra, där varje lager fångar olika delar av solljusspektrat. Denna stapling möjliggör mer effektiv användning av solljus jämfört med en enda typ av solcell. Till exempel kan ett lager som fångar synligt ljus kombineras med ett lager som fångar infrarött ljus, vilket ökar den totala energiomvandlingen. Medan CQD-solceller erbjuder en potentiell lösning, innebär deras individuella prestanda och integration i tandemsolceller flera utmaningar, såsom laddningsrekombination, behovet av effektiv ytpassivering och optiska förluster i gränssnitt. Komplexiteten i att optimera solceller för maximal effektivitet belyser dock behovet av avancerad forskning om CQD-prestandaförbättring och integrering i tandemstrukturer. Denna forskning är mycket relevant eftersom den erbjuder en väg till effektivare solceller, vilket bidrar till det bredare målet att minska beroendet av fossila bränslen och mildra klimatförändringarna.

Huvudsyftet med denna avhandling är att undersöka integrationen av CQD-solceller med andra fotovoltaiska teknologier för tandemtillämpningar och att ta itu med de utmaningar som begränsar deras effektivitet. Forskningen utforskar grundläggande aspekter av att integrera CQD-solceller med färgsensibiliserade solceller (DSSC) och perovskitsolceller, optimerar prestandan för CQD-solceller genom ytpassivering och undersökningar av laddningsbärardynamiken. I arbetet försöker vi förbättra laddningsextraktion, minimera rekombinationsförluster för att möjliggöra bättre solceller gjorda av kvantprickar.

Denna forskning använder en mängd olika metoder för att uppnå sina mål. Nyckeltekniker inkluderar syntesen av PbS CQDs med hjälp av en varminsprutningsmetod (hot-injection) för att säkerställa enhetlig storlek och högkvalitativa kvantprickar, integration av CQD-solceller i tandemkonfigurationer genom gränssnittsteknik, ytpassiveringstekniker för att reducera defekttillstånd och förbättra laddningstransportegenskaper, karakterisering av fotovoltaiska laddningar med hjälp av fotoelektriska metoder och avancerade spektroskopimetoder.

Forskningsresultaten, som beskrivs i sju artiklar, visar den betydande potentialen hos CQD-baserade tandemsolceller och de utmaningar som måste åtgärdas för att förbättra deras effektivitet. **Paper I, II och III** fokuserar på att integrera CQD-solceller med andra fotovoltaiska teknologier (DSSCs och perovskiter). De visar att kvantprickar kan fånga en bredare del av solspektrumet, särskilt i det infraröda området, vilket förbättrar den totala ljusabsorptionen och omvandlingseffektiviteten. Men de identifierade också kritiska utmaningar, såsom höga laddningsrekombinationshastigheter och ineffektiv laddningstransport, som hindrar QD-solcellsprestanda, samt vikten av effektiv ljushantering och gränssnittsteknik. **Paper IV och V** gav djupare insikter i att förbättra CQD-solceller, vilket visar att ytpassivering avsevärt förbättrar effektiviteten genom att minska rekombinationsförluster och visar att effektiv laddningsöverföring är avgörande för bättre prestanda. **Paper VI och VII** fokuserade på att förstå laddningsbärarens dynamik inom CQD-solceller. De visar att ytligander och filmtjocklek i hög grad påverkar laddningstransportegenskaperna och avslöjar att mindre CQDs uppvisar bättre laddningstransportegenskaper och reducerade rekombinationshastigheter jämfört med större CQDs. Detta indikerar vikten av att ytterligare skräddarsy kvantprickar för optimal prestanda.

Sammantaget integrerade denna forskning framgångsrikt CQDs i tandemkonfigurationer och tog sig an viktiga utmaningar för att optimera olika aspekter av CQD-solceller. Fynden lägger en solid grund för den fortsatta utvecklingen av denna lovande teknologi, och betonar behovet av pågående ansträngningar inom ytpassivering, gränssnittsteknik, optimering av laddningsdynamik, utforskning av nya material och kombinationer för tandemenheter, långsiktig stabilitetstestning och uppskalning av produktionen av CQD-baserade solceller för kommersiella applikationer.

Resultaten av denna forskning har betydande konsekvenser för utvecklingen av nästa generations solceller. Den förbättrade effektiviteten hos CQD-baserade tandemsolceller kan leda till mer effektiva och hållbara solenergilösningar. Potentiella applikationer inkluderar högeffektiva solpaneler för bostads- och kommersiell användning, integration i byggmaterial för energieffektiva byggnader och utveckling av flexibla och lätta solceller för bärbar teknologi och bärbara enheter.

Podsumowanie popularnonaukowe

Stale przyśpieszające tempo zmian klimatycznych podkreśla krytyczną potrzebę rozwoju rozwiązań w zakresie energii odnawialnej. Paliwa kopalne od dawna są głównym źródłem energii, ale ich wykorzystanie powoduje znaczną emisję gazów cieplarnianych, przyczyniając się tym samym do globalnego ocieplenia. Przejście na odnawialne źródła energii, takie jak energia słoneczna, stało się niezbędne. Energia słoneczna ma bowiem potencjał, aby zaspokoić globalne zapotrzebowanie na energię, a urządzenia z ogniwami słonecznymi mają zdolność do bezpośredniej konwersji światła słonecznego na energię elektryczną. Jednak tradycyjne ogniwa słoneczne na bazie krzemu, które dominują na rynku, mają ograniczenia w przechwytywaniu pełnego spektrum światła słonecznego, szczególnie w zakresie podczerwieni (IR), co prowadzi do znacznych strat energii. Ta luka wymaga opracowania nowych technologii fotowoltaicznych, które mogą wykorzystać szerszy zakres widma słonecznego. Badania przedstawione w tej pracy koncentrują się na ogniwach słonecznych z koloidalnymi kropkami kwantowymi (CQD), obiecującej technologii, która ma potencjał do rozwiązania ograniczeń tradycyjnych ogniw słonecznych na bazie krzemu. Kropki kwantowe, zwłaszcza siarczku ołowiu (PbS), posiadają unikalne właściwości optoelektroniczne, w tym regulowane przerwy pasmowe i zdolność do absorbowania światła podczerwonego. Kropki kwantowe to bardzo małe cząstki, które zachowują się inaczej niż ich większe odpowiedniki ze względu na zasady mechaniki kwantowej. Można je dostosować do pochłaniania różnych części widma światła słonecznego poprzez zmianę ich rozmiaru, kształtu lub właściwości powierzchni. Te cechy dają kropkom kwantowym wysoki potencjał do wykorzystania w tandemowych ogniwach słonecznych.

Tandemowe ogniwa słoneczne układają różne typy ogniw słonecznych jedno na drugim, przy czym każda warstwa jest odpowiedzialna za wychwytywanie innej części widma światła słonecznego. Takie układanie pozwala na bardziej efektywne wykorzystanie światła słonecznego w porównaniu z pojedynczym typem ogniwa słonecznego. Na przykład warstwa, która wychwytuje światło widzialne może być sparowana z warstwą, która wychwytuje światło podczerwone, zwiększając ogólną konwersję energii. Chociaż ogniwa słoneczne z kropkami kwantowymi oferują duży potencjał, ich indywidualna wydajność i integracja do ogniw tandemowych stwarzają kilka wyzwań, takich jak: rekombinacje ładunku, potrzeba skutecznej pasywacji powierzchni i międzywarstwowe straty optyczne. Wysoka złożoność procesów optymalizacji ogniw

słonecznych w celu uzyskania maksymalnej wydajności podkreśla potrzebę zaawansowanych badań nad poprawą produktywności kropek kwantowych i ich integracją ze strukturami tandemowymi. Badania te są wysoce istotne, ponieważ oferują ścieżkę do bardziej wydajnych urządzeń słonecznych, przyczyniając się do zmniejszenia zależności od paliw kopalnych i łagodzenia zmian klimatycznych. Głównymi celami tej pracy są zbadanie integracji ogniw słonecznych opartych na kropkach kwantowych z innymi technologiami fotowoltaicznymi w zastosowaniach tandemowych i zajęcie się wyzwaniami, które ograniczają ich wydajność. Badania te mają na celu skontrolowanie podstawowych aspektów integracji ogniw słonecznych na bazie kropek kwantowych z ogniwami barwnikowymi i perowskitowymi, optymalizację wydajności ogniw słonecznych z kropkami kwantowymi poprzez pasywację powierzchni i badanie dynamiki nośników ładunku, zwiększenie ekstrakcji ładunku, minimalizację strat rekombinacyjnych oraz opracowanie zaawansowanych materiałów i podejść do inżynierii takich urządzeń w celu uwolnienia pełnego ich potencjału.

W badaniach tych zastosowano wiele metod, aby osiągnąć wyżej wymienione cele. Kluczowe techniki obejmują syntezę kropek kwantowych PbS przy użyciu metody wtrysku na gorąco, aby zapewnić im jednolity rozmiar i wysoką jakość, integrację ogniw słonecznych z kropkami kwantowymi w konfiguracjach tandemowych poprzez inżynierię miedzywarstwową, techniki pasywacji powierzchni w celu zmniejszenia defektów i poprawy właściwości transportu ładunku, charakterystykę wydajności fotowoltaicznej poprzez pomiary prądu i napięcia oraz badanie dynamiki nośników ładunku przy użyciu zaawansowanych metod spektroskopii.

Wyniki badań, zebrane w siedmiu artykułach, pokazują znaczny potencjał tandemowych ogniw słonecznych opartych na kropkach kwantowych i wyzwania, które należy rozwiązać, aby zwiększyć ich wydajność. **Artykuły I, II i III** koncentrują się na integracji ogniw słonecznych bazujących na kropkach kwantowych z innymi technologiami fotowoltaicznymi (ogniwa barwnikowe i perowskitowe). Pokazują one, że kropki kwantowe mogą przechwytywać szerszy zakres widma słonecznego, szczególnie w obszarze podczerwieni, zwiększając ogólną absorpcję światła i wydajność konwersji. Jednak zidentyfikowane zostały również krytyczne wyzwania, takie jak wysokie wskaźniki rekombinacji i nieefektywny transport ładunku, które utrudniają działanie ogniw, jak również znaczenie efektywnego zarządzania światłem i inżynierii interwarstwowej. **Artykuły IV i V** dostarczyły głębszych informacji na temat ulepszania ogniw słonecznych z kropkami kwantowymi, wykazując, że pasywacja powierzchni różnymi ligandami tiolowymi znacznie zwiększa wydajność poprzez redukcję strat rekombinacji i pokazując, że efektywny transfer ładunku jest kluczowy dla lepszej wydajności. **Artykuły VI i VII** skupiały się na zrozumieniu dynamiki nośników ładunku w ogniwach słonecznych opartych na kropkach kwantowych. Wykazują, że ligandy powierzchniowe i grubość filmu z kropek kwantowych w dużym stopniu wpływają na właściwości transportu ładunku i ujawniają, że mniejsze kropki kwantowee wykazują

lepsze właściwości transportu ładunku i zmniejszone wskaźniki rekombinacji w porównaniu z większymi. Wskazuje to na wysokie znaczenie dalszego dostosowywania kropek kwantowych w celu uzyskania optymalnej wydajności.

Podsumowujac, badania te pomyślnie zintegrowały ogniwa słoneczne z kropkami kwantowymi w konfiguracjach tandemowych i zidentyfikowaly kluczowe wyzwania w optymalizacji różnych aspektów ogniw słonecznych na bazie kropek kwantowych. Wyniki te stanowią solidne podstawy do dalszego rozwoju tej obiecującej technologii, podkreślając potrzebę ciągłych wysiłków w zakresie pasywacji powierzchni, inżynierii interwarstwowej, optymalizacji dynamiki ładunku, eksploracji nowych materiałów i kombinacji dla urządzeń tandemowych, długoterminowych testów stabilności i zwiększania produkcji ogniw słonecznych opartych na kropkach kwantowych do zastosowań komercyjnych.

Wyniki tych badań mają istotne implikacje dla rozwoju ogniw słonecznych nowej generacji. Zwiększona wydajność ogniw słonecznych tandemowych opartych na kropkach kwantowych może prowadzić do bardziej efektywnych i zrównoważonych rozwiązań w zakresie energii słonecznej. Potencjalne zastosowania obejmują wysokowydajne panele słoneczne do użytku mieszkalnego i komercyjnego, integrację z materiałami budowlanymi w celu uzyskania energooszczędnych budynków oraz rozwój elastycznych i lekkich ogniw słonecznych do technologii noszonych na ciele i urządzeń przenośnych.

References

1. Lee, H. et al. IPCC Sixth Assessment Report - Synthesis Report. Intergovernmental Panel on Climate Change, 2023 (2022).
2. Report, E. G. No more hot air. Nature **447**, (2007).
3. Ritchie Hannah, Rosado Pablo, R. M. CO_2 emissions. OurWorldinData.org [Online Resource]
4. Walsh, P. P., Banerjee, A. & Murphy, E. The UN 2030 Agenda for Sustainable Development. Sustain. Dev. Goals Ser. **Part F2740**, 1–12 (2022).
5. Solomon, S. Stratospheric ozone depletion: A review of concepts and history. Rev. Geophys. **37**, 275–316 (1999).
6. Heede, R. Tracing anthropogenic carbon dioxide and methane emissions to fossil fuel and cement producers, 1854-2010. Clim. Change **122**, 229–241 (2014).
7. Melsted, O. & Pallua, I. The historical transition from coal to hydrocarbons: Previous explanations and the need for an integrative perspective. Can. J. Hist. **53**, 395–422 (2018).
8. Chipperfield, M. P. & Bekki, S. Opinion: Stratospheric ozone – depletion, recovery and new challenges. Atmos. Chem. Phys. **24**, 2783–2802 (2024).
9. Majors Carbon. Carbon_Majors_Launch_Report. Carbon Majors (2024).
10. Qazi, A. et al. Towards Sustainable Energy: A Systematic Review of Renewable Energy Sources, Technologies, and Public Opinions. IEEE Access **7**, 63837–63851 (2019).
11. Sinsel, S. R., Riemke, R. L. & Hoffmann, V. H. Challenges and solution technologies for the integration of variable renewable energy sources—a review. Renew. Energy **145**, 2271–2285 (2020).
12. Lewis, N. S. & Nocera, D. G. Powering the planet: Chemical challenges in solar energy utilization. Proc. Natl. Acad. Sci. U. S. A. **103**, 15729–15735 (2006).
13. Varun Sivaram. Taming the Sun: Innovations to Harness Solar Energy and Power the Planet. **1**, 1–234 (2018).
14. Farmer, J. D. & Lafond, F. How predictable is technological progress? Res. Policy **45**, 647–665 (2016).
15. -. Best Research-Cell Efficiencies. NREL 2025 (2025).
16. Louwen, A., Van Sark, W., Schropp, R. & Faaij, A. A cost roadmap for silicon heterojunction solar cells. Sol. Energy Mater. Sol. Cells **147**, 295–314 (2016).
17. IRENA. Renewable Generation Costs in 2022. International Renewable Energy Agency (2022).
18. Shockley, W. & Queisser, H. J. Detailed balance limit of efficiency of p-n junction solar cells. J. Appl. Phys. **32**, 510–519 (1961).
19. Reichelstein, S. & Yorston, M. The prospects for cost competitive solar PV power. Energy Policy **55**, 117–127 (2013).

20. Hsu, C. W. Using a system dynamics model to assess the effects of capital subsidies and feed-in tariffs on solar PV installations. Appl. Energy **100**, 205–217 (2012).
21. Yan, J., Yang, Y., Elia Campana, P. & He, J. City-level analysis of subsidy-free solar photovoltaic electricity price, profits and grid parity in China. Nat. Energy **4**, 709–717 (2019).
22. Zhang, J. et al. Synthetic Conditions for High-Accuracy Size Control of PbS Quantum Dots. J. Phys. Chem. Lett. **6**, 1830–1833 (2015).
23. Moreels, I. et al. Size-dependent optical properties of colloidal PbS quantum dots. ACS Nano **3**, 3023–3030 (2009).
24. Lee, H. K., Park, T. & Yoo, H. Device Applications Enabled by Bandgap Engineering Through Quantum Dot Tuning: A Review. Materials (Basel). **17**, 1–20 (2024).
25. García de Arquer, F. P. et al. Semiconductor quantum dots: Technological progress and future challenges. Science **373**, (2021).
26. Karani, A. et al. Perovskite/Colloidal Quantum Dot Tandem Solar Cells: Theoretical Modeling and Monolithic Structure. ACS Energy Lett. **3**, 869–874 (2018).
27. Zhu, J., Lu, K., Li, J., Liu, Z. & Ma, W. Tandem solar cells based on quantum dots. Mater. Chem. Front. 1792–1807 (2024). doi:10.1039/d3qm01087b
28. Becquerel, E. On Electron Effects under the Influence of Solar Radiation. Comptes Rendus 'l' Acad. Sci. Paris **9**, 561 (1839).
29. Rühle, S. Tabulated values of the Shockley-Queisser limit for single junction solar cells. Sol. Energy **130**, 139–147 (2016).
30. Gogolin, R. & Harder, N. P. Trapping behavior of Shockley-Read-Hall recombination centers in silicon solar cells. J. Appl. Phys. **114**, (2013).
31. Nakamura, T. et al. Reducing Shockley-Read-Hall recombination losses in the depletion region of a solar cell by using a wide-gap emitter layer. J. Appl. Phys. **130**, (2021).
32. Zhang, J., Lee, S. T. & Sun, B. Effect of series and shunt resistance on organic-inorganic hybrid solar cells performance. Electrochim. Acta **146**, 845–849 (2014).
33. Tress, W. et al. Interpretation and evolution of open-circuit voltage, recombination, ideality factor and subgap defect states during reversible light-soaking and irreversible degradation of perovskite solar cells. Energy Environ. Sci. **11**, 151–165 (2018).
34. Paviet-Salomon, B. et al. Back-Contacted Silicon Heterojunction Solar Cells: Optical-Loss Analysis and Mitigation. IEEE J. Photovoltaics **5**, 1293–1303 (2015).
35. Bremner, S. P., Levy, M. Y. & Honsberg, C. B. Analysis ofTandem Solar Cell Efficiencies Under AM1.5G Spectrum Using a Rapid Flux Calculation Method. Prog. Photovoltaics Res. Appl. **16**, 225–233 (2008).
36. Aydin, E. et al. Enhanced optoelectronic coupling for perovskite/silicon tandem solar cells. Nature **623**, 732–738 (2023).
37. Geisz, J. F. et al. Six-junction III–V solar cells with 47.1% conversion efficiency under 143 Suns concentration. Nat. Energy **5**, 326–335 (2020).
38. Eperon, G. E., Hörantner, M. T. & Snaith, H. J. Metal halide perovskite tandem and multiple-junction photovoltaics. Nat. Rev. Chem. **1**, (2017).
39. Protesescu, L. et al. Nanocrystals of Cesium Lead Halide Perovskites (CsPbX3, X = Cl, Br, and I): Novel Optoelectronic Materials Showing Bright Emission with Wide Color Gamut. Nano Lett. **15**, 3692–3696 (2015).

40. Swarnkar, A. et al. Quantum dot–induced phase stabilization ofa-CsPbI3 perovskite for high-efficiency photovoltaics. Science (80-.). **354**, 92–96 (2016).
41. Chan, W. C. W. et al. Luminescent quantum dots for multiplexed biological detection and imaging. Curr. Opin. Biotechnol. **13**, 40–46 (2002).
42. Shirasaki, Y., Supran, G. J., Bawendi, M. G. & Bulović, V. Emergence of colloidal quantum-dot light-emitting technologies. Nat. Photonics **7**, 13–23 (2013).
43. Wang, R. et al. Colloidal quantum dot ligand engineering for high performance solar cells. Energy Environ. Sci. **9**, 1130–1143 (2016).
44. Rossetti, R., Nakahara, S. & Brus, L. E. Quantum size effects in the redox potentials, resonance Raman spectra, and electronic spectra of CdS crystallites in aqueous solution. J. Chem. Phys. **79**, 1086–1088 (1983).
45. Brus, L. E. Electron-electron and electron-hole interactions in small semiconductor crystallites: The size dependence of the lowest excited electronic state. J. Chem. Phys. **80**, 4403–4409 (1984).
46. Ekimov, A. I., Efros, A. L. & Onushchenko, A. A. Quantum size effect in semiconductor microcrystals. Solid State Commun. **56**, 921–924 (1985).
47. Murray, C. B., Norris, D. J. & Bawendi, M. G. Synthesis and Characterization of Nearly Monodisperse CdE (E = S, Se, Te) Semiconductor Nanocrystallites. J. Am. Chem. Soc. **115**, 8706–8715 (1993).
48. Yoffe, A. D. Low-dimensional systems: Quantum size effects and electronic properties of semiconductor microcrystallites (zero-dimensional systems) and some quasi-two-dimensional systems. Adv. Phys. **51**, 799–890 (2002).
49. Zorman, B., Ramakrishna, M. V. & Friesner, R. A. Quantum Confinement Effects in CdSe Quantum Dots. J. Phys. Chem **99**, 7649–7653 (1995).
50. De Mello Donegá, C. Nanoparticles: Workhorses of nanoscience. Nanoparticles: Workhorses of Nanoscience **9783662448**, (2014).
51. Machol, J. L., Wise, F. W., Patel, R. C. & Tanner, D. B. Vibronic quantum beats in PbS microcrystallites. Phys. Rev. B **48**, 2819–2822 (1993).
52. Moreels, I. et al. Size-Tunable, Bright, and Stable PbS Quantum Dots: A Surface Chemistry Study. ACS Nano **5**, 2004–2012 (2011).
53. Luther, J. M. et al. Multiple exciton generation in films of electronically coupled PbSe quantum dots. Nano Lett. **7**, 1779–1784 (2007).
54. Cunningham, P. D. et al. Enhanced multiple exciton generation in quasi-one-dimensional semiconductors. Nano Lett. **11**, 3476–3481 (2011).
55. Zhang, X., Liu, J. & Johansson, E. M. J. Efficient charge-carrier extraction from Ag2S quantum dots prepared by the SILAR method for utilization of multiple exciton generation. Nanoscale **7**, 1454–1462 (2015).
56. Polman, A., Knight, M., Garnett, E. C., Ehrler, B. & Sinke, W. C. Photovoltaic materials: Present efficiencies and future challenges. Science (80-.). **352**, (2016).
57. Ramasamy, P., Kim, N., Kang, Y. S., Ramirez, O. & Lee, J. S. Tunable, Bright, and Narrow-Band Luminescence from Colloidal Indium Phosphide Quantum Dots. Chem. Mater. **29**, 6893–6899 (2017).
58. Xia, C. et al. Size-dependent band-gap and molar absorption coefficients of colloidal CuInS2 quantum dots. ACS Nano **12**, 8350–8361 (2018).
59. Rainò, G. et al. Ultra-narrow room-temperature emission from single CsPbBr3 perovskite quantum dots. Nat. Commun. **13**, (2022).
60. Dai, X. et al. Solution-processed, high-performance light-emitting diodes based on quantum dots. Nature **515**, 96–99 (2014).

61. Zhang, X., Zhang, J., Liu, J. & Johansson, E. M. J. Solution processed flexible and bending durable heterojunction colloidal quantum dot solar cell. Nanoscale **7**, 11520–11524 (2015).
62. Kim, M. R. Quantum-Dot-Based Solar Cells: Recent Advances, Strategies, and Challenges. (2015).
63. Wang, X. et al. Tandem colloidal quantum dot solar cells employing a graded recombination layer. Nat. Photonics **5**, 480–484 (2011).
64. Xia, Y. et al. Cation-Exchange Synthesis of Highly Monodisperse PbS Quantum Dots from ZnS Nanorods for Efficient Infrared Solar Cells. Adv. Funct. Mater. **30**, 1–11 (2020).
65. Chuang, C. H. M., Brown, P. R., Bulović, V. & Bawendi, M. G. Improved performance and stability in quantum dot solar cells through band alignment engineering. Nat. Mater. **13**, 796–801 (2014).
66. Abdelhameed, M. et al. Tuning the Optical Properties of Silicon Quantum Dots via Surface Functionalization with Conjugated Aromatic Fluorophores. Sci. Rep. **8**, (2018).
67. Shuklov, I. A. & Razumov, V. F. Lead chalcogenide quantum dots for photoelectric devices. Russ. Chem. Rev. **89**, 379–391 (2020).
68. Chen, J., Jia, D., Zhuang, R., Hua, Y. & Zhang, X. Highly Orientated Perovskite Quantum Dot Solids for Efficient Solar Cells. Adv. Mater. **34**, 1–10 (2022).
69. Mei, X., Jia, D., Chen, J., Zheng, S. & Zhang, X. Approaching high-performance light-emitting devices upon perovskite quantum dots: Advances and prospects. Nano Today **43**, 101449 (2022).
70. Chen, F., Lin, Q., Shen, H. & Tang, A. Blue quantum dot-based electroluminescent light-emitting diodes. Materials Chemistry Frontiers **4**, 1340–1365 (2020).
71. Jung, D. et al. Recent Advances in InAs Quantum Dot Lasers Grown on On-Axis (001) Silicon by Molecular Beam Epitaxy. Physica Status Solidi (A) Applications and Materials Science **216**, (2019).
72. Liu, M. et al. Quantum-Dot-Derived Catalysts for CO2 Reduction Reaction. Joule **3**, 1703–1718 (2019).
73. Borchert, H. Solar Cells Based on Colloidal Nanocrystals.
74. Ning, Z. et al. Wave-function engineering of CdSE/CdS core/shell quantum dots for enhanced electron transfer to a TiO2 Substrate. J. Phys. Chem. C **114**, 15184–15189 (2010).
75. Choi, H., Nicolaescu, R., Paek, S., Ko, J. & Kamat, P. V. Supersensitization of CdS quantum dots with a near-infrared organic dye: Toward the design of panchromatic hybrid-sensitized solar cells. ACS Nano **5**, 9238–9245 (2011).
76. Zhou, N. et al. Highly efficient PbS/CdS co-sensitized solar cells based on photoanodes with hierarchical pore distribution. Electrochem. commun. **20**, 97–100 (2012).
77. Becker, M. A., Radich, J. G., Bunker, B. A. & Kamat, P. V. How does a silar cdse film grow? Tuning the deposition steps to suppress interfacial charge recombination in solar cells. J. Phys. Chem. Lett. **5**, 1575–1582 (2014).
78. Leach, A. D. P. & Macdonald, J. E. Optoelectronic Properties of CuInS2 Nanocrystals and Their Origin. J. Phys. Chem. Lett. **7**, 572–583 (2016).
79. Ji, Y. et al. Surface Engineering Enables Efficient AgBiS2 Quantum Dot Solar Cells. Nano Lett. **24**, 10418–10425 (2024).
80. Akhil, S. & Balakrishna, R. G. CuBiS2 Ternary Quantum Dots: Tuning the Deposition Technique for Enhanced Photovoltaic Performance. ACS Appl. Energy Mater. **6**, 7487–7496 (2023).

81. Yang, S., Zhao, P., Zhao, X., Qu, L. & Lai, X. InP and Sn:InP based quantum dot sensitized solar cells. J. Mater. Chem. A **3**, 21922–21929 (2015).
82. Duan, J., Tang, Q., He, B. & Yu, L. Efficient In2S3 Quantum dot-sensitized Solar Cells: A Promising Power Conversion Efficiency of 1.30%. Electrochim. Acta **139**, 381–385 (2014).
83. Mamiyev, Z. Q. & Balayeva, N. O. CuS nanoparticles synthesized by a facile chemical route under different pH conditions. Mendeleev Commun. **26**, 235–237 (2016).
84. Balayeva, O. O. et al. β-NiS and Ni3S4 nanostructures: Fabrication and characterization. Mater. Res. Bull. **75**, 155–161 (2016).
85. Wise, F. W. Lead salt quantum dots: The limit of strong quantum confinement. Acc. Chem. Res. **33**, 773–780 (2000).
86. He, J., Liu, C., Li, F., Sa, R. & Wu, K. Size-dependence of stability and optical properties of lead sulfide clusters. Chem. Phys. Lett. **457**, 163–168 (2008).
87. Santoni, A., Paolucci, G., Santoro, G., Prince, K. C. & Christensen, N. E. Band structure of lead sulphide. J. Phys. Condens. Matter **4**, 6759–6768 (1992).
88. Kang, I. & Wise, F. W. Electronic structure and optical properties of PbS and PbSe quantum dots. J. Opt. Soc. Am. B **14**, 1632 (1997).
89. Goodwin, H., Jellicoe, T. C., Davis, N. J. L. K. & Böhm, M. L. Multiple exciton generation in quantum dot-based solar cells. Nanophotonics **7**, 111–126 (2018).
90. Ding, C. et al. Over 15% Efficiency PbS Quantum-Dot Solar Cells by Synergistic Effects of Three Interface Engineering: Reducing Nonradiative Recombination and Balancing Charge Carrier Extraction. Adv. Energy Mater. **12**, 1–16 (2022).
91. Klem, E. J. D., MacNeil, D. D., Cyr, P. W., Levina, L. & Sargent, E. H. Efficient solution-processed infrared photovoltaic cells: Planarized all-inorganic bulk heterojunction devices via inter-quantum-dot bridging during growth from solution. Appl. Phys. Lett. **90**, (2007).
92. Clifford, J. P., Johnston, K. W., Levina, L. & Sargent, E. H. Schottky barriers to colloidal quantum dot films. Appl. Phys. Lett. **91**, 5–7 (2007).
93. Johnston, K. W. et al. Schottky-quantum dot photovoltaics for efficient infrared power conversion. Appl. Phys. Lett. **92**, (2008).
94. Piliego, C., Protesescu, L., Bisri, S. Z., Kovalenko, M. V. & Loi, M. A. 5.2% efficient PbS nanocrystal Schottky solar cells. Energy Environ. Sci. **6**, 3054–3059 (2013).
95. Choi, M. J. et al. Tailoring of the PbS/metal interface in colloidal quantum dot solar cells for improvements of performance and air stability. Energy Environ. Sci. **7**, 3052–3060 (2014).
96. Azmi, R., Oh, S. H. & Jang, S. Y. High-Efficiency Colloidal Quantum Dot Photovoltaic Devices Using Chemically Modified Heterojunctions. ACS Energy Lett. **1**, 100–106 (2016).
97. Choi, M. J. et al. Highly Asymmetric n+-p Heterojunction Quantum-Dot Solar Cells with Significantly Improved Charge-Collection Efficiencies. Adv. Mater. **28**, 1780–1787 (2016).
98. Lan, X. et al. Self-assembled, nanowire network electrodes for depleted bulk heterojunction solar cells. Adv. Mater. **25**, 1769–1773 (2013).
99. Koleilat, G. I. et al. A donor-supply electrode (DSE) for colloidal quantum dot photovoltaics. Nano Lett. **11**, 5173–5178 (2011).
100. Pattantyus-Abraham, A. G. et al. Depleted-heterojunction colloidal quantum dot solar cells. ACS Nano **4**, 3374–3380 (2010).

101. Brown, P. R. et al. Improved current extraction from ZnO/PbS quantum dot heterojunction photovoltaics using a MoO3 interfacial layer. Nano Lett. **11**, 2955–2961 (2011).
102. Jean, J. et al. ZnO nanowire arrays for enhanced photocurrent in PbS quantum dot solar cells. Adv. Mater. **25**, 2790–2796 (2013).
103. Gao, J., Zhang, J., Van De Lagemaat, J., Johnson, J. C. & Beard, M. C. Charge generation in PbS quantum dot solar cells characterized by temperature-dependent steady-state photoluminescence. ACS Nano **8**, 12814–12825 (2014).
104. Yang, J. et al. Hybrid Surface Passivation for Retrieving Charge Collection Efficiency of Colloidal Quantum Dot Photovoltaics. ACS Appl. Mater. Interfaces **12**, 43576–43585 (2020).
105. Chiu, A. et al. Sulfur-infused hole transport materials to overcome performance-limiting transport in colloidal quantum dot solar cells. ACS Energy Lett. **5**, 2897–2904 (2020).
106. Fan, J. Z. et al. Ligand cleavage enables formation of 1,2-ethanedithiol capped colloidal quantum dot solids. Nanoscale **11**, 10774–10781 (2019).
107. Choi, J. J. et al. PbSe Nanocrystal Excitonic Solar Cells. Nano Lett. **9**, 3749–3755 (2009).
108. Guo, W. et al. Ultrafast electron transfer in low-band gap polymer/PbS nanocrystalline blend films. Adv. Funct. Mater. **26**, 713–721 (2016).
109. Jeong, Y. J., Song, J. H., Jeong, S. & Baik, S. J. PbS Colloidal Quantum Dot Solar Cells with Organic Hole Transport Layers for Enhanced Carrier Separation and Ambient Stability. IEEE J. Photovoltaics **8**, 493–498 (2018).
110. Baek, S. W. et al. Nanostructured Back Reflectors for Efficient Colloidal Quantum-Dot Infrared Optoelectronics. Adv. Mater. **31**, 1–7 (2019).
111. Zhang, Y. et al. Hybrid Quantum Dot/Organic Heterojunction: A Route to Improve Open-Circuit Voltage in PbS Colloidal Quantum Dot Solar Cells. ACS Energy Lett. **5**, 2335–2342 (2020).
112. Zhang, X. et al. Bioinspired synthesis of Ag@TiO2 plasmonic nanocomposites to enhance the light harvesting of dye-sensitized solar cells. RSC Adv. **3**, 18587–18595 (2013).
113. Zhou, R. et al. A novel anion-exchange strategy for constructing high performance PbS quantum dot-sensitized solar cells. Nano Energy **30**, 559–569 (2016).
114. Du, Z., Artemyev, M., Wang, J. & Tang, J. Performance improvement strategies for quantum dot-sensitized solar cells: A review. J. Mater. Chem. A **7**, 2464–2489 (2019).
115. Hodes, G. Comparison of dye- and semiconductor-sensitized porous nanocrystalline liquid junction solar cells. J. Phys. Chem. C **112**, 17778–17787 (2008).
116. Zhang, X. et al. Slow recombination in quantum dot solid solar cell using p-i-n architecture with organic p-type hole transport material. J. Mater. Chem. A **3**, 20579–20585 (2015).
117. Liu, M. et al. Double-Sided Junctions Enable High-Performance Colloidal-Quantum-Dot Photovoltaics. Adv. Mater. **28**, 4142–4148 (2016).
118. Xu, J. et al. 2D matrix engineering for homogeneous quantum dot coupling in photovoltaic solids. Nat. Nanotechnol. **13**, 456–462 (2018).
119. Mandal, D. & Rath, A. K. Quantum Dots Coupled to an Oriented Two-Dimensional Crystalline Matrix for Solar Cell Application. ACS Appl. Mater. Interfaces **10**, 39074–39082 (2018).

120. Gu, M. et al. Stable PbS quantum dot ink for efficient solar cells by solution-phase ligand engineering. J. Mater. Chem. A **7**, 15951–15959 (2019).
121. Kim, H. Il et al. A Tuned Alternating D–A Copolymer Hole-Transport Layer Enables Colloidal Quantum Dot Solar Cells with Superior Fill Factor and Efficiency. Adv. Mater. **32**, 1–7 (2020).
122. Kim, T. et al. Hybrid Tandem Quantum Dot/Organic Solar Cells with Enhanced Photocurrent and Efficiency via Ink and Interlayer Engineering. ACS Energy Lett. **3**, 1307–1314 (2018).
123. Kim, J. et al. Butylamine-Catalyzed Synthesis of Nanocrystal Inks Enables Efficient Infrared CQD Solar Cells. Adv. Mater. **30**, 1–7 (2018).
124. Ning, Z. et al. Graded doping for enhanced colloidal quantum dot photovoltaics. Adv. Mater. **25**, 1719–1723 (2013).
125. Zhang, Y. et al. Realizing solution-processed monolithic PbS QDs/perovskite tandem solar cells with high UV stability. J. Mater. Chem. A **6**, 24693–24701 (2018).
126. Manekkathodi, A. et al. Solution-processed perovskite-colloidal quantum dot tandem solar cells for photon collection beyond 1000 nm. J. Mater. Chem. A **7**, 26020–26028 (2019).
127. Chen, B. et al. Enhanced optical path and electron diffusion length enable high-efficiency perovskite tandems. Nat. Commun. **11**, (2020).
128. Bi, Y. et al. Colloidal Quantum Dot Tandem Solar Cells Using Chemical Vapor Deposited Graphene as an Atomically Thin Intermediate Recombination Layer. ACS Energy Lett. **3**, 1753–1759 (2018).
129. Crisp, R. W. et al. Tandem Solar Cells from Solution-Processed CdTe and PbS Quantum Dots Using a ZnTe-ZnO Tunnel Junction. Nano Lett. **17**, 1020–1027 (2017).
130. Kim, T. et al. Hybrid tandem solar cells with depleted-heterojunction quantum dot and polymer bulk heterojunction subcells. Nano Energy **17**, 196–205 (2015).
131. Kim, T. et al. Hybrid tandem quantum dot/organic photovoltaic cells with complementary near infrared absorption. Appl. Phys. Lett. **110**, (2017).
132. Baek, S. W. et al. Efficient hybrid colloidal quantum dot/organic solar cells mediated by near-infrared sensitizing small molecules. Nat. Energy **4**, 969–976 (2019).
133. Yuan, L. et al. Four-Terminal Tandem Solar Cell with Dye-Sensitized and PbS Colloidal Quantum-Dot-Based Subcells. ACS Appl. Energy Mater. **3**, 3157–3161 (2020).
134. Semonin, O. E., Nozik, A. J. & Beard, M. C. Peak External Photocurrent Quantum Efficiency Exceeding 100% via MEG in a Quantum Dot Solar Cell. Science (80-.). **1530**, 1530–1534 (2013).
135. Böhm, M. L. et al. Lead telluride quantum dot solar cells displaying external quantum efficiencies exceeding 120%. Nano Lett. **15**, 7987–7993 (2015).
136. Yan, Y. et al. Multiple exciton generation for photoelectrochemical hydrogen evolution reactions with quantum yields exceeding 100%. Nat. Energy **2**, 1–7 (2017).
137. Leatherdale, C. A. & Bawendi, M. G. Electron and hole relaxation pathways in semiconductor quantum dots. Phys. Rev. B - Condens. Matter Mater. Phys. **60**, 13740–13749 (1999).
138. Singhal, P. & Ghosh, H. N. Hot-hole extraction from quantum dot to molecular adsorbate. Chem. - A Eur. J. **21**, 4405–4412 (2015).
139. Spoor, F. C. M. et al. Hole cooling is much faster than electron cooling in pbse quantum dots. ACS Nano **10**, 695–703 (2016).

140. López-Arteaga, R. & Peon, J. Ultrafast Photoluminescence Kinetics from Hot Excitonic States in CdSe Nanocrystals. J. Phys. Chem. C **122**, 26698–26706 (2018).
141. Zhang, Y. et al. Lead Selenide Colloidal Quantum Dot Solar Cells Achieving High Open-Circuit Voltage with One-Step Deposition Strategy. J. Phys. Chem. Lett. **9**, 3598–3603 (2018).
142. Giansante, C. & Infante, I. Surface Traps in Colloidal Quantum Dots: A Combined Experimental and Theoretical Perspective. J. Phys. Chem. Lett. **8**, 5209–5215 (2017).
143. Zhang, Y. et al. Air Stable PbSe Colloidal Quantum Dot Heterojunction Solar Cells: Ligand-Dependent Exciton Dissociation, Recombination, Photovoltaic Property, and Stability. J. Phys. Chem. C **120**, 28509–28518 (2016).
144. Li, B. et al. Excitons and Biexciton Dynamics in Single CsPbBr 3 Perovskite Quantum Dots. J. Phys. Chem. Lett. **9**, 6934–6940 (2018).
145. Boehme, S. C. et al. Density of trap states and Auger-mediated electron trapping in CdTe quantum-dot solids. Nano Lett. **15**, 3056–3066 (2015).
146. Nagpal, P. & Klimov, V. I. Role of mid-gap states in charge transport and photoconductivity in semiconductor nanocrystal films. Nat. Commun. **2**, (2011).
147. Klimov, V. I. Multicarrier interactions in semiconductor nanocrystals in relation to the phenomena of auger recombination and carrier multiplication. Annu. Rev. Condens. Matter Phys. **5**, 285–316 (2014).
148. Klimov, V. I. & McBranch, D. W. Auger-process-induced charge separation in semiconductor nanocrystals. Phys. Rev. B - Condens. Matter Mater. Phys. **55**, 13173–13179 (1997).
149. Schaller, R. D. & Klimov, V. I. High efficiency carrier multiplication in PbSe nanocrystals: Implications for solar energy conversion. Phys. Rev. Lett. **92**, 1–4 (2004).
150. Cooney, R. R. et al. Unified picture of electron and hole relaxation pathways in semiconductor quantum dots. Phys. Rev. B - Condens. Matter Mater. Phys. **75**, 1–14 (2007).
151. Ross, R. T. & Nozik, A. J. Efficiency of hot-carrier solar energy converters. J. Appl. Phys. **53**, 3813–3818 (1982).
152. Chang, J. et al. Ligand-dependent exciton dynamics and photovoltaic properties of PbS quantum dot heterojunction solar cells. Phys. Chem. Chem. Phys. **19**, 6358–6367 (2017).
153. Lingley, Z., Lu, S. & Madhukar, A. The dynamics of energy and charge transfer in lead sulfide quantum dot solids. J. Appl. Phys. **115**, (2014).
154. Vokhmintcev, K. V., Samokhvalov, P. S. & Nabiev, I. Charge transfer and separation in photoexcited quantum dot-based systems. Nano Today **11**, 189–211 (2016).
155. Zhu, H., Yang, Y., Wu, K. & Lian, T. Charge Transfer Dynamics from Photoexcited Semiconductor Quantum Dots. Annu. Rev. Phys. Chem. **67**, 259–281 (2016).
156. Palato, S. et al. Electron Dynamics at the Surface of Semiconductor Nanocrystals. J. Phys. Chem. C **121**, 26519–26527 (2017).
157. Voznyy, O., Sutherland, B. R., Ip, A. H., Zhitomirsky, D. & Sargent, E. H. Engineering charge transport by heterostructuring solution-processed semiconductors. Nat. Rev. Mater. **2**, 1–10 (2017).
158. Guglietta, G. W. et al. Lifetime, mobility, and diffusion of photoexcited carriers in ligand-exchanged lead selenide nanocrystal films measured by time-resolved terahertz spectroscopy. ACS Nano **9**, 1820–1828 (2015).

159. Crisp, R. W. et al. Metal Halide Solid-State Surface Treatment for High Efficiency PbS and PbSe QD Solar Cells. Sci. Rep. **5**, 1–6 (2015).
160. Kagan, C. R. & Murray, C. B. Charge transport in strongly coupled quantum dot solids. Nat. Nanotechnol. **10**, 1013–1026 (2015).
161. Scheele, M. To be or not to be: Band-like transport in quantum dot solids. Zeitschrift fur Phys. Chemie **229**, 167–178 (2015).
162. Lan, X. et al. Quantum dot solids showing state-resolved band-like transport. Nat. Mater. **19**, 323–329 (2020).
163. Zhang, Z. et al. Effect of Halide Treatments on PbSe Quantum Dot Thin Films: Stability, Hot Carrier Lifetime, and Application to Photovoltaics. J. Phys. Chem. C **119**, 24149–24155 (2015).
164. Lin, Q. et al. Phase-Transfer Ligand Exchange of Lead Chalcogenide Quantum Dots for Direct Deposition of Thick, Highly Conductive Films. J. Am. Chem. Soc. **139**, 6644–6653 (2017).
165. Zhang, Y. et al. Photoexcited carrier dynamics in colloidal quantum dot solar cells: Insights into individual quantum dots, quantum dot solid films and devices. Chem. Soc. Rev. **49**, 49–84 (2020).
166. Kim, T. et al. Design Strategy of Quantum Dot Thin-Film Solar Cells. Small **16**, 1–13 (2020).
167. Goldschmidt, V. M. Die Gesetze der Krystallochemie. Perit. Dial. Int. **14**, 477–485 (1926).
168. Kobayashi, K., Kimura, T., Sawada, H., Terakura, K. & Tokura, Y. Room-temperature magnetoresistance in anoxide materialwith anordered double perovskite structure. Nature **395**, 677–680 (1998).
169. Miyasaka, T. Lead halide perovskites in thin film photovoltaics: Background and perspectives. Bull. Chem. Soc. Jpn. **91**, 1058–1068 (2018).
170. Green, M. A., Ho-Baillie, A. & Snaith, H. J. The emergence of perovskite solar cells. Nat. Photonics **8**, 506–514 (2014).
171. Grätzel, M. The light and shade of perovskite solar cells. Nat. Mater. **13**, 838–842 (2014).
172. Weber, D. CH3NH3SnBrxI3-x (x = 0-3), a Sn(II)-System with Cubic Perovskite Structure. Zeitschrift für Naturforsch. **33b**, 862–865 (1978).
173. Weber, D. $CH_3NH_3PbX_3$, ein Pb(II)-System mit kubischer Perowskitstruktur / $CH_3NH_3PbX_3$, a Pb(II)-System with Cubic Perovskite Structure. Zeitschrift für Naturforsch. B **33**, 1443–1445 (1978).
174. Mitzi, D. B., Wang, S., Feild, C. A., Chess, C. A. & Guloy, A. M. Conducting Layered Organic-inorganic Halides Containing 〈110〉 -Oriented Perovskite Sheets. Science (80-.). **267**, 1473–1476 (1995).
175. Takeoka, Y., Asai, K., Rikukawa, M. & Sanui, K. Incorporation of conjugated polydiacetylene systems into organic—inorganic quantum-well structures. Chem. Commun. **1**, 2592–2593 (2001).
176. Kondo, T. et al. RESONANT THIRD-ORDER OPTICAL NONLINEARITY IN THE LAYERED PEROVSKITE-TYPE MATERIAL (C6H13NH3)2PbI4. Solid State Commun. **105**, 503–506 (1998).
177. Tanaka, K. et al. Comparative study on the excitons in lead-halide-based perovskite-type crystals CH3NH3PbBr3 CH3NH 3PbI3. Solid State Commun. **127**, 619–623 (2003).
178. Kojima, A., Teshima, K., Shirai, Y. & Miyasaka, T. Organometal halide perovskites as visible-light sensitizers for photovoltaic cells. J. Am. Chem. Soc. **131**, 6050–6051 (2009).

179. Lee, M. M., Teuscher, J., Miyasaka, T., Murakami, T. N. & Snaith, H. J. Efficient Hybrid Solar Cells Basedon Meso-SuperstructuredOrganometal Halide Perovskites. Science (80-.). **338**, 643–647 (2012).
180. Kim, H. S. et al. Lead iodide perovskite sensitized all-solid-state submicron thin film mesoscopic solar cell with efficiency exceeding 9%. Sci. Rep. **2**, 1–7 (2012).
181. Saliba, M. et al. Cesium-containing triple cation perovskite solar cells: Improved stability, reproducibility and high efficiency. Energy Environ. Sci. **9**, 1989–1997 (2016).
182. McMeekin, D. P. et al. A mixed-cation lead mixed-halide perovskite absorber for tandem solar cells. Science (80-.). **351**, 151–155 (2016).
183. Jeon, N. J. et al. Compositional engineering of perovskite materials for high-performance solar cells. Nature **517**, 476–480 (2015).
184. Noel, N. K. et al. Lead-free organic-inorganic tin halide perovskites for photovoltaic applications. Energy Environ. Sci. **7**, 3061–3068 (2014).
185. Ke, W. & Kanatzidis, M. G. Prospects for low-toxicity lead-free perovskite solar cells. Nat. Commun. **10**, 1–4 (2019).
186. Aktas, E. et al. Challenges and strategies toward long-term stability of lead-free tin-based perovskite solar cells. Commun. Mater. **3**, 1–14 (2022).
187. Shao, J. Y. et al. Recent progress in perovskite solar cells: material science. Science China Chemistry **66**, (2023).
188. Ho-Baillie, A. W. Y. et al. Recent progress and future prospects of perovskite tandem solar cells. Appl. Phys. Rev. **8**, (2021).
189. Dunlap-Shohl, W. A., Zhou, Y., Padture, N. P. & Mitzi, D. B. Synthetic Approaches for Halide Perovskite Thin Films. Chem. Rev. **119**, 3193–3295 (2019).
190. Jiang, Y., He, S., Qiu, L., Zhao, Y. & Qi, Y. Perovskite solar cells by vapor deposition based and assisted methods. Appl. Phys. Rev. **9**, (2022).
191. Saki, Z., Byranvand, M. M., Taghavinia, N., Kedia, M. & Saliba, M. Solution-processed perovskite thin-films: The journey from lab: The large-scale solar cells. Energy Environ. Sci. **14**, 5690–5722 (2021).
192. Yan, J., Savenije, T. J., Mazzarella, L. & Isabella, O. Progress and challenges on scaling up of perovskite solar cell technology. Sustain. Energy Fuels **6**, 243–266 (2022).
193. Wang, F. et al. Recent progress of scalable perovskite solar cells and modules. Energy Rev. **1**, 100010 (2022).
194. Gao, Y. et al. Flexible Perovskite Solar Cells: From Materials and Device Architectures to Applications. ACS Energy Lett. **7**, 1412–1445 (2022).
195. Yang, F. et al. High Bending Durability of Efficient Flexible Perovskite Solar Cells Using Metal Oxide Electron Transport Layer. J. Phys. Chem. C **122**, 17088–17095 (2018).
196. Ohashi, N. et al. Bilayer Indium Tin Oxide Electrodes for Deformation-Free Ultrathin Flexible Perovskite Solar Cells. Sol. RRL **7**, 1–7 (2023).
197. D'Innocenzo, V. et al. Excitons versus free charges in organo-lead tri-halide perovskites. Nat. Commun. **5**, 1–6 (2014).
198. Miyata, A. et al. Direct measurement of the exciton binding energy and effective masses for charge carriers in organic-inorganic tri-halide perovskites. Nat. Phys. **11**, 582–587 (2015).
199. Doughty, B., Simpson, M. J., Yang, B. & Xiao, K. Simplification of femtosecond transient absorption microscopy data from CH3NH3Pb 3 perovskite thin films into decay associated amplitude maps. Nanotechnology **27**, 1–10 (2016).

200. Jha, A. et al. Direct Observation of Ultrafast Exciton Dissociation in Lead Iodide Perovskite by 2D Electronic Spectroscopy. ACS Photonics **5**, 852–860 (2018).
201. Sun, Q. et al. Ultrafast and high-yield polaronic exciton dissociation in two-dimensional perovskites. J. Am. Chem. Soc. **143**, 19128–19136 (2021).
202. Seitz, M. et al. Exciton diffusion in two-dimensional metal-halide perovskites. Nat. Commun. **11**, 1–8 (2020).
203. Huang, J. et al. Influence of film quality on power conversion effciency in perovskite solar cells. Coatings **9**, 1–10 (2019).
204. Wu, X. et al. Trap states in lead iodide perovskites. J. Am. Chem. Soc. **137**, 2089–2096 (2015).
205. Zhao, S. et al. Cascade Type-II 2D/3D Perovskite Heterojunctions for Enhanced Stability and Photovoltaic Efficiency. Sol. RRL **4**, 1–9 (2020).
206. Ren, X., Wang, Z., Sha, W. E. I. & Choy, W. C. H. Exploring the Way to Approach the Efficiency Limit of Perovskite Solar Cells by Drift-Diffusion Model. ACS Photonics **4**, 934–942 (2017).
207. Van Reenen, S., Kemerink, M. & Snaith, H. J. Modeling Anomalous Hysteresis in Perovskite Solar Cells. J. Phys. Chem. Lett. **6**, 3808–3814 (2015).
208. Saba, M., Quochi, F., Mura, A. & Bongiovanni, G. Excited State Properties of Hybrid Perovskites. Acc. Chem. Res. **49**, 166–173 (2016).
209. He, H. et al. Exciton localization in solution-processed organolead trihalide perovskites. Nat. Commun. **7**, 1–7 (2016).
210. Lin, Y. et al. Unveiling the operation mechanism of layered perovskite solar cells. Nat. Commun. **10**, 1–11 (2019).
211. Xu, Z. et al. Phase Distribution and Carrier Dynamics in Multiple-Ring Aromatic Spacer-Based Two-Dimensional Ruddlesden-Popper Perovskite Solar Cells. ACS Nano **14**, 4871–4881 (2020).
212. Bera, D., Qian, L., Tseng, T. K. & Holloway, P. H. Quantum dots and their multimodal applications: A review. Materials (Basel). **3**, 2260–2345 (2010).
213. Chen, Z. et al. A Review of Top-Down Strategies for the Production of Quantum-Sized Materials. Small Sci. **3**, (2023).
214. Hines, M. A. & Scholes, G. D. Colloidal PbS Nanocrystals with Size-Tunable Near-Infrared Emission: Observation of Post-Synthesis Self-Narrowing of the Particle Size Distribution. Adv. Mater. **15**, 1844–1849 (2003).
215. Talapin, D. V., Rogach, A. L., Haase, M. & Weller, H. Evolution of an ensemble of nanoparticles in a colloidal solution: Theoretical study. J. Phys. Chem. B **105**, 12278–12285 (2001).
216. LaMer, V. K. & Dinegar, R. H. Theory, Production and Mechanism of Formation of Monodispersed Hydrosols. South. Med. J. **72**, 4847–4854 (1950).
217. Polte, J. Fundamental growth principles of colloidal metal nanoparticles - a new perspective. CrystEngComm **17**, 6809–6830 (2015).
218. Baronov, A., Bufkin, K., Shaw, D. W., Johnson, B. L. & Patrick, D. L. A simple model of burst nucleation. Phys. Chem. Chem. Phys. **17**, 20846–20852 (2015).
219. Choi, H., Ko, J. H., Kim, Y. H. & Jeong, S. Steric-hindrance-driven shape transition in PbS quantum dots: Understanding size-dependent stability. J. Am. Chem. Soc. **135**, 5278–5281 (2013).
220. Tan, L., Li, P., Sun, B., Chaker, M. & Ma, D. Stabilities Related to Near-Infrared Quantum Dot-Based Solar Cells: The Role of Surface Engineering. ACS Energy Lett. **2**, 1573–1585 (2017).

221. Lin, W. M. M., Yarema, M., Liu, M., Sargent, E. & Wood, V. Nanocrystal quantum dot devices: How the lead sulfide (pbs) system teaches us the importance of surfaces. Chimia (Aarau). **75**, 398–413 (2021).
222. Remacle, F. & Levine, R. D. Quantum dots as chemical building blocks: Elementary theoretical considerations. ChemPhysChem **2**, 20–36 (2001).
223. Choi, J. J. et al. Photogenerated exciton dissociation in highly coupled lead salt nanocrystal assemblies. Nano Lett. **10**, 1805–1811 (2010).
224. Logar, M., Xu, S., Acharya, S. & Prinz, F. B. Variation of energy density of states in quantum dot arrays due to interparticle electronic coupling. Nano Lett. **15**, 1855–1860 (2015).
225. Kagan, C. R., Lifshitz, E., Sargent, E. H. & Talapin, D. V. Building devices from colloidal quantum dots. Science (80-.). **353**, (2016).
226. Brown, P. R. et al. Energy level modification in lead sulfide quantum dot thin films through ligand exchange. ACS Nano **8**, 5863–5872 (2014).
227. Kim, J., Song, S., Kim, Y. H. & Park, S. K. Recent Progress of Quantum Dot-Based Photonic Devices and Systems: A Comprehensive Review of Materials, Devices, and Applications. Small Struct. **2**, 1–24 (2021).
228. Duan, L. et al. Quantum Dots for Photovoltaics: A Tale of Two Materials. Adv. Energy Mater. **11**, 1–23 (2021).
229. Teh, Z. L. et al. Enhanced Power Conversion Efficiency via Hybrid Ligand Exchange Treatment of p-Type PbS Quantum Dots. ACS Appl. Mater. Interfaces **12**, 22751–22759 (2020).
230. Hu, L. et al. Optimizing Surface Chemistry of PbS Colloidal Quantum Dot for Highly Efficient and Stable Solar Cells via Chemical Binding. Adv. Sci. **8**, 1–9 (2021).
231. Mubarok, M. Al et al. PbS-Based Quantum Dot Solar Cells with Engineered I -Conjugated Polymers Achieve 13% Efficiency. ACS Energy Lett. **5**, 3452–3460 (2020).
232. Choi, M. J. et al. Cascade surface modification of colloidal quantum dot inks enables efficient bulk homojunction photovoltaics. Nat. Commun. **11**, 1–9 (2020).
233. Sahoo, U., Seth, A. K. & Chawla, R. UV/Visible Spectroscopy. (LAP LAMBERT Academic Publishing, 2012).
234. Lakowicz, J. R. Principles of Fluorescence Spectroscopy. (Springer New York, 2006). doi:https://doi.org/10.1007/978-0-387-46312-4
235. Litvin, A. P. et al. Size and temperature dependencies of the low-energy electronic structure of PbS quantum dots. J. Phys. Chem. C **118**, 20721–20726 (2014).
236. Warner, J. H., Thomsen, E., Watt, A. R., Heckenberg, N. R. & Rubinsztein-Dunlop, H. Time-resolved photoluminescence spectroscopy of ligand-capped PbS nanocrystals. Nanotechnology **16**, 175–179 (2005).
237. Zhang, X. et al. Highly photostable and efficient semitransparent quantum dot solar cells by using solution-phase ligand exchange. Nano Energy **53**, 373–382 (2018).
238. Kirmani, A. R. et al. Overcoming the Ambient Manufacturability-Scalability-Performance Bottleneck in Colloidal Quantum Dot Photovoltaics. Adv. Mater. **30**, 1–9 (2018).
239. Kufer, D., Lasanta, T., Bernechea, M., Koppens, F. H. L. & Konstantatos, G. Interface Engineering in Hybrid Quantum Dot-2D Phototransistors. ACS Photonics **3**, 1324–1330 (2016).

240. Özdemir, O., Ramiro, I., Gupta, S. & Konstantatos, G. High Sensitivity Hybrid PbS CQD-TMDC Photodetectors up to 2 μm. ACS Photonics **6**, 2381–2386 (2019).
241. Zereshki, P. et al. Observation of charge transfer in mixed-dimensional heterostructures formed by transition metal dichalcogenide monolayers and PbS quantum dots. Phys. Rev. B **100**, 1–8 (2019).

Acta Universitatis Upsaliensis

Digital Comprehensive Summaries of Uppsala Dissertations from the Faculty of Science and Technology 2503

Editor: The Dean of the Faculty of Science and Technology

A doctoral dissertation from the Faculty of Science and Technology, Uppsala University, is usually a summary of a number of papers. A few copies of the complete dissertation are kept at major Swedish research libraries, while the summary alone is distributed internationally through the series Digital Comprehensive Summaries of Uppsala Dissertations from the Faculty of Science and Technology. (Prior to January, 2005, the series was published under the title "Comprehensive Summaries of Uppsala Dissertations from the Faculty of Science and Technology".)

Distribution: publications.uu.se
urn:nbn:se:uu:diva-550366

ACTA UNIVERSITATIS
UPSALIENSIS
2025